

**University of Alberta**

*Insights into the Performance of Proton-Exchange Membrane Fuel Cells obtained  
from  $^1\text{H}$  NMR Microscopy Experiments*

by

Kirk Wayne Feindel



A thesis submitted to the Faculty of Graduate Studies and Research  
in partial fulfillment of the requirements for the degree of

Doctor of Philosophy

Department of Chemistry

Edmonton, Alberta

Spring 2007



Library and  
Archives Canada

Bibliothèque et  
Archives Canada

Published Heritage  
Branch

Direction du  
Patrimoine de l'édition

395 Wellington Street  
Ottawa ON K1A 0N4  
Canada

395, rue Wellington  
Ottawa ON K1A 0N4  
Canada

*Your file* *Votre référence*  
*ISBN: 978-0-494-29672-1*  
*Our file* *Notre référence*  
*ISBN: 978-0-494-29672-1*

**NOTICE:**

The author has granted a non-exclusive license allowing Library and Archives Canada to reproduce, publish, archive, preserve, conserve, communicate to the public by telecommunication or on the Internet, loan, distribute and sell theses worldwide, for commercial or non-commercial purposes, in microform, paper, electronic and/or any other formats.

The author retains copyright ownership and moral rights in this thesis. Neither the thesis nor substantial extracts from it may be printed or otherwise reproduced without the author's permission.

**AVIS:**

L'auteur a accordé une licence non exclusive permettant à la Bibliothèque et Archives Canada de reproduire, publier, archiver, sauvegarder, conserver, transmettre au public par télécommunication ou par l'Internet, prêter, distribuer et vendre des thèses partout dans le monde, à des fins commerciales ou autres, sur support microforme, papier, électronique et/ou autres formats.

L'auteur conserve la propriété du droit d'auteur et des droits moraux qui protègent cette thèse. Ni la thèse ni des extraits substantiels de celle-ci ne doivent être imprimés ou autrement reproduits sans son autorisation.

---

In compliance with the Canadian Privacy Act some supporting forms may have been removed from this thesis.

Conformément à la loi canadienne sur la protection de la vie privée, quelques formulaires secondaires ont été enlevés de cette thèse.

While these forms may be included in the document page count, their removal does not represent any loss of content from the thesis.

Bien que ces formulaires aient inclus dans la pagination, il n'y aura aucun contenu manquant.

  
**Canada**

*"The ideal condition  
Would be, I admit, that men should be right by instinct;  
But since we are all likely to go astray,  
The reasonable thing is to learn from those who can teach."*

Sophocles, *Antigone*

## Abstract

Proton nuclear magnetic resonance microscopy was employed to investigate *in-situ* the effects of the distribution and amount of water in operating proton-exchange membrane fuel cells, PEMFCs. This is a timely and significant application of NMR microscopy for numerous reasons. The quintessence of a PEMFC is the membrane that is conductive to protons while essentially impermeable to the fuel and non-conductive to electrons. The performance of PEMFCs using typical proton-exchange membranes, PEMs, such as Nafion is closely related to the distribution and content of water in the PEM and neighbouring regions (*e.g.*, gas flow channels). Few available techniques, however, can be used to visualize and investigate water in operating PEMFCs and obtain information that is critical to develop effective designs and to parameterize and validate theoretical models.

The ultimate goal of this research was to demonstrate that  $^1\text{H}$  NMR microscopy can provide a *qualitative* picture of dynamic water distribution in operating PEMFCs and, that PEMFC performance can *quantitatively* be related to the amount of water in various parts of the system.

PEMFCs were designed and constructed to fit within 10 mm and 30 mm diameter NMR microscopy probes and to operate within the strong magnetic fields required to complete the studies. Preliminary experiments demonstrated that  $\text{H}_2\text{O}(l)$  produced from the reduction of  $\text{O}_2(g)$  is observable, and that water in the

PEM diffuses outward from the catalyst decal into surrounding membrane. The first images of the in-plane distribution of water in the PEM between the catalyst layers are reported. The results show that feed gas configuration (*i.e.*, co- vs. counter-flow), gas flow rates, and PEMFC power output affect the distribution of water in the PEM and in the cathode flow field, and confirm the predictions of several theoretical models. Image contrast is introduced by exchanging hydrogen for deuterium through use of either  $D_2O(l)$  or by operating the PEMFC on  $D_2(g)$ . The integrated intensity of the images corresponds well to changes in the PEMFC power output, and the feasibility of determining the absolute water content of the PEM is investigated. The results obtained suggest several projects for future research.

## *Preface*

Since joining Rod's research group as a graduate student in the fall of 2001, I have been involved in a plethora of research projects. These include experimental investigations of coupled multi-spin systems, less commonly studied quadrupolar nuclei ( $^{35}\text{Cl}$ ,  $^{55}\text{Mn}$ ,  $^{91}\text{Zr}$ ,  $^{139}\text{La}$ ) at high applied magnetic fields, quantum chemical investigations of magnetic shielding and indirect nuclear spin-spin coupling tensors, and application of  $^1\text{H}$  NMR microscopy to investigate water in hydrogen fuel cells. I recall that throughout my graduate student career I was often asked what the topic of my Thesis was. Reflecting upon that now, I think I had as many responses as the number of times I was asked. I am fortunate that Rod recognized the importance of students having access to the latest NMR equipment and techniques for the exploration and characterization of materials. Within the first year of my Ph.D. our new Bruker spectrometers including a micro-imaging accessory were installed and a hyperpolarized Xe-129 NMR spectroscopy system was constructed.

Although I continue experimental and theoretical NMR studies of solids, I have chosen to focus my Thesis on  $^1\text{H}$  NMR microscopy. In specific, this Thesis is composed of research into the application of  $^1\text{H}$  NMR microscopy to investigate water throughout operating proton-exchange membrane fuel cells that was completed during the past three years. I have chosen this topic because the application is novel, the results are high-impact, and have been well received in the literature. The publications that have resulted from this research are listed in Appendix A.1 and publications resulting from other research are listed in Appendix A.2.

## Acknowledgement

To start, I thank my supervisor Prof. Rod Wasylshen for providing access to his seemingly endless knowledge of the NMR literature. I appreciated Rod's genuine desire for his students to enjoy their research. I thank Rod for his patience and tolerance of our extracurricular activities during the early years of my graduate studies. Rod has continued to foster my desire for balance in research, hobbies, family, and relationships. In particular, I will remember his encouragement to leave the lab early when heading to the mountains for the weekend.

I thank the current members of the solid-state NMR group for helpful discussions over the years. Shelley is thanked for introducing me to Rod at Dalhousie after my third year of undergrad. I appreciate the many hours Harris has spent on numerous occasions making the Linux computers do what I thought they were supposed to do. Thanks go to Guy for getting me started with computational chemistry, for training on the spectrometers, and for his morning greeting. My graduate career has been shared with Kris Ooms who has been a steadfast friend and colleague. I think we have grown together in many aspects of academic, personal, and professional life. Our often different perspectives and frequent discussions on individual research lead to successful collaboration. On many occasion, discussions over pints and dinner began with academics and turned to scotch on politics and religion.

Former group member Prof. David Bryce is responsible for instilling the belief that there are no *good* excuses for not being productive during grad school. Dave left me with a great deal of respect for Rod, and the reminder that talking daily with your supervisor is the best way to keep research projects on track. In addition, although I was sceptical at first, I now understand Dave's balance of caffeine, research, beer, and vegetables. Former group member Dr. Myrlene Gee is

thanked for assistance with single-crystal NMR experiments, theoretical calculations, the forgotten art of paper box making, and more recently aspects of NMR imaging.

In regards to the PEMFC research, many acknowledgements are required. Prof. Steve Bergens is thanked for providing direction and encouragement with the PEMFC research. I enjoyed seeing fuzzy grayscale images of water in a fuel cell bring a smile to Steve's face and appreciate our many discussions on what the results from my experiments might mean. I hope some of Steve's elegant style of scientific writing has rubbed off on me. Thanks go to Logan for getting me started with operating the PEMFCs and his guidance when I prepared the MEAs. The Department of Chemistry Machine Shop is thanked for their continued support. In particular, the PEMFCs were machined, and if necessary repaired, by Dieter Starke. Without Dieter, this research would not have been possible. Dieter is also acknowledged for numerous conversations on topics ranging from weather patterns and isobars to family origins in Europe. Al, Kim, and Ed in the Electronics Shop are thanked for their extended assistance. Dr. Thomas Oerther with Bruker-BioSpin GmbH is acknowledged for his technical support with the micro-imaging hardware and software.

Aspects of my research over the past five years involving solid-state NMR and quantum chemical computations are not included in this thesis; however, many people warrant acknowledgement: Much of my high applied magnetic field research was performed in the Environmental Molecular Sciences Laboratory, a national scientific user facility sponsored by the US Department of Energy's Office of Biological and Environmental Research and located at Pacific Northwest National Laboratory in Richland, WA. I thank Nancy Isern, Jesse Sears, Andy Lipton, Joe Ford, David Hoyt, and Paul Ellis for their assistance at EMSL and discussions on



research. Prof. Jochen Autschbach is thanked for assistance with the CPL module for the calculation of spin-spin coupling tensors in the ADF program. For providing computer resources: Prof. P-N Roy is thanked for access to *Plethora*, funded in-part by CFI, and Prof. Cynthia Jameson and Dr. Devin Sears are thanked for access to *Buckingham* and *Gutowsky*.

Profs. Mariusz Klobukowski, John-Bruce Green, Christian Beaulieu, and Colin Fyfe are thanked for examining my thesis and serving on my Ph.D. committee.

For financial support over the past five years the University of Alberta, Alberta Ingenuity, NSERC, and the GSA are acknowledged.

I'm very lucky to have found Jean who has a mysterious ability to tolerate, love, and accept me.

I thank my family for their love and support, and for attempting to remember aspects of my research beyond "he works with big magnets". Special thanks go to Nanny for continuing to write me letters and for keeping me in her prayers.

## Table of Contents

<b>Chapter 1. Introduction and Objectives.....</b>	<b>1</b>
1.1. Introduction.....	1
1.1.1. Proton-Exchange Membrane Fuel Cells.....	1
1.1.2. Magnetic Resonance Imaging.....	4
1.2. Thesis Objectives and Outline.....	6
1.3. References.....	7
<b>Chapter 2. Background and Theory: NMR Microscopy.....</b>	<b>14</b>
2.1. The Zeeman Interaction and the NMR Response.....	14
2.2. Birdcage RF Coils.....	16
2.3. Spatial Localization.....	17
2.3.1. Slice Selection.....	19
2.3.2. Nuclear Spin Relaxation.....	20
2.3.3. Spin-Density, k-space, and Spatial Encoding.....	22
2.4. Gradient-Echo and Spin-Echo Experiments.....	26
2.5. Resolution and S/N.....	27
2.6. Contrast.....	29
2.7. Image Artefacts.....	29
2.8. Summary.....	31
2.9. References.....	31
<b>Chapter 3. Background and Theory: PEMFCs .....</b>	<b>34</b>
3.1. PEMFC Components and Reactions.....	34
3.1.1. Proton Transport in Nafion.....	36
3.1.2. Catalysts and Reactions.....	39
3.2. Water and PEMFCs.....	41
3.3. Fuel Cell Diagnostic Techniques.....	42

3.4.	Summary.....	44
3.5.	References.....	45
<b>Chapter 4.</b>	<b>PEMFCs and Experimental Setup.....</b>	<b>50</b>
4.1.	Construction of PEMFCs.....	50
4.1.1.	30 mm PEMFC.....	50
4.1.2.	10 mm PEMFC.....	52
4.1.3.	Preparation of the Membrane Electrode Assemblies.....	53
4.2.	Experimental Methods.....	54
4.2.1.	Gas Supply and Measuring PEMFC Performance.....	54
4.2.2.	<sup>1</sup> H NMR Microscopy: Setup.....	58
4.2.3.	<sup>1</sup> H NMR Microscopy: Considerations.....	59
4.3.	Summary.....	61
4.4.	References.....	61
<b>Chapter 5.</b>	<b><sup>1</sup>H NMR Microscopy: Non-Operating PEMFCs.....</b>	<b>63</b>
5.1.	Slice Selection and Image Content.....	63
5.1.1.	30 mm PEMFC.....	63
5.1.2.	10 mm PEMFC.....	67
5.2.	Influence of Materials on the NMR Signal.....	67
5.3.	Image Algebra – What is the Difference?.....	71
5.4.	Summary.....	72
5.5.	References.....	73
<b>Chapter 6.</b>	<b>The Distribution of Water in an Operating PEMFC.....</b>	<b>74</b>
6.1.	Introduction.....	74
6.2.	Experimental Details.....	75
6.3.	Diffusion of Water away from the MEA.....	75
6.4.	Water in the MEA and Flow Fields.....	77
6.4.1.	In-plane Distribution of H <sub>2</sub> O .....	78

6.4.2. Effect of Gas Flow Direction.....	85
6.4.3. Effect of H <sub>2</sub> O( <i>l</i> ) Accumulation in the Cathode Flow Field on Performance.....	90
6.5. Conclusions.....	92
6.6. References.....	93
<b>Chapter 7. Use of Hydrogen-Deuterium Exchange to Introduce Image Contrast.....</b>	<b>96</b>
7.1. Introduction.....	96
7.2. Experimental Details.....	96
7.3. Contrast Introduced <i>via</i> Use of D <sub>2</sub> O( <i>l</i> ).....	97
7.4. Contrast Introduced by Alternating between H <sub>2</sub> ( <i>g</i> ) and D <sub>2</sub> ( <i>g</i> ) as Fuel.....	104
7.5. Conclusions.....	110
7.6. References.....	111
<b>Chapter 8. PEMFC Performance and Integral of <sup>1</sup>H NMR Microscopy Image Intensity.....</b>	<b>113</b>
8.1. Introduction.....	113
8.2. Experimental Details.....	114
8.3. Correlation Between PEMFC Performance and Image Intensity Integral.....	115
8.3.1. The Region of Interest and Influence of Gas Flow Configuration.....	115
8.3.2. Influence of O <sub>2</sub> ( <i>g</i> ) Flow Rate.....	120
8.3.3. Influence of Power Density.....	125
8.4. Toward Quantification of the Amount of Water in the PEM.....	127
8.5. Conclusions.....	129
8.6. References.....	130

<b>Chapter 9. Concluding Remarks.....</b>	<b>134</b>
9.1. References.....	136
<b>Chapter 10. Future Research Directions and Challenges.....</b>	<b>137</b>
10.1. NMR Techniques.....	137
10.2. H <sub>2</sub> /O <sub>2</sub> PEMFCs.....	137
10.2.1. Water in the MEA.....	137
10.2.2. Variable Temperature Studies.....	138
10.3. Direct Alcohol PEMFCs.....	139
10.4. PEM Pre-Treatment and MEA Preparation.....	140
10.5. New Materials and Designs.....	141
10.6. References.....	141
<b>Appendix A. List of Publications.....</b>	<b>143</b>
A.1. Publications Based on Material in this Thesis.....	143
A.2. Other Publications Resulting from Ph.D. Research.....	144
<b>Appendix B. You and Your PEMFC.....</b>	<b>146</b>
B.1. Maintenance.....	146
B.2. Assembly.....	148
B.2.1. 30 mm PEMFC.....	148
B.2.2. 10 mm PEMFC.....	149
B.3. Conditioning.....	152
B.4. Long-Period Operation.....	152
<b>Appendix C. User Scale Mapping of Image Intensity.....</b>	<b>154</b>

## List of Tables

<b>Table 3-1.</b>	Protonic conductivity of acid-form Nafion-117 as a function of water content.....	36
<b>Table 3-2.</b>	Summary of $^1\text{H}$ translational diffusion rates for pure $\text{H}_2\text{O}(l)$ and $\text{H}_2\text{O}$ in acid-form Nafion-117.....	38
<b>Table 4-1.</b>	Summary of $^1\text{H}$ NMR spin-lattice relaxation times, $T_1$ , for pure $\text{H}_2\text{O}(l)$ and $\text{H}_2\text{O}$ in Nafion-117.....	60
<b>Table 6-1.</b>	The power, current, and voltage measured from the 30 mm PEMFC after the $\text{O}_2(g)$ flow rate was increased from 2.5 to 50 $\text{mL min}^{-1}$ at $t = 0$ .....	81
<b>Table 6-2.</b>	The power, current, and voltage measured from the 30 mm PEMFC after the $\text{O}_2(g)$ flow rate was reduced from 50 to 2.5 $\text{mL min}^{-1}$ at $t = 0$ .....	83
<b>Table 7-1.</b>	The time that the 30 mm PEMFC operated on $\text{H}_2(g)$ at the indicated power prior to acquiring the image of the MEA used in the calculation of the signal recovery MEA difference image shown in Figure 7-4.....	103
<b>Table 7-2.</b>	The time that the PEMFC operated on $\text{D}_2(g)$ or $\text{H}(g)$ at the indicated power prior to acquiring the image of the MEA used in the calculation of the signal loss or signal recovery images shown in Figure 7-7.....	110
<b>Table 8-1.</b>	The area and integrated $^1\text{H}$ NMR signal intensity for each of the ROIs shown in Figure 8-1c to e.....	116
<b>Table 8-2.</b>	The integrated $^1\text{H}$ NMR signal intensities for the images shown in Figure 8-2 for the ROI defined in Figure 8-1c to e.....	118

## List of Figures

<b>Figure 1-1.</b>	Representation of a PEMFC.....	1
<b>Figure 2-1.</b>	Zeeman energy levels for a nucleus with $I = \frac{1}{2}$ .....	15
<b>Figure 2-2.</b>	Representation of a high-pass birdcage resonator.....	17
<b>Figure 2-3.</b>	Effect of a magnetic field gradient on $B_0$ and $\nu_L$ .....	18
<b>Figure 2-4.</b>	Representation of imaging gradient coils.....	18
<b>Figure 2-5.</b>	Time and frequency domain profiles of a sinc-3 RF pulse.....	19
<b>Figure 2-6.</b>	Effect of a slice-select gradient on the NMR response and corresponding Bloch diagram.....	20
<b>Figure 2-7.</b>	A two-dimensional GE pulse sequence and k-space representation.....	24
<b>Figure 2-8.</b>	Comparison of $T_2^*$ and $T_2$ .....	26
<b>Figure 2-9.</b>	SE pulse sequence with gradient pulses and corresponding Bloch diagram.....	27
<b>Figure 3-1.</b>	Schematic of the components of a typical PEMFC.....	34
<b>Figure 3-2.</b>	Representation of the chemical composition of Nafion.....	35
<b>Figure 3-3.</b>	Mechanisms of proton transport in Nafion.....	37
<b>Figure 4-1.</b>	Representation, assembly schematic, and photograph of the 30 mm PEMFC.....	51
<b>Figure 4-2.</b>	Photographs of the disassembled and assembled 30 mm PEMFC.....	52
<b>Figure 4-3.</b>	Assembly schematic and photographs of the 10 mm PEMFC.....	53
<b>Figure 4-4.</b>	Example of a gas inlet/outlet configuration and direction of gas flow for the 30 mm PEMFC.....	55

<b>Figure 4-5.</b>	Graph of power, potential, and current versus time for the 30 mm PEMFC showing a mutual response of the potential and current.....	56
<b>Figure 4-6.</b>	Example polarization curves for the 10 mm and 30 mm PEMFCs.....	56
<b>Figure 4-7.</b>	Schematic of a typical experimental setup used to perform NMR microscopy studies of an operating PEMFC in the vertical wide-bore 7.05 T magnet.....	58
<b>Figure 4-8.</b>	Example polarization curve measured from the 30 mm PEMFC operating in- and outside the external applied magnetic field.....	59
<b>Figure 5-1.</b>	Schematic indicating the orientation of the three basic slice orientations relative to the 30 mm PEMFC and the corresponding $^1\text{H}$ NMR microscopy images.....	64
<b>Figure 5-2.</b>	A series of images showing various orientations of a surface projection generated from a three dimensional GE dataset.....	65
<b>Figure 5-3.</b>	An axial image of the 30 mm PEMFC filled with water and a schematic showing the dimensions of the MEA and flow fields.....	65
<b>Figure 5-4.</b>	Images of the MEA and cathode flow field of the 30 mm PEMFC showing the results from different thickness slices and a photograph of the O-ring and flow field.....	66
<b>Figure 5-5.</b>	Schematic indicating the two basic slice orientations relative to the 10 mm PEMFC and the corresponding images.....	68
<b>Figure 5-6.</b>	A cross-sectional image obtained from the 10 mm PEMFC and corresponding schematic showing the impact of the GDL on the $^1\text{H}$ NMR microscopy image.....	69



<b>Figure 5-7.</b>	Example of the calculation of difference images to show the change in water content between two images.....	72
<b>Figure 6-1.</b>	$^1\text{H}$ NMR microscopy images from a slice containing the MEA of the 30 mm PEMFC showing the diffusion of water radially outward from the catalyst region during fuel cell start up.....	76
<b>Figure 6-2.</b>	$^1\text{H}$ NMR microscopy images of the PEMFC showing the non-uniform distribution of water in the PEM between the catalyst layers and the accumulation of $\text{H}_2\text{O}(l)$ in the cathode flow field....	78
<b>Figure 6-3.</b>	Representation of the top of the 30 mm PEMFC showing the gas inlets/outlets and the direction of gas flow through the anode and cathode flow fields.....	80
<b>Figure 6-4.</b>	$^1\text{H}$ NMR microscopy images of the MEA and cathode flow field, and the MEA difference images showing the decline of water when the $\text{O}_2(g)$ flow rate was increased from 2.5 to 50 $\text{mL min}^{-1}$ .....	81
<b>Figure 6-5.</b>	$^1\text{H}$ NMR microscopy images of the MEA and cathode flow field, and the MEA difference images showing the recovery of water when the $\text{O}_2(g)$ flow rate was decreased from 50 to 2.5 $\text{mL min}^{-1}$ .....	83
<b>Figure 6-6.</b>	Schematic of the model postulated by Büchi and Srinivasan for water flux across the MEA in a self-humidifying counter flow PEMFC.....	85
<b>Figure 6-7.</b>	The four possible gas flow configurations for the 30 mm PEMFC, the resulting distribution of water in the MEA and cathode flow field, and the corresponding operating times and power output.....	87

<b>Figure 6-8.</b>	Schematic of a model for water flux across the MEA in a self-humidifying co-flow PEMFC.....	89
<b>Figure 6-9.</b>	$^1\text{H}$ NMR microscopy images summarizing the effect of the onset of $\text{H}_2\text{O}(l)$ accumulation in the cathode flow field on the cell power output.....	91
<b>Figure 7-1.</b>	Representation of the top of the 30 mm PEMFC showing the gas inlets/outlets and the direction of gas flow through the cathode and anode flow fields.....	98
<b>Figure 7-2.</b>	$^1\text{H}$ NMR microscopy images of the MEA in the 30 mm PEMFC showing the decline in signal upon cycling $\text{D}_2\text{O}(l)$ through the cathode flow field.....	98
<b>Figure 7-3.</b>	$^1\text{H}$ NMR microscopy images of the MEA in the 30 mm PEMFC showing the increase in signal upon operating the cell on $\text{H}_2(g)$ after cycling $\text{D}_2\text{O}(l)$ through the cathode flow field.....	99
<b>Figure 7-4.</b>	The four possible gas flow configurations for the 30 mm PEMFC, the corresponding MEA difference images showing the decline in $^1\text{H}$ NMR signal caused by cycling $\text{D}_2\text{O}(l)$ through the cathode or anode flow field, and the increase in signal upon operating the cell on $\text{H}_2(g)$ .....	103
<b>Figure 7-5.</b>	$^1\text{H}$ NMR microscopy images of the MEA and the cathode flow field, and the MEA difference images showing the decrease in signal while operating the PEMFC on $\text{D}_2(g)$ as fuel.....	105
<b>Figure 7-6.</b>	$^1\text{H}$ NMR microscopy images of the MEA and the cathode flow field, and the MEA difference images showing the increase in signal after switching the fuel from $\text{D}_2(g)$ to $\text{H}_2(g)$ .....	108

<b>Figure 7-7.</b>	The four possible gas flow configurations for the 30 mm PEMFC, the corresponding MEA difference images showing the decline in $^1\text{H}$ NMR signal when using $\text{D}_2(\text{g})$ as fuel, and the subsequent increase in signal when using $\text{H}_2(\text{g})$ as fuel.....	110
<b>Figure 8-1.</b>	Photograph of the O-ring, Au ring, and flow field of the 30 mm PEMFC, $^1\text{H}$ NMR microscopy image from a slice containing the MEA, and the defined ROIs.....	116
<b>Figure 8-2.</b>	The four possible gas flow configurations for the 30 mm PEMFC and example ROIs in $^1\text{H}$ NMR microscopy images from a slice containing the MEA.....	118
<b>Figure 8-3.</b>	Plot of power density and integrated $^1\text{H}$ NMR signal intensities versus time and corresponding $^1\text{H}$ NMR microscopy images showing the effect of changes to the $\text{O}_2(\text{g})$ flow rate on power, MEA water content, and $\text{H}_2\text{O}(\text{l})$ in the cathode flow field.....	121
<b>Figure 8-4.</b>	Plot of power density and integrated $^1\text{H}$ NMR signal intensities versus time and corresponding $^1\text{H}$ NMR microscopy images showing the sensitivity of the power density, MEA water content, and $\text{H}_2\text{O}(\text{l})$ in the cathode flow field to changes in the $\text{O}_2(\text{g})$ flow rate.....	124
<b>Figure 8-5.</b>	Plot of power density and integrated $^1\text{H}$ NMR signal intensities versus time and corresponding $^1\text{H}$ NMR microscopy images showing the effect of changes in the external circuit resistance and the $\text{O}_2(\text{g})$ flow rate on power, MEA water content, and $\text{H}_2\text{O}(\text{l})$ in the cathode flow field.....	125
<b>Figure 10-1.</b>	$^1\text{H}$ NMR microscopy image showing the different signal intensity in the hot-pressed regions of the PEM.....	140

<b>Figure B-1.</b>	Dies for punching the latex O-rings for the 10 mm PEMFC.....	146
<b>Figure B-2.</b>	Tool for use with the screws through which the Au wire is placed in the 10 mm PEMFC.....	147
<b>Figure B-3.</b>	Dies for punching GDLs and the MEA for the 10 mm PEMFC.....	149
<b>Figure B-4.</b>	The jig used for assembling the 10 mm PEMFC.....	150
<b>Figure B-5.</b>	The wrench for use with the 10 mm PEMFC assembly.....	151
<b>Figure B-6.</b>	The shims used for centring the MEA of the 10 mm PEMFC in the 10 mm birdcage, and the platform for the top of the probe-head.....	152

## List of Symbols and Abbreviations

$\alpha$	flip-angle of RF excitation pulse
atm	atmosphere
a.u.	arbitrary units
$\mathbf{B}_0$	static applied magnetic field vector
$B_0$	component of $\mathbf{B}_0$ the z-direction
$B_1$	magnetic component of RF field applied perpendicular to $B_0$
$B_x, B_y, B_z$	components of the $\mathbf{B}_0$ column vector
BW	bandwidth
$\chi$	humidity ratio
cm	centimetre
C	Coulomb
CP-MG	Carr-Purcell Meiboom-Gill experiment
$\delta$	duration of the gradient pulse for diffusion measurements
$\Delta$	time between application of gradient pulses for diffusion measurements
$\Delta E$	energy difference between Zeeman energy levels
$\Delta G^{\circ}_f$	molar Gibb's free energy
$\Delta t$	dwel time
$\Delta k_i$	distance between points along the $i$ -axis of $\mathbf{k}$ -space
$\Delta \nu$	change in resonance frequency due to magnetic field gradient
$\Delta x$	pixel size
$D$	diffusion constant
EW	equivalent weight
$F$	Faraday constant
FE	frequency encoding
FI	Fourier imaging

FID	free induction decay
FOV	field of view
FT	Fourier transform
$\gamma$	magnetogyric ratio
G	conductance
<b>G</b>	magnetic field gradient vector
$G_i$	magnetic field gradient along the $i$ -direction
$G_{ss}$	slice select gradient
GDL	gas diffusion layer
GE	gradient echo
$h$	Planck constant
$\hbar$	Planck constant divided by $2\pi$
h	hour
$\mathcal{H}$	Zeeman Hamiltonian
Hz	hertz
$\text{H}_2\text{O}(pem)$	water in the PEM
$\mathbf{I}\hbar$	nuclear spin angular momentum vector
I	electrical current
$I$	nuclear spin quantum number
$\varphi$	relative humidity
<b>k</b>	reciprocal space vector
$k_x$	frequency encode direction of <b>k</b> -space
$k_y$	phase encode direction of <b>k</b> -space
K	Kelvin
kHz	kilohertz

kPa	kilopascal
$\lambda$	$n\text{H}_2\text{O}/\text{SO}_3\text{H}$
$\mu\text{L}$	microliter
$\mu\text{m}$	micrometer
$\mu\text{s}$	microsecond
m	meter
$m_I$	nuclear spin state
$m_x$	rate of production of $x$ in $\text{mol s}^{-1}$
mA	milliamp
mg	milligram
min	minute
mm	millimetre
ms	millisecond
mW	milliwatt
$M_0$	thermal equilibrium magnetization
$M_x$	molecular weight of species $x$
$M_{x,y}$	magnetization in the $x,y$ plane
$M_z(t)$	magnetization along $z$ at time $t$ after an RF pulse
MHz	megahertz
MEA	membrane electrode assembly
MPa	megapascal
MRI	magnetic resonance imaging
MTX	dimensions of $\mathbf{k}$ -space
NMR	nuclear magnetic resonance
$N_x$	dimension of $\mathbf{k}$ -space along frequency encode axis

$N_y$	dimension of $\mathbf{k}$ -space along phase encode axis
$\nu_{1/2}$	line-width of NMR resonance at half-height
$\nu_L$	Larmor frequency
$P$	total pressure
$p_{vs}$	saturation pressure
PE	phase encode
PEM	proton-exchange membrane
PEMFC	proton-exchange membrane fuel cell
PG	pulsed gradient
pu	pixel unit
$r$	length of vector in space
rad	radian
$\langle r^2 \rangle^{1/2}$	root mean square displacement
RF	radio frequency
ROI	region of interest
$\rho(\mathbf{r})$	spin-density at $\mathbf{r}$
$\sigma$	conductivity
s	second
S	Siemens
SG	static gradient
SE	spin echo
S/N	signal-to-noise ratio
$S(\mathbf{k})$	NMR signal in reciprocal space
$S(t)$	NMR signal as a function of time
$\tau$	duration of magnetic field gradient



T	Tesla
T	temperature
<i>t</i>	time
<i>t<sub>PE</sub></i>	duration of PE gradient pulse
<i>t<sub>zc</sub></i>	time from the centre of an RF pulse to the first zero crossing
<i>T<sub>1</sub></i>	longitudinal or spin-lattice relaxation time
<i>T<sub>2</sub></i>	transverse or spin-spin relaxation time
<i>T<sub>2</sub><sup>*</sup></i>	apparent spin-spin relaxation time
<i>T<sub>A</sub></i>	acquisition time
<i>T<sub>E</sub></i>	echo time
<i>T<sub>R</sub></i>	repetition time
TFE	tetrafluoroethylene
V	volt
<i>V<sub>probe</sub></i>	volume of the RF coil
<i>V<sub>voxel</sub></i>	volume of a voxel
wt%	weight %
<i>x, y, z</i>	lab-frame coordinate system
<i>x', y', z'</i>	rotating-frame coordinate system

## Chapter 1. Introduction and Objectives

### 1.1. Introduction

The subject of this Thesis is the application of  $^1\text{H}$  nuclear magnetic resonance, NMR, microscopy (*i.e.*, magnetic resonance imaging, MRI) to study the distribution of water throughout an operating proton-exchange membrane fuel cell, PEMFC[1]. In this chapter a brief introduction to the development of PEMFCs is given, leading to the motivation and necessity for this research. As well, NMR microscopy is introduced with emphasis on its suitability for investigating operating PEMFCs. In the final section of this chapter the specific objectives of this research are presented together with an outline of subsequent chapters.

#### 1.1.1. Proton-Exchange Membrane Fuel Cells

PEMFCs (Figure 1-1) are an attractive alternative for producing clean energy from renewable resources, particularly for automobiles[2], homes[3], and portable electronic devices[4]. The primary incentives for research involving hydrogen-fuelled PEMFCs are that in principle, the fuel cell will produce only water as exhaust, and the theoretical energy efficiency is greater than 80 %[5]. Other

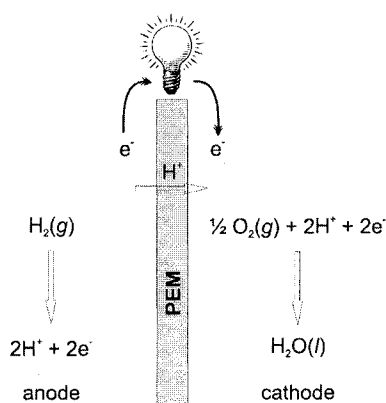


**Figure 1-1.** Representation of a PEMFC operating on  $\text{H}_2(\text{g})$  as fuel.  $\text{H}_2(\text{g})$  is oxidized over the anode catalyst, protons are transferred from the anode through the membrane to the cathode, and electrons are conducted through an external circuit. At the cathode catalyst, protons and electrons reduce  $\text{O}_2(\text{g})$  to produce  $\text{H}_2\text{O}(\text{l})$ .

incentives include few moving parts, low noise, scalability to demand, and mobility. The rapidly increasing reliance on fossil fuels for energy, and the environmental impact of conventional energy production from fossil fuels, mandates efforts to develop cleaner, more efficient methods to produce energy such as PEMFCs.

The term fuel cell was coined by Rideal and Evans in 1922[6]; however, the first reported experimental demonstration of a fuel cell was in 1839 by Grove who fed hydrogen and oxygen over platinum electrodes into aqueous sulphuric acid to produce, what he termed, a "gaseous voltaic battery"[7]. Although the electrochemical reaction producing the electrical current and voltage was thought to take place at the surface of the electrode, not until 1882 did Lord Rayleigh demonstrate that the performance could be improved by increasing the surface area of the electrode by using platinum gauze[8]. In 1889 Mond and Langer introduced the use of a solid matrix to contain the electrolyte and improve catalyst performance by preventing wetting of the platinum black[9]; this represents the first prototype of a practical fuel cell. Over the years numerous classes of fuel cells have been developed including: solid oxide, molten carbonate, alkaline, phosphoric acid, and proton-exchange membrane, PEM[10,11]. Detailed information regarding the history, components, and applications of the various fuel cell systems can be found in recent monographs[5,10,11].

PEMFCs, also commonly referred to as polymer electrolyte or solid-polymer electrolyte fuel cells, were developed to overcome difficulties encountered with sealing and circulation in liquid alkaline electrolyte systems[10]. PEMFCs were reported by General Electric in 1960[12] and used to provide power for the Gemini 5 space mission in 1965[13]. However, the first PEMs, based on a composition of polystyrene sulfonic acid mixed with polychlorotrifluoroethylene (Kel-F), were vulnerable to degradation by  $H_2O_2$ . In 1972, a polymer that was stable in the

presence of halogens (except fluorine), sulfuric acid, and  $\text{H}_2\text{O}_2$  was introduced by E. I. du Pont de Nemours and Company, and registered shortly thereafter as Nafion[14,15]. Nafion remains the industry standard for fuel cell PEMs. A detailed description of modern PEMFC components, including the structure and morphology of Nafion, is in Chapter 3.

There are a number of obstacles that have prevented the economic, widespread use of hydrogen PEMFCs[1,16,17]. These include the storage and availability of pure  $\text{H}_2(\text{g})$ [18-21], the high cost of PEMs, low to moderate long-term operating stability, and robustness. The conductivity of Nafion depends on its water content[22,23]; therefore, the operating conditions of PEMFCs are closely related to the amount and distribution of water throughout the PEMFC, and the properties of water within the PEM[1]. This is the motivation for *in-situ* investigations of the distribution of water throughout operating PEMFCs. The amount of water in the components of an operating PEMFC, or stacks thereof, is dynamic, and depends upon operating conditions such as cell voltage, current, temperature, gas humidification, and gas flow rates[23,24]. PEMs also expand as the water content increases[25] and stacks of fuel cells bundled in series may therefore expand or contract as a consequence. The number of freeze-thaw cycles a stack of fuel cells can undergo without failure and the freeze-start characteristics of the stack are both related to the amount of water in the system[26]. The ability to simultaneously and accurately monitor water throughout an operating PEMFC or stack is essential to engineer the PEMs, fuel supply systems, flow fields, exhaust manifolds, *etc.*, and thus to achieve robust, high-performance PEMFC systems. A plethora of studies characterizing and modeling the components of PEMFCs and their performance, as well as several recent reviews, are in the literature[27-33].

Over the past 30 years NMR spectroscopy investigations have improved [28], and continue to improve[34,35] the understanding of the morphology of PEMs, the state and behaviour of water within them, and the mechanisms of proton conduction. Within the past decade, various approaches have been reported to visualize and investigate an operating PEMFC. These methods include electron paramagnetic resonance investigations of PEM degradation[36,37], the construction of PEMFCs using transparent materials[38-47], the use of neutron[48-56] and infrared thermal imaging[57], and now  $^1\text{H}$  NMR microscopy[58-69]. Both neutron imaging and  $^1\text{H}$  NMR microscopy have enabled the visualization of areas within an operating PEMFC not observable by direct optical methods. Of these techniques,  $^1\text{H}$  NMR microscopy is an accessible, non-invasive, and sensitive technique with the potential to measure and spatially resolve proton density and to impart a variety of molecular-interaction based image contrast[70-72].

#### 1.1.2. Magnetic Resonance Imaging

MRI is perhaps the most publicly recognized application of the NMR phenomenon. Within a decade of the first independently reported demonstrations of the use of magnetic field gradients to spread the frequency of an NMR signal and encode spatial information, in the early 1970s by Paul Lauterbur[73] and Peter Mansfield[74], clinical trials of biomedical applications were commencing[75]. The potential utility of MRI for non-invasive diagnostics of biological tissues spurred remarkable advances in radiofrequency, magnet, and gradient capabilities to accommodate improvements in experimental methodology. The impact of MRI on *in-situ* medical diagnostics has been revolutionary, and in 2003 Lauterbur and Mansfield shared the Nobel Prize in Medicine or Physiology for their discoveries concerning “magnetic resonance imaging”[76,77]. Below is a brief history of the development of the technique.

Lauterbur, a chemist by training, had observed the sacrifice and dissection of rats to remove cancerous and healthy tissue samples for  $^1\text{H}$  NMR relaxation measurements. He found the experience rather distasteful and was curious if these measurements could be completed from outside the living body[77]. Capitalizing on the relation between the frequency of an NMR signal and the strength of the external magnetic field, Lauterbur employed the linear shim gradients on a 60 MHz NMR spectrometer to modulate the magnetic field. Completing a series of careful measurements and a mathematical transformation of the data, Lauterbur obtained a spatially resolved image of two capillaries filled with water. After coining the term zeugmatography (from the Greek *zeugma* meaning connection or yoke) to describe the process, the manuscript with hand-drawn results (referred to as zeugmatograms, rather than images) was submitted to *Nature*, and rejected until the revised version[73] contained references to biological tissues and cancer[77].

In the Department of Physics and Astronomy at the University of Nottingham, Mansfield and coworkers were investigating multiple-pulse line-narrowing NMR experiments in solids and were curious if a linear field gradient would reveal the molecular structure of the sample[76]. Although unsuccessful in resolving the structure, in 1973 they reported the use of field gradients to introduce a spatial dependence in the NMR signal in solids and the use of the Fourier transform to process the signal[74]. Shortly thereafter, they demonstrated the use of selective irradiation to define a thin slice of material to limit the region from which an image was obtained[78], and introduced the use of spin-echoes to reduce the experimental acquisition time by several orders of magnitude[79]. Later, Mansfield introduced active shielding of the static applied field from the pulsed gradients which enabled the use of strong gradients to define the slices and image axes[80,81].

The achievable resolution of MRI is ultimately limited by the frequency and relaxation of the NMR signal and is on the order of  $\mu\text{m}$ [82,83], comparable to that of optical microscopy and hence, the term “NMR microscopy” is often used for materials imaging[84]. Although X-ray or neutron source techniques for materials characterization can achieve atomic scale resolution, the variety of image contrasts that can be obtained based on the sensitivity of NMR parameters to molecular interactions[70] makes the technique extremely robust and the applications diverse. Application of MRI outside of the life sciences realm is often technically challenging due to the non-aqueous or heterogeneous composition of the materials of interest[85]. NMR microscopy techniques have been developed and utilized in a variety of materials and processes including the study of complex fluids[86], concrete building materials[87], seed germination[88], drug release from tablets[89], and food property characterization[90-93]. A PEMFC has a heterogeneous material composition, including semi-aqueous and aqueous components suitable for investigation *via* NMR microscopy. The principles of NMR microscopy as related to this Thesis are covered in Chapter 2.

## 1.2. Thesis Objectives and Outline

The paramount objective of the research presented in this Thesis is to establish the feasibility of using  $^1\text{H}$  NMR microscopy to provide experimental insight into the relationship between the water content in, and the performance of, operating PEMFCs. Specific goals of the research were developed as the potential of the technique was realized.

The first step of the project, as detailed in Chapter 4, was to design and construct PEMFCs that would fit within the available imaging hardware, and to determine if the PEMFCs would operate within the strong static and pulsed magnetic fields required to perform the  $^1\text{H}$  NMR microscopy experiments. Images

of the PEMFCs filled with water, presented in Chapter 5, were acquired to show the perspective and dimensions of the inside of the PEMFCs. The effects of some materials used in the PEMFCs on the  $^1\text{H}$  NMR signal are evident and potential limitations with respect to attainable resolution are considered. Presented in Chapter 6 are results from the preliminary exploration of using  $^1\text{H}$  NMR microscopy as a diagnostic tool to garner information about the distribution of water in operating PEMFCs. The effects of gas flow rate and inlet/outlet configuration on the in-plane distribution of water in the PEM between the operating catalyst layers and the cathode flow channels are studied. In addition, the results are discussed with respect to specific hypotheses, inferences, observations, and theoretical predictions within the vast PEMFC literature. The use of H-D exchange to introduce contrast in the  $^1\text{H}$  NMR microscopy images of water within the PEM is investigated (Chapter 7). In Chapter 8, correlation between the integral intensities of  $^1\text{H}$  NMR microscopy images and PEMFC operating conditions is explored and the potential of quantifying the amount of water in the PEM of an operating PEMFC is discussed. A brief summary of results and conclusions is provided in Chapter 9. The results presented in this Thesis demonstrate that  $^1\text{H}$  NMR microscopy is a valuable technique to elucidate important information regarding the interdependence of PEMFC water content, gas flow rates and configuration, and PEMFC performance. Recommendations for future investigations and possible challenges are offered in Chapter 10.

### 1.3. References

- [1] Eikerling, M.; Kornyshev, A. A.; Kucernak, A. R. *Phys. Today* **2006**, *59*, 38-44.
- [2] Appleby, A. J. *Sci. Am.* **1999**, *281*, 74-79.
- [3] Lloyd, A. C. *Sci. Am.* **1999**, *281*, 80-84,86.



- [4] Dyer, C. K. *Sci. Am.* **1999**, *281*, 88-93.
- [5] Barbir, F. *PEM Fuel Cells: Theory and Practice*; Elsevier Academic Press: San Diego, 2005.
- [6] Rideal, E. K.; Evans, U. R. T. *Faraday Soc.* **1922**, *17*, 0466-0482.
- [7] Grove, W. R. *Philos. Mag. J. Sci.* **1839**, *14*, 127-130.
- [8] Rayleigh, L. P. *Camb. Philos. Soc.* **1882**, *4*, 198.
- [9] Mond, L.; Langer, C. *Proc. R. Soc. Lon.* **1889**, *46*, 296-304.
- [10] Hoogers, G., Ed. *Fuel Cell Technology Handbook*; CRC Press LLC: Boca Raton, 2003.
- [11] Larminie, J.; Dicks, A. *Fuel Cell Systems Explained*; 2nd ed.; John Wiley and Sons Ltd.: Chichester, 2003.
- [12] Grubb, W. T.; Niedrach, L. W. *J. Electrochem. Soc.* **1960**, *107*, 131-135.
- [13] Cohen, R. In *20th Annual Power Sources Conference*: New Jersey, 1966.
- [14] Grot, W. *Chem. Ing. Tech.* **1972**, *44*, 167-169.
- [15] Grot, W. *Chem. Ing. Tech.* **1975**, *47*, 617-617.
- [16] Steele, B. C. H.; Heinzl, A. *Nature* **2001**, *414*, 345-352.
- [17] Service, R. F. *Science* **2004**, *305*, 958-961.
- [18] Schneider, D. *Am. Sci.* **2005**, *93*, 410-411.
- [19] Brown, L. F. *Int. J. Hydrogen Energy* **2001**, *26*, 381-397.
- [20] Schlapbach, L.; Züttel, A. *Nature* **2001**, *414*, 353-358.
- [21] Turner, J. A. *Science* **2004**, *305*, 972-974.
- [22] Slade, R. C. T.; Barker, J.; Strange, J. H. *Solid State Ionics* **1989**, *35*, 11-15.
- [23] Zawodzinski, T. A., Jr.; Derouin, C.; Radzinski, S.; Sherman, R. J.; Smith, V. T.; Springer, T. E.; Gottesfeld, S. *J. Electrochem. Soc.* **1993**, *140*, 1041-1047.

- [24] Williams, M. V.; Kunz, H. R.; Fenton, J. M. *J. Power Sources* **2004**, *135*, 122-134.
- [25] Gebel, G.; Aldebert, P.; Pineri, M. *Polymer* **1993**, *34*, 333-339.
- [26] Knights, S. D.; Colbow, K. M.; St-Pierre, J.; Wilkinson, D. P. *J. Power Sources* **2004**, *127*, 127-134.
- [27] Li, Q.; He, R.; Jensen, J. O.; Bjerrum, N. J. *Chem. Mater.* **2003**, *15*, 4896-4915.
- [28] Mauritz, K. A.; Moore, R. B. *Chem. Rev.* **2004**, *104*, 4535-4585.
- [29] Hickner, M. A.; Ghassemi, H.; Kim, Y. S.; Einsla, B. R.; McGrath, J. E. *Chem. Rev.* **2004**, *104*, 4587-4611.
- [30] Russell, A. E.; Rose, A. *Chem. Rev.* **2004**, *104*, 4613-4635.
- [31] Kreuer, K.-D.; Paddison, S. J.; Spohr, E.; Schuster, M. *Chem. Rev.* **2004**, *104*, 4637-4678.
- [32] Weber, A. Z.; Newman, J. *Chem. Rev.* **2004**, *104*, 4679-4726.
- [33] Wang, C.-Y. *Chem. Rev.* **2004**, *104*, 4727-4765.
- [34] Ye, G.; Janzen, N.; Goward, G. R. *Macromolecules* **2006**, *39*, 3283-3290.
- [35] Traer, J. W.; Montoneri, E.; Samoson, A.; Past, J.; Tuhem, T.; Goward, G. R. *Chem. Mater.* **2006**, *18*, 4747-4754.
- [36] Panchenko, A.; Dilger, H.; Kerres, J.; Hein, M.; Ullrich, A.; Kaz, T.; Roduner, E. *Phys. Chem. Chem. Phys.* **2004**, *6*, 2891-2894.
- [37] Panchenko, A.; Dilger, H.; Möller, E.; Sixt, T.; Roduner, E. *J. Power Sources* **2004**, *127*, 325-330.
- [38] Argyropoulos, P.; Scott, K.; Taama, W. M. *J. Appl. Electrochem.* **1999**, *29*, 661-669.
- [39] Argyropoulos, P.; Scott, K.; Taama, W. M. *Electrochim. Acta* **1999**, *44*, 3575-3584.
- [40] Lu, G. Q.; Wang, C. Y. *J. Power Sources* **2004**, *134*, 33-40.

- [41] Scott, K.; Argyropoulos, P.; Yiannopoulos, P.; Taama, W. M. *J. Appl. Electrochem.* **2001**, *31*, 823-832.
- [42] Tüber, K.; Poćza, D.; Hebling, C. *J. Power Sources* **2003**, *124*, 403-414.
- [43] Yang, X. G.; Zhang, F. Y.; Lubawy, A. L.; Wang, C. Y. *Electrochem. Solid-State Lett.* **2004**, *7*, A408-A411.
- [44] Yang, H.; Zhao, T. S.; Ye, Q. *J. Power Sources* **2005**, *139*, 79-90.
- [45] Yang, H.; Zhao, T. S.; Cheng, P. *Int. J. Heat Mass Tran.* **2004**, *47*, 5725-5739.
- [46] Nordlund, J.; Picard, C.; Birgersson, E.; Vynnycky, M.; Lindbergh, G. *J. Appl. Electrochem.* **2004**, *34*, 763-770.
- [47] Theodorakakos, A.; Ous, T.; Gavaises, M.; Nouri, J. M.; Nikolopoulos, N.; Yanagihara, H. *J. Colloid Interface Sci.* **2006**, *300*, 673-687.
- [48] Bellows, R. J.; Lin, M. Y.; Arif, M.; Thompson, A. K.; Jacobson, D. *J. Electrochem. Soc.* **1999**, *146*, 1099-1103.
- [49] Geiger, A. B.; Tsukada, A.; Lehmann, E.; Vontobel, P.; Wokaun, A.; Scherer, G. G. *Fuel Cells* **2002**, *2*, 92-98.
- [50] Kramer, D.; Lehmann, E.; Frei, G.; Vontobel, P.; Wokaun, A.; Scherer, G. G. *Nucl. Instrum. Methods Phys. Res., Sect. A* **2005**, *542*, 52-60.
- [51] Satija, R.; Jacobson, D. L.; Arif, M.; Werner, S. A. *J. Power Sources* **2004**, *129*, 238-245.
- [52] Pekula, N.; Heller, K.; Chuang, P. A.; Turhan, A.; Mench, M. M.; Brenizer, J. S.; Ünlü, K. *Nucl. Instrum. Methods Phys. Res., Sect. A* **2005**, *542*, 134-141.
- [53] Kramer, D.; Zhang, J.; Shimoi, R.; Lehmann, E.; Wokaun, A.; Shinohara, K.; Scherer, G. G. *Electrochim. Acta* **2005**, *50*, 2603-2614.
- [54] Zhang, J.; Kramer, D.; Shimoi, R.; Ono, Y.; Lehmann, E.; Wokaun, A.; Shinohara, K.; Scherer, G. G. *Electrochim. Acta* **2006**, *51*, 2715-2727.
- [55] Hickner, M. A.; Siegel, N. P.; Chen, K. S.; McBrayer, D. N.; Hussey, D. S.; Jacobson, D. L.; Arif, M. *J. Electrochem. Soc.* **2006**, *153*, A902-A908.

- [56] Schneider, I. A.; Kramer, D.; Wokaun, A.; Scherer, G. G. *Electrochem. Commun.* **2005**, *7*, 1393-1397.
- [57] Wang, M. H.; Guo, H.; Ma, C. F. *J. Power Sources* **2006**, *157*, 181-187.
- [58] Feindel, K. W.; Bergens, S. H.; Wasylishen, R. E. *ChemPhysChem* **2006**, *7*, 67-75.
- [59] Feindel, K. W.; Bergens, S. H.; Wasylishen, R. E. *J. Am. Chem. Soc.* **2006**, *128*, 14192-14199.
- [60] Feindel, K. W.; LaRocque, L. P. A.; Starke, D.; Bergens, S. H.; Wasylishen, R. E. *J. Am. Chem. Soc.* **2004**, *126*, 11436-11437.
- [61] Ha, S.; Dunbar, Z.; Masel, R. *Abstr. Pap. Am. Chem. S.* **2005**, *230*, U1638-U1639.
- [62] Teranishi, K.; Tsushima, S.; Hirai, S. *Therm. Sci. Eng.* **2002**, *10*, 59-60.
- [63] Teranishi, K.; Tsushima, S.; Hirai, S. *Therm. Sci. Eng.* **2003**, *11*, 35-36.
- [64] Teranishi, K.; Tsushima, S.; Hirai, S. *Therm. Sci. Eng.* **2004**, *12*, 91-92.
- [65] Tsushima, S.; Teranishi, K.; Hirai, S. *Energy* **2005**, *30*, 235-245.
- [66] Tsushima, S.; Teranishi, K.; Nishida, K.; Hirai, S. *Magn. Reson. Imaging* **2005**, *23*, 255-258.
- [67] Minard, K. R.; Viswanathan, V. V.; Majors, P. D.; Wang, L.-Q.; Rieke, P. C. *J. Power Sources* **2006**, *161*, 856-863.
- [68] Tsushima, S.; Teranishi, K.; Hirai, S. *Electrochem. Solid-State Lett.* **2004**, *7*, A269-A272.
- [69] Teranishi, K.; Tsushima, S.; Hirai, S. *J. Electrochem. Soc.* **2006**, *153*, A664-A668.
- [70] Xia, Y. *Concepts Magn. Reson.* **1996**, *8*, 205-225.
- [71] Callaghan, P. T. *Principles of Nuclear Magnetic Resonance Microscopy*; Oxford University Press: New York, 1991.

- [72] Haacke, E. M.; Brown, R. W.; Thompson, M. R.; Venkatesan, R. *Magnetic Resonance Imaging: Physical Principles and Sequence Design*; John Wiley and Sons: New York, 1999.
- [73] Lauterbur, P. C. *Nature* **1973**, *242*, 190-191.
- [74] Mansfield, P.; Grannell, P. K. *J. Phys. C Solid State* **1973**, *6*, L422-L426.
- [75] Mansfield, P.; Morris, P. G. *NMR Imaging in Biomedicine*; Academic Press: New York, 1982.
- [76] Mansfield, P. *Angew. Chem. Int. Ed.* **2004**, *43*, 5456-5464.
- [77] Lauterbur, P. C. *Angew. Chem. Int. Ed.* **2005**, *44*, 1004-1011.
- [78] Garroway, A. N.; Grannell, P. K.; Mansfield, P. *J. Phys. C Solid State* **1974**, *7*, L457-L462.
- [79] Mansfield, P. *J. Phys. C Solid State* **1977**, *10*, L55-L58.
- [80] Chapman, B.; Mansfield, P. *J. Phys. D Appl. Phys.* **1986**, *19*, L129-L131.
- [81] Mansfield, P.; Chapman, B. *J. Magn. Reson.* **1986**, *66*, 573-576.
- [82] Lee, S. C.; Kim, K.; Kim, J.; Lee, S.; Yi, J. H.; Kim, S. W.; Ha, K. S.; Cheong, C. *J. Magn. Reson.* **2001**, *150*, 207-213.
- [83] Ciobanu, L.; Seeber, D. A.; Pennington, C. H. *J. Magn. Reson.* **2002**, *158*, 178-182.
- [84] Eccles, C. D.; Callaghan, P. T. *J. Magn. Reson.* **1986**, *68*, 393-398.
- [85] Stapf, S.; Han, S.-I., Eds. *Nuclear Magnetic Resonance Imaging in Chemical Engineering*; Wiley-VCH: Weinheim, 2006.
- [86] Callaghan, P. T. *Curr. Opin. Colloid Interface Sci.* **2006**, *11*, 13-18.
- [87] Young, J. J.; Bremner, T. W.; Thomas, M. D. A.; Balcom, B. J. In *NMR Imaging in Chemical Engineering*; Stapf, S., Han, S. I., Eds.; Wiley-VCH: Weinheim, 2006, 285-303.

- [88] Terskikh, V. V.; Feurtado, J. A.; Ren, C. W.; Abrams, S. R.; Kermode, A. R. *Planta* **2005**, *221*, 17-27.
- [89] Fyfe, C. A.; Blazek-Welsh, A. I. *J. Controlled Release* **2000**, *68*, 313-333.
- [90] Kasai, M.; Lewis, A.; Marica, F.; Ayabe, S.; Hatae, K.; Fyfe, C. A. *Food Res. Int.* **2005**, *38*, 403-410.
- [91] McCarthy, M. J. *Magnetic Resonance Imaging in Foods*; Chapman and Hall: New York, 1994.
- [92] Hills, B. P. *Magnetic Resonance Imaging in Food Science*; Wiley Interscience: New York, 1998.
- [93] Ruan, R. R.; Chen, P. L. *Water in Foods and Biological Materials: A Nuclear Magnetic Resonance Approach*; Technomic: Lancaster, 1998.

## Chapter 2. Background and Theory: NMR Microscopy

There is a wide variety of monographs available on the subject of MRI with applications to both medicine and materials science. Over the last several years numerous books have been of value, whether for an introduction to the fundamentals of imaging[1-4], a qualitative overview[5,6], or applications in materials science[7]. This chapter serves to introduce the concepts of NMR microscopy as applied in this Thesis.

Portions of this chapter are reproduced with permission from Feindel, K.W., Bergens, S.H., and Wasylishen, R.E. *ChemPhysChem*, 2006, 7, 67-75. Copyright 2006 Wiley Interscience.

### 2.1. The Zeeman Interaction and the NMR Response

The fundamental interaction between a magnetic field and the magnetic dipole moment associated with the orbital angular momentum of a nucleus was theorized by Hendrik Lorentz and first observed by Pieter Zeeman in 1896[8]. This interaction is the source of the observable NMR response. The Zeeman Hamiltonian describes the energy of interaction of the nuclear spin angular momentum vector,  $\mathbf{I}\hbar$ , with an external applied magnetic field,  $\mathbf{B}_0$ ,

$$\mathcal{H}_Z = -\gamma\mathbf{I}\hbar\mathbf{B}_0 \quad (2-1)$$

where  $\gamma$  is the magnetogyric ratio,  $\hbar$  is the Planck constant  $h$  divided by  $2\pi$ , and the magnetic moment is represented by the product  $\gamma\mathbf{I}\hbar$ . Tables of the nuclear spin properties are available[9]. The largest component of the  $\mathbf{B}_0$  column vector ( $B_x$ ,  $B_y$ ,  $B_z$ ) defines the  $z$ -axis of the laboratory frame of reference. Typically, only the field along this direction is considered and thus  $\mathbf{B}_0 = (0, 0, B_0)$ . The potential energy of a magnetic dipole moment in a magnetic field depends on the projection of the magnetization vector with respect to the field. Considering a proton with nuclear

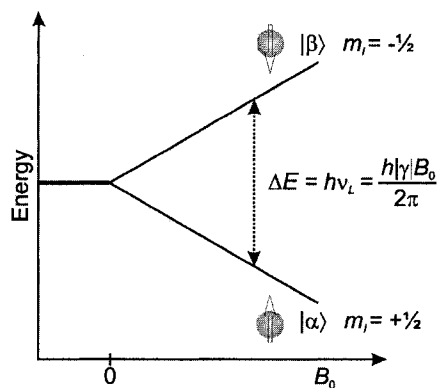


**Figure 2-1.** Zeeman energy levels for a nucleus with  $I = \frac{1}{2}$  demonstrating the separation of the nuclear spin states  $m_l = \pm\frac{1}{2}$  as a function of  $B_0$ .

spin  $I = \frac{1}{2}$ , eigenstates with different energies are obtained for the two possible projections with respect to the applied field: parallel ( $m_l = \frac{1}{2}$ ) and antiparallel ( $m_l = -\frac{1}{2}$ ) (Figure 2-1). The frequency corresponding to the difference in energy between the two states,  $\Delta E$ , is defined by the Larmor equation,

$$\nu_L = \frac{|\gamma|B_0}{2\pi} = \frac{\Delta E}{h} \quad (2-2)$$

where  $\nu_L$  is referred to as the Larmor frequency. Both equations 2-1 and 2-2 show the field-dependent nature of the NMR frequency. Herein we are concerned with the NMR of water, which provides the option of investigating  $^1\text{H}$ ,  $^2\text{H}$ , or  $^{17}\text{O}$ , but  $^1\text{H}$  is the most suitable with the highest natural abundance and the largest  $\gamma$ . The Larmor frequencies of protons in commercial superconducting NMR magnets are on the order of  $10^8$  Hz, or in the radio frequency, RF, range. The experiments to obtain the results presented herein were completed at  $B_0 = 7.05$  T, and for a proton  $\gamma = 26.7522128107 \times 10^7$  rad  $\text{s}^{-1}$   $\text{T}^{-1}$ , thus  $\nu_L$  is  $\sim 300.17$  MHz. If one assumes that an ensemble of isochronous protons in a bulk sample subject to  $B_0$  experience the same local magnetic field, they will exhibit a single coherent resonance at  $\nu_L$ . To generate a detectable NMR response the equilibrium magnetization is disturbed by applying an oscillating magnetic field,  $B_1$ , transverse to the z-axis, with frequency that



matches  $\nu_L$ . The duration and amplitude of the  $B_1$  field determines the extent to which the magnetization rotates about the  $B_1$  field away from the z-axis. Often to facilitate simple vector model diagrams of the magnetization, the lab-frame coordinate system  $(x, y, z)$  is transformed to a frame where the oscillatory  $B_1$  field appears stationary  $(x', y', z')$ , *i.e.*, the coordinate system rotates at the frequency of the RF transmitter.

The  $^1\text{H}$  NMR response to an RF pulse contains a wealth of information regarding the local and long-range environment of the protons within a sample. For example, differences in chemical environment, diffusion, and the magnetic susceptibility of the sample influence the resulting frequencies that are encoded in the NMR response or free-induction decay, FID, and their rates of relaxation. Many of these effects are related to the strength of the applied static magnetic field,  $B_0$ , and provide different mechanisms from which molecular interaction based image contrast can be obtained[1,3,10]. This diverse sensitivity has facilitated the establishment of NMR techniques as some of the most powerful methods for molecular structural elucidation[11], characterization of materials[7,12], and for diagnostic medical imaging[13,14].

## 2.2. Birdcage RF Coils

The static applied magnetic field,  $B_0$ , experienced by the sample must be homogeneous to prevent a spread in  $\nu_L$ . In continuance, the pulsed magnetic field,  $B_1$ , applied transverse to the static applied magnetic field, that generates the measurable NMR response must also be homogeneous. To achieve greater RF uniformity over larger volumes typically required for imaging, a design called the birdcage resonator is often used (Figure 2-2)[15-18]. In principle a standing wave is formed around the cylinder and in the lowest frequency mode will result in a single

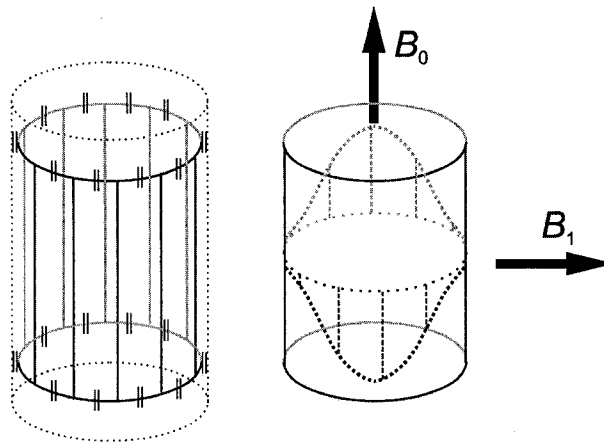


**Figure 2-2.** Representation of a quadrature high-pass birdcage RF resonator. The circuit design results in a sinusoidal variation of current and voltage around the cylinder and creates an oscillating  $B_1$  field in an approximately spherical volume.

wavelength sinusoidal variation in current and voltage around the cylinder[1]. Birdcage resonators are quadrature coils and the magnetization of the RF pulse rotates in a full circle with the proton spins (in contrast to a typical solenoid where the RF pulse is varied only along one axis). Quadrature coils result in reduced RF power deposition and in an increased signal to noise ratio[15].

### 2.3. Spatial Localization

In general, three independent parameters of the NMR response are used for  $^1\text{H}$  NMR microscopy: the amplitude, frequency, and phase. The amplitude of the FID is related directly to the number of protons, *i.e.*,  $^1\text{H}$  nuclei, which provides the fundamental image contrast. By introducing controlled inhomogeneities into  $B_0$ , spatial information about the sample is encoded into the frequency and phase associated with the source FID. For example, when a magnetic field gradient,  $G_y$ , is applied across the sample, the total magnetic field experienced by protons varies with respect to their position within the applied gradient (Figure 2-3). Note that the direction of the magnetic field created by the gradient is in the  $z$ -direction; the subscript  $y$  denotes the axis along which the gradient is positioned. The

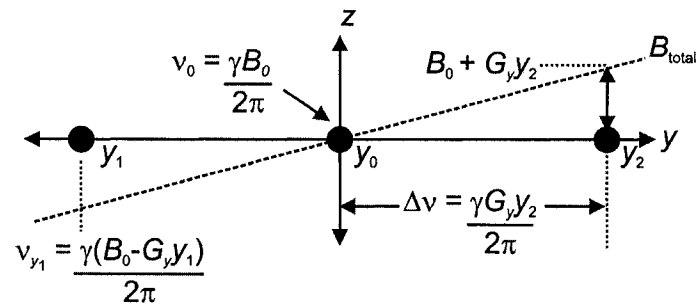


**Figure 2-3.** A magnetic field gradient along the  $y$ -axis,  $G_y$ , modulates the static applied magnetic field along the  $z$ -axis,  $B_0$ . The change in magnetic field is related to the strength of the gradient and the distance from the origin of the axis along which the gradient is applied such that  $B_{total} = B_0 + G_y y$ . As a result the resulting resonance frequency of a spin,  $\nu_y$ , can be related to its position in space with respect to the gradient axis.

corresponding change in resonance frequency,  $\Delta \nu$ , can be described as a function of the applied field gradient and therefore of position in space,  $y$ :  $\Delta \nu(y) = \gamma G_y y$ . To generate the uniform spatially dependent magnetic fields a set of three actively shielded[19] gradient coils surround the RF coil assembly. The magnetic field gradients either add to, or subtract from,  $B_0$ , and the gradient units are designed such that the pulsed magnetic fields increase with distance from the centre of the device. The magnetic field is generated along the  $z$ -axis ( $G_z$ ) using a Maxwell pair[20], and in the mutually orthogonal  $x$ - and  $y$ -directions ( $G_x, G_y$ ) using concentric saddle coils[21,22] (see Figure 2-4).

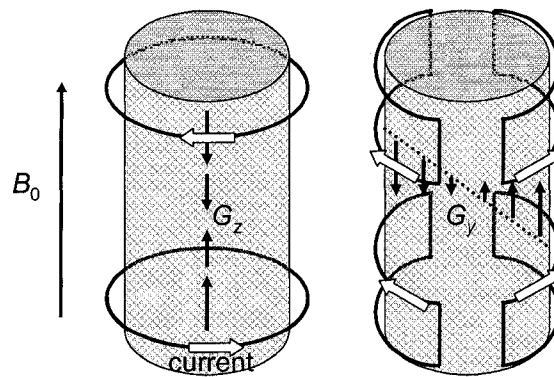


**Figure 2-4.** Representation of the coils used to create magnetic field gradients that vary linearly through space. A Maxwell pair creates the longitudinal gradient field along  $z$ , and a Golay coil configuration creates the transverse  $x$  and  $y$  gradient fields.

### 2.3.1. Slice Selection

One of the major benefits of NMR microscopy as a diagnostic tool is the ability to investigate non-invasively objects in specific regions of interest by defining image slices. This technique, first demonstrated by Mansfield in 1974[23], was one of the critical advances in MRI warranting his receiving the 2003 Nobel Prize in Medicine or Physiology. The slice selection process relies on a magnetic field gradient across the sample creating a spread in  $\nu_L$ . The amplitude of the RF pulse used to generate the detectable NMR signal is often shaped in the time domain such the frequency profile of the  $B_1$  field is approximately square. Shown in Figure 2-5 are the time and frequency domain profiles for a sinc-3 pulse, where  $\text{sinc} = \sin(t)/t$  and the 3 indicates the number of zero crossings. The pulse  $\text{BW} = 1/t_{zc}$ , where  $t_{zc}$  is the time from the centre of the RF pulse to the first zero crossing. The BW of the shaped RF pulse in combination with the applied field gradient defines the region from which the NMR response is generated. For example, if a slice is to be defined using an RF pulse BW of 5 kHz, from Eq. 2-2 the required change in magnetic field over the thickness of the slice is  $\sim 1.174 \times 10^{-4}$  T. The BW of the RF pulse and the maximum gradient strength available determines the minimum slice thickness. For example, with a maximum gradient of  $1 \text{ T m}^{-1}$  (for the hardware used in this research) and an RF pulse  $\text{BW} = 5 \text{ kHz}$  the minimum slice thickness is  $\sim 117 \mu\text{m}$ . As

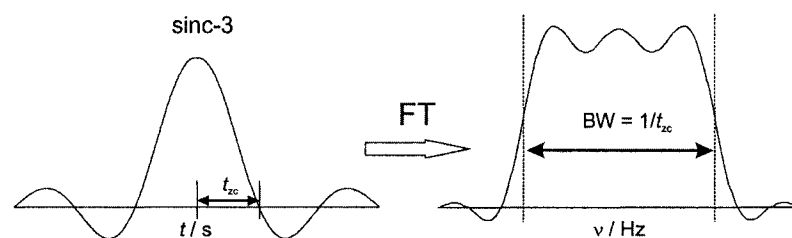


**Figure 2-5.** Time and frequency domain profiles of a sinc-3 RF pulse. Shaped time domain RF pulses are used to provide an approximately square frequency profile of the  $B_1$  field used for slice-selective excitation.

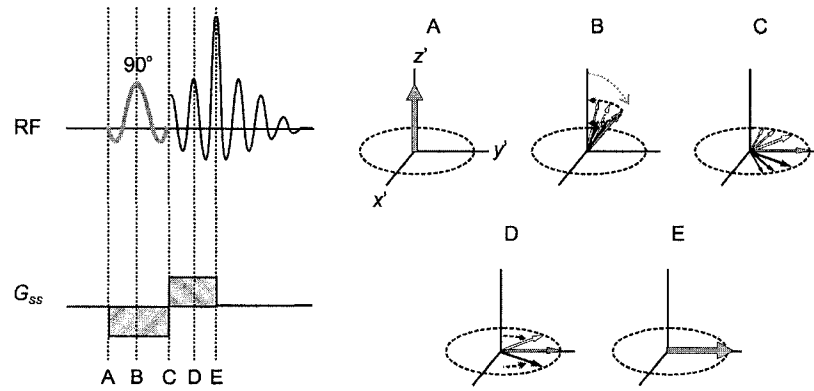


**Figure 2-6.** Representation of the effect of a slice-select gradient,  $G_{ss}$ , on the NMR response during a  $90^\circ$  RF pulse showing the necessity of a refocusing gradient. The time domain of the RF channel and field gradient are shown on the left, and the corresponding Bloch diagrams depicting the magnetization are on the right. The RF pulse (A-C) rotates the magnetization into the  $x',y'$  plane. The slice-select gradient (A-C) is used to create a spread in Larmor frequencies, but also causes the magnetization to lose phase coherence. A field gradient of opposite sign refocuses the in-plane magnetization (C-E).

shown in Figure 2-6, a consequence of the slice selection gradient,  $G_{ss}$ , is a spread in the precession frequencies of the nuclear spins and a loss of phase coherence, and therefore of detectable NMR response. To reverse this dephasing,  $G_{ss}$  is reapplied in the opposite direction to bring the precession of the nuclear spins in the slice back into phase.

The profiles of the RF pulses used for slice excitation are imperfect (*i.e.*, are not rectangular) and for multi-slice acquisition imperfect slice shapes can lead to inadvertent excitation of protons outside the intended image slice. To reduce this effect gaps can be left between neighbouring slices or excitation of the slices can be interlaced to maximize the time elapsing between excitation of adjacent slices.

### 2.3.2. Nuclear Spin Relaxation

At thermal equilibrium the magnetization,  $M_0$ , is in the direction of  $B_0$  along the  $z$ -axis. Application of an RF pulse that rotates the magnetization away from the  $z$ -axis and into the  $x,y$  plane disturbs the equilibrium of the spin system. Over time

the equilibrium will be restored, and the magnetization along the z-axis at time  $t$ ,  $M_z(t)$  can be described using the classical equation of motion derived by Bloch[24]:

$$M_z(t) - M_0 = [M_z(0) - M_0] \exp\left(-\frac{t}{T_1}\right) \quad (2-3)$$

where  $M_z(0)$  is the magnetization remaining along the z-axis after the RF pulse and  $T_1$  is the spin-lattice or longitudinal relaxation time. Similarly, the nuclear spins forming the magnetization rotated into the  $x,y$  plane,  $M_{x,y}$ , will come to thermal equilibrium resulting in no net transverse magnetization. For liquid-state molecules this relaxation process and transverse magnetization at time  $t$ ,  $M_{x,y}(t)$ , can generally be treated using the theory of Bloembergen, Purcell, and Pound[25] and described by Eq. 2-4:

$$M_{x,y}(t) = M_{x,y}(0) \exp\left(-\frac{t}{T_2}\right) \quad (2-4)$$

where  $M_{x,y}(0)$  is the transverse magnetization immediately following the RF pulse and  $T_2$  is the spin-spin or transverse relaxation time. In general,  $T_2 \leq T_1$ . In the absence of paramagnetic materials, aqueous or semi-solid systems containing water with a homogeneous composition tend to exhibit  $^1\text{H}$   $T_2$  values on the order of  $10^{-1}$  s or longer.

As described in §2.3.1, application of a magnetic field gradient will dephase magnetization in the transverse plane, which can be refocused with a gradient of opposite sign. However, if the spins are diffusing the two gradients experienced by the spins will be of different magnitude and an overall attenuation of the transverse magnetization will result. Stejskal and Tanner[26] demonstrated that this principle could be applied to obtain the bulk rate of diffusion,  $D$ , of the species. In the absence of other relaxation mechanisms (*i.e.*,  $T_2$ ), the attenuation of transverse

magnetization due to unrestricted translational diffusion as measured by a pulsed-gradient spin-echo experiment can be expressed as[2]:

$$M_{x,y}(t) = M_{x,y}(0) \exp\left[-\gamma^2 G^2 D \delta^2 \left(\Delta - \frac{\delta}{3}\right)\right] \quad (2-5)$$

where  $G$  is the strength of the applied gradient,  $\delta$  is the duration of the gradient pulse, and  $\Delta$  is the time between application of the two gradient pulses.

### 2.3.3. Spin-Density, $\mathbf{k}$ -space, and Spatial Encoding

The amplitude of the NMR signal acquired as a function of time is denoted  $S(t)$ . In NMR microscopy, the frequency of the signal from a volume of spins at position  $\mathbf{r}$ , *i.e.*, the spin density,  $\rho(\mathbf{r})$ , is a function of the position with respect to the gradient vector,  $\mathbf{G}$ . The signal amplitude integrated over volume has the form of a Fourier transform, FT, and assuming mixing with a reference frequency, can be expressed as[1]:

$$S(t) = \iiint \rho(\mathbf{r}) \exp[i\gamma \mathbf{G} \cdot \mathbf{r} t] d\mathbf{r} \quad (2-6)$$

Mansfield introduced the concept of a reciprocal space vector,  $\mathbf{k}$ , of the form[27-29]:

$$\mathbf{k} = \frac{\gamma \mathbf{G} t}{2\pi} \quad (2-7)$$

which shows that  $\mathbf{k}$ -space can be traversed by gradient magnitude or by time, and that the dimensions of  $\mathbf{k}$ -space are cycles per meter. That is, low spatial frequency information is contained in the centre of  $\mathbf{k}$ -space, such as intensity and contrast, and toward the edges of  $\mathbf{k}$ -space high spatial frequency information is contained, *i.e.*, information about features providing fine detail. The fundamental relationship of NMR microscopy is that the signal,  $S(\mathbf{k})$ , and  $\rho(\mathbf{r})$  are an FT pair:

$$S(\mathbf{k}) = \iiint \rho(\mathbf{r}) \exp[i2\pi \mathbf{k} \cdot \mathbf{r}] d\mathbf{r} \quad (2-8)$$

$$\rho(\mathbf{r}) = \iiint S(\mathbf{k}) \exp[-i2\pi \mathbf{k} \cdot \mathbf{r}] d\mathbf{k} \quad (2-9)$$

Subjecting  $\mathbf{k}$ -space to a multi-dimensional FT converts the data into an image, *i.e.*, a map of signal intensity as a function of frequency, and therefore physical space.

The FIDs acquired from an image slice are mapped onto  $\mathbf{k}$ -space (see Figure 2-7). Herein we will be concerned primarily with two-dimensional Fourier Imaging, FI, where each FID is stored along a single line in  $\mathbf{k}$ -space. For a two-dimensional image there are two axes in  $\mathbf{k}$ -space, typically referred to as the frequency and phase encode axes, and herein denoted  $k_x$  and  $k_y$ , respectively. In a two dimensional Cartesian axis system the FT pair becomes:

$$S(k_x, k_y) = \int_{-\infty}^{\infty} \int_{-\infty}^{\infty} \rho(x, y) \exp[i2\pi(k_x x + k_y y)] dx dy \quad (2-10)$$

$$\rho(x, y) = \int_{-\infty}^{\infty} \int_{-\infty}^{\infty} S(k_x, k_y) \exp[-i2\pi(k_x x + k_y y)] dk_x dk_y \quad (2-11)$$

Slice selection determines the region of a sample which contributes to the observable NMR response and each line along  $k_x$  contains an FID. In the absence of gradients, all protons in a slice precess at identical frequencies (assuming a homogeneous magnetic field and the absence of chemical shift differences), and the signal obtained is at the centre of  $\mathbf{k}$ -space. Each complex point sampled from the FID constitutes a point in  $\mathbf{k}$ -space along  $k_x$ , *i.e.*, if 128 complex points are sampled, the dimension of  $k_x$  is  $N_x = 128$ . Herein, the dimensions or size of the  $\mathbf{k}$ -space matrix is denoted MTX. Thus, each point in  $\mathbf{k}$ -space originates from the NMR signal from the entire slice. The axes of  $\mathbf{k}$ -space do not correspond directly to physical space; however, the number of points along a given axis of  $\mathbf{k}$ -space corresponds to the number of pixels along that axis of the image. As usual, the duration between point acquisition (*i.e.*, the dwell time),  $\Delta t$ , is determined by the sampling BW of the receiver. For example, if the receiver BW is 100 kHz the sampling time between



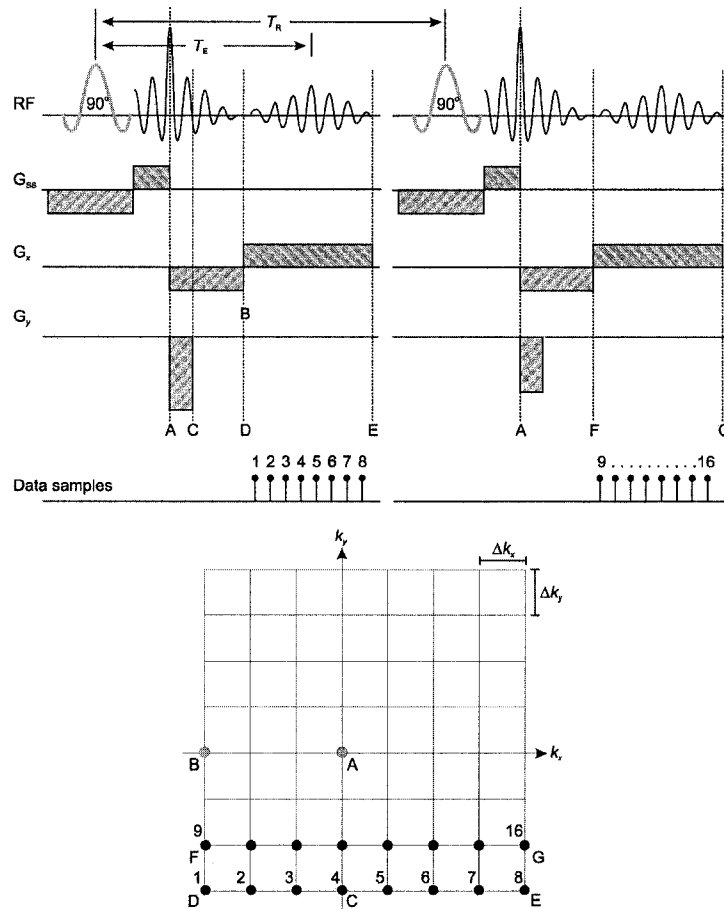


**Figure 2-7.** A sample two-dimensional GE imaging pulse sequence (top) and corresponding k-space representation (bottom). Following slice selective excitation (A) the NMR signal is located at the origin of k-space. The FE gradient,  $G_x$ , is applied (A-B) to traverse along the  $k_x$  axis of k-space to point B. Application of a PE gradient,  $G_y$  (A-C), enables traversing along the  $k_y$  axis of k-space to point C. Applying both  $G_x$  and  $G_y$  traverses k-space from point A to D. Reversal of  $G_x$  (D-E) then results in traversal along  $k_x$  during which the FID is sampled (1-8). The number of points sampled is determined by the dimension of the FE axis,  $N_x$ , and this procedure is repeated as determined by the dimension of the PE axis,  $N_y$ .

complex points is  $10 \mu\text{s}$ , and the acquisition time,  $T_A$ , for a single line along  $k_x$  with  $N_x = 128$  is 1.28 ms.

Applying a magnetic field across the sample imparts a modulation in the precessional frequency of the spins relative to their position in the gradient and therefore the position in the sample. If a gradient is applied along one axis of the imaging plane variations in the signal frequency (or phase) are created along that gradient axis; the spatial location of protons is defined based on their position along

the gradient axis (see Figure 2-3). In practice, the data points are sampled as the FID evolves under the influence of a gradient of fixed strength (Figure 2-7 (D-E)) applied across the sample and the overall NMR response contains spatial information (phase as a function of position). This technique is called frequency encoding, FE. To compensate for the loss of phase coherence due to the field gradient (as mentioned when discussing slice selection in §2.3.1), a dephasing gradient (Figure 2-7(A-B)) is typically applied prior to measuring the NMR signal, and therefore when the signal is measured the phase of the spins is refocused. Following the excitation pulse, successive magnetic field gradients of equal magnitude and opposite sign are applied to create the echo; hence, this technique is referred to as a gradient echo, GE. Thus the distance between points along the FE axis,  $\Delta k_x$  can be described by:

$$\Delta k_x = \frac{\gamma G_x \Delta t}{2\pi} \quad (2-12)$$

The second in-plane axis of the image (and third axis for three dimensional imaging) can be localized by phase encoding, PE, which relates the location of the NMR signals to differences in their phases at readout[30]. Typically, a gradient is applied for a short, fixed time-period,  $t_{PE}$ , perpendicular to the axes of slice selection and FE (Figure 2-7(A-C)). During the brief application of the gradient, the spins precess at different frequencies along the axis of the gradient which introduces a phase shift. After the gradient pulse has ended, all the spins once again precess at the same frequency but the phase shift remains; therefore, the signal acquired during readout contains a phase difference caused by the PE gradient. By incrementing the strength of the gradient the magnitude of the phase change imparted on the FID is modified. Thus the distance between points in along the PE axis,  $\Delta k_y$  can be described by:

$$\Delta k_y = \frac{\gamma \Delta G_y t_{PE}}{2\pi} \quad (2-13)$$

where  $\Delta G_y$  is the change in gradient strength.

#### 2.4. Gradient-Echo and Spin-Echo Experiments

The fundamental pulse sequence required for NMR imaging, the gradient echo, was introduced in §2.3.3 (see Figure 2-7). Often the apparent transverse relaxation time,  $T_2^*$ , is shorter than  $T_2$  due to dephasing of the magnetization caused by inhomogeneous interactions (*e.g.*, chemical shift) or an inhomogeneous magnetic field (Figure 2-8). The GE is adequate for aqueous samples with long  $T_2^*$  relaxation times, for rapid image acquisition, or for introducing  $T_2^*$  contrast. If  $T_2^* \ll T_2$  and results in rapid loss of detectable magnetization, the phase coherence can be recovered by application of an RF refocusing pulse. Although both GE and SE experiments were used for the research presented herein, due to the heterogeneous composition of a PEMFC, most results were obtained with SE experiments. Figure 2-9 shows an example of a SE pulse sequence with a FE gradient and the corresponding Bloch diagrams. In general, the time between signal excitation and echo acquisition,  $T_E$ , is shorter for a GE than a SE experiment, due to the second RF

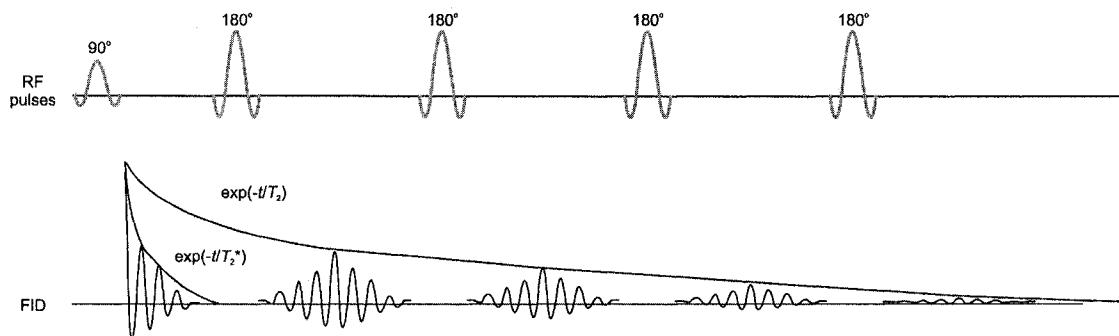


**Figure 2-8.** Comparison of the apparent transverse relaxation,  $\exp(-t/T_2^*)$ , after a  $90^\circ$  RF pulse and the use of a  $180^\circ$  RF pulse to refocus the magnetization dephased by inhomogeneous interactions. A train of  $180^\circ$  pulses, typically called a CPMG sequence, will yield a series of echoes, the envelope of which is representative of the transverse relaxation,  $\exp(-t/T_2)$ .

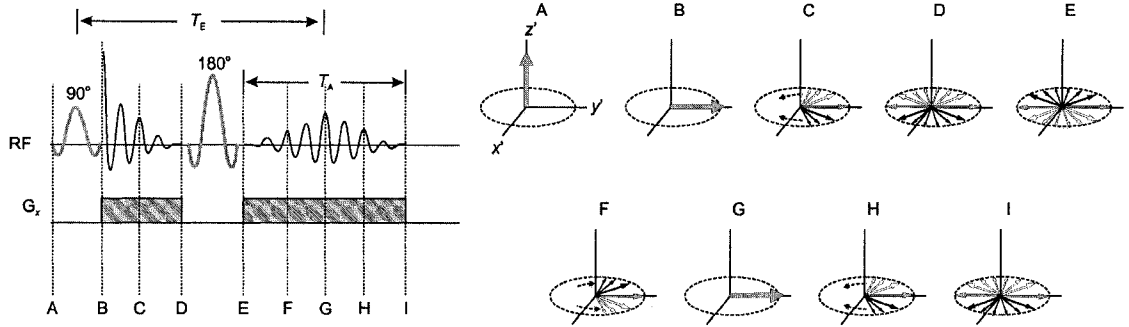


**Figure 2-9.** Representation of a SE sequence showing the effect of a field gradient,  $G_x$ , and  $180^\circ$  RF refocusing pulse on the NMR response after a  $90^\circ$  RF pulse. The time domain of the RF and gradient channels are shown on the left, and the corresponding Bloch diagrams depicting the magnetization are on the right. The RF pulse (A-B) rotates the magnetization into the  $x',y'$  plane. The field gradient (B-D) forces the in-plane magnetization to lose coherence resulting in a decay of the signal. The  $180^\circ$  RF pulse (D-E) flips the transverse magnetization about the  $y'$ -axis to refocus inhomogeneous dephasing (e.g., chemical shift). A field gradient of same sign refocuses the in-plane magnetization (E-G) and the continued presence of the field gradient once again dephases the magnetization (G-I).

pulse used in a SE experiment. A train of RF refocusing pulses will yield a series of SEs, the envelope of which can be described by  $T_2$  (Figure 2-8). This method, referred to as the CPMG experiment, after Carr and Purcell[31], and Meiboom and Gill[32], is often used to measure  $T_2$ .

## 2.5. Resolution and S/N

The image pixel size is determined by the number of points in  $k$ -space and the physical dimensions of the region to be imaged, typically called the field-of-view, FOV. The pixel size for the FE dimension can be described by:

$$\Delta x = \frac{\text{FOV}_x}{N_x} \quad (2-14)$$

where  $N_x$  is the number of points acquired. Many images presented herein were obtained with a  $30 \text{ mm} \times 30 \text{ mm}$  FOV and a  $128 \times 128$  point  $k$ -space (i.e.,  $\text{MTX} = 128^2$ ), which results in an image pixel size of  $234 \mu\text{m} \times 234 \mu\text{m}$ . For experiments using FE, the achievable spatial resolution,  $1/\Delta x$ , as described by Equation (2-15), is limited by the spread in observed frequencies or linewidth at half-height of the

NMR peak,  $\nu_{1/2}$ , and the strength of the applied gradient,  $G_x$ [7]:

$$\frac{1}{|\Delta x|} = \left| \frac{\gamma G_x}{2\pi \nu_{1/2}} \right| \quad (2-15)$$

In practice, the maximum strength of the applied gradient is limited (*e.g.*, the maximum commercially available gradients for NMR microscopy are approaching 3 T m<sup>-1</sup> (Bruker Micro-5)). The linewidth is related to the time required for the NMR signal to decay; as a result of inhomogeneities in the magnetic field experienced the linewidth is related to the shorter apparent spin-spin relaxation time,  $T_2^*$ , such that  $\nu_{1/2} = (\pi T_2^*)^{-1}$ . In addition, if the total signal readout is long compared to the  $T_2^*$  of the signal, the ends of the FE axes in  $k$ -space contain mostly noise which also results in image blurring.

Each pixel in a two-dimensional image slice is a projection of the signal contained within the volume defined by the width of the pixel and the slice thickness. This three-dimensional volume element is called a voxel. Larger slice thicknesses and larger pixel sizes increase the signal to noise ratio,  $S/N$ ; however, fine detail may be obscured by averaging of the signal within a voxel. Typically to increase the  $S/N$  of an NMR experiment one can either average the signal ( $S/N \propto [\text{number FIDs acquired}]^{1/2}$ ) or use a stronger applied magnetic field (ideally,  $S/N \propto B_0^{7/4}$ , however, in practice  $S/N \propto B_0$ )[33]. With the availability of commercial wide-bore superconducting magnets with applied fields greater than 15 T, the use of higher fields to increase  $S/N$  is common; however, higher applied magnetic fields require the use of stronger gradients and higher frequency excitation pulses. The  $S/N$  is also related to the filling factor of the RF probe with respect to the volume from which signal is acquired[2]:

$$S/N \propto \frac{V_{\text{voxel}}}{V_{\text{probe}}} \quad (2-16)$$

where  $V_{\text{voxel}}$  and  $V_{\text{probe}}$  are the volumes of the voxel and RF coil, respectively. For this research, birdcage resonators of 10 mm and 30 mm diameter were used. Assuming that the height equals the diameter of the coil and the same  $V_{\text{voxel}}$ , using the smaller coil would increase the S/N by a factor of ~25.

## 2.6. Contrast

NMR microscopy is a robust technique with vast application in medical and materials science due to the multitude of molecular based image contrast mechanisms that can be invoked. For example, image contrast can be related to relaxation of the nuclei, molecular motion (*e.g.*, diffusion, flow), chemical shift variations, magnetic susceptibility variations, and relaxation of the nuclei[1-3,10]. The potential of using relaxation as a basis for image contrast was reported in 1971 by Damadian[34], who noted that the  $^1\text{H}$  NMR signals from healthy and cancerous tissues exhibited different NMR relaxation times. Although this dependence is exploited daily in MRI, the fundamental concepts to attain spatial localization using NMR were not developed by Damadian and he was passed over for the 2003 Nobel Prize in Medicine or Physiology awarded to Lauterbur and Mansfield for their discoveries concerning MRI.

## 2.7. Image Artefacts

The highest frequency that can be sampled unambiguously is one-half of the receiver BW; this is the Nyquist frequency. If the object is beyond the FOV of the acquired image, signal from outside the region may fold into the opposite side of the image. In the FE direction, signals with frequencies outside the desired range are eliminated with a digital filter; however, the FOV in the PE direction must encompass the entire sample. For PE, the magnetic field gradient is applied for a short, fixed time-period and the phase evolution of all spins due to field heterogeneity is constant except for the phase-shift introduced by the gradient.

However, sample motion introduces a phase shift term which causes frequency components to be misregistered resulting in a ghosting artefact.

There are several effects that different receiver BWs can impart. A larger BW facilitates faster data acquisition (*i.e.*, reduced dwell time), reduced artefacts due to chemical shift differences, magnetic field inhomogeneities, and motion, but also results in lower S/N. Assuming a constant FOV, a larger BW requires stronger FE gradients due to the decreased time between sampled points. A smaller BW increases the time required to sample each echo, which significantly increases the echo time,  $T_E$ , and may introduce unwanted  $T_2$  or  $T_2^*$  contrast. As well, if the readout is long compared to  $T_2^*$  the images may be degraded by blurring. At a given field strength, the difference in frequencies between protons with different chemical shifts is constant. With a smaller BW, weaker FE gradients are used and the frequency difference between pixels is reduced; therefore a difference in frequency due to chemical shift causes a shift over more pixels when the sampling BW is reduced. In practice, the signal strength is proportional to field strength, whereas the S/N increases only as the square root of BW reduction; therefore, one may effectively compensate for the increase in severity of chemical shift artefacts or motion at higher fields with an increased BW and still provide greater signal overall.

Interference from RF noise can result in stripes in images called zipper artefacts[6]. Such artefacts commonly occur along the PE axis at the point of zero frequency but extraneous RF noise may also result in artefacts elsewhere. Truncation artefacts are caused by incomplete sampling of the wave forms and upon Fourier transformation, edge or Gibbs ringing can result in alternating light and dark bands[4]. Magnetic susceptibility differences can result in image distortion from incorrect FE[7], and at higher applied fields the frequency shift introduced becomes larger. Such artefacts can often be reduced by using a SE technique with a

short  $T_E$ ; however, if the field distortions become very large (or the sampling BW small) susceptibility inhomogeneities can result in complete loss of signal. Understanding the origin of artefacts introduced into NMR images by conductors and susceptibility differences is of interest for both materials and medical imaging[35,36]. For example, magnetic susceptibility differences due to blood oxygen levels are responsible for the contrast observed in functional MRI[36].

## 2.8. Summary

This chapter introduced the concepts of NMR microscopy as applied in this Thesis. The fundamental Zeeman interaction results in an energy splitting between nuclear spin states in the presence of an external applied magnetic field,  $B_0$ , and the frequency corresponding to this difference in energy is the Larmor frequency,  $\nu_L$ . The Larmor frequency is proportional to both the magnetogyric ratio,  $\gamma$ , and to  $B_0$ . By introducing linear field gradients that either add to, or subtract from,  $B_0$ , the time-dependent NMR signal can be related to position in space *via* a Fourier transform. The attainable resolution of the resulting image is related to the relaxation time of the NMR signal, and effects such as diffusion, magnetic susceptibility variations, and RF interference may introduce artefacts into the image.

## 2.9. References

- [1] Callaghan, P. T. *Principles of Nuclear Magnetic Resonance Microscopy*; Oxford University Press: New York, 1991.
- [2] Kimmich, R. *NMR: Tomography, Diffusometry, Relaxometry*; Springer-Verlag: Berlin, 1997.
- [3] Haacke, E. M.; Brown, R. W.; Thompson, M. R.; Venkatesan, R. *Magnetic Resonance Imaging: Physical Principles and Sequence Design*; John Wiley and Sons: New York, 1999.
- [4] Liang, Z. P.; Lauterbur, P. C. *Principles of Magnetic Resonance Imaging: A Signal Processing Perspective*; IEEE Press: New York, 2000.



- [5] McRobbie, D. W.; Moore, E. A.; Graves, M. J.; Prince, M. R. *MRI: From Picture to Proton*; Cambridge University Press: Cambridge, 2003.
- [6] Mitchell, D. G.; Cohen, M. S. *MRI Principles*; Second ed.; Saunders: Philadelphia, 2004.
- [7] Blümich, B. *NMR imaging of materials*; Oxford University Press: New York, 2000.
- [8] Zeeman, P. *Nature* **1897**, *55*, 347.
- [9] Harris, R. K.; Becker, E. D.; De Menezes, S. M. C.; Goodfellow, R.; Granger, P. *Pure Appl. Chem.* **2001**, *73*, 1795-1818.
- [10] Xia, Y. *Concepts Magn. Reson.* **1996**, *8*, 205-225.
- [11] Ernst, R. R. *Angew. Chem.* **1992**, *104*, 817-836.
- [12] Cory, D. G. In *Annual Reports on NMR Spectroscopy*; Webb, G. A., Ed.; Academic Press Inc.: London, 1992; Vol. 24, 87-180.
- [13] Lauterbur, P. C. *Angew. Chem. Int. Ed.* **2005**, *44*, 1004-1011.
- [14] Mansfield, P. *Angew. Chem. Int. Ed.* **2004**, *43*, 5456-5464.
- [15] Hayes, C. E.; Edelstein, W. A.; Schenck, J. F.; Mueller, O. M.; Eash, M. J. *Magn. Reson.* **1985**, *63*, 622-628.
- [16] Roffmann, W. U.; Crozier, S.; Luescher, K.; Doddrell, D. M. *J. Magn. Reson. B* **1996**, *111*, 174-177.
- [17] Forbes, L. K.; Crozier, S.; Doddrell, D. M. *SIAM J. Appl. Math.* **1997**, *57*, 401-425.
- [18] Crozier, S.; Luescher, K.; Forbes, L. K.; Doddrell, D. M. *J. Magn. Reson. B* **1995**, *109*, 1-11.
- [19] Mansfield, P.; Chapman, B. *J. Magn. Reson.* **1986**, *66*, 573-576.
- [20] Tanner, J. E. *Rev. Sci. Instrum.* **1965**, *36*, 1086-1087.
- [21] Hoult, D. I.; Richards, R. E. *Proc. R. Soc. London, Ser. A* **1975**, *344*, 311-340.

- [22] Moore, W. S.; Holland, G. N. *Philos. T. Roy. Soc. B* **1980**, 289, 511-518.
- [23] Garroway, A. N.; Grannell, P. K.; Mansfield, P. J. *Phys. C Solid State* **1974**, 7, L457-L462.
- [24] Bloch, F. *Phys. Rev.* **1946**, 70, 460-474.
- [25] Bloembergen, N.; Purcell, E. M.; Pound, R. V. *Phys. Rev.* **1948**, 73, 679-712.
- [26] Stejskal, E. O.; Tanner, J. E. *J. Chem. Phys.* **1965**, 42, 288-292.
- [27] Mansfield, P.; Grannell, P. K. *J. Phys. C Solid State* **1973**, 6, L422-L426.
- [28] Mansfield, P.; Grannell, P. K. *Phys. Rev. B: Condens. Matter* **1975**, 12, 3618-3634.
- [29] Mansfield, P. *Contemp. Phys.* **1976**, 17, 553-576.
- [30] Edelstein, W. A.; Hutchison, J. M.; Johnson, G.; Redpath, T. *Phys. Med. Biol.* **1980**, 25, 751-756.
- [31] Carr, H. Y.; Purcell, E. M. *Phys. Rev.* **1954**, 94, 630-638.
- [32] Meiboom, S.; Gill, D. *Rev. Sci. Instrum.* **1958**, 29, 688-691.
- [33] Hoult, D. I.; Richards, R. E. *J. Magn. Reson.* **1976**, 24, 71-85.
- [34] Damadian, R. *Science* **1971**, 171, 1151-1153.
- [35] Lauer, U. A.; Graf, H.; Berger, A.; Claussen, C. D.; Schick, F. *Magn. Reson. Imaging* **2005**, 23, 563-569.
- [36] Ogawa, S.; Lee, T. M.; Nayak, A. S.; Glynn, P. *Magnet. Reson. Med.* **1990**, 14, 68-78.

### Chapter 3. Background and Theory: PEMFCs

This chapter serves to introduce the fundamental components and theory of PEMFCs as related to the research presented in this Thesis. An overview of proton transport properties in Nafion is also provided, followed by a brief review of typical PEMFC diagnostic techniques. Several monographs on fuel cells have been useful for outlining the fundamental concepts and recent state of PEMFCs[3-5], in particular the text edited by Hoogers[4] contains an abundance of primary references.

#### 3.1. PEMFC Components and Reactions

The main components of a typical PEMFC are the PEM, catalysts/electrode, gas diffusion layer, gas flow channels, and the current collector plate (Figure 3-1)[3]. The fundamental requirements of a suitable PEM are to: exhibit high proton conductivity, be impermeable to reactants (*e.g.*,  $H_2(g)$ ,  $O_2(g)$ ,  $MeOH(aq)$ ), and be chemically and mechanically stable in a PEMFC environment. The industry standard for PEMs is Nafion, introduced by DuPont in 1972[7,8], although similar products have been developed (*e.g.*, Flemion, Aciplex). These PEMs are made from a perfluorocarbon-sulfonic acid ionomer, which is a copolymer of tetrafluoroethylene (TFE,  $C_2F_4$ ) and perfluorosulfonate monomers. As shown in a

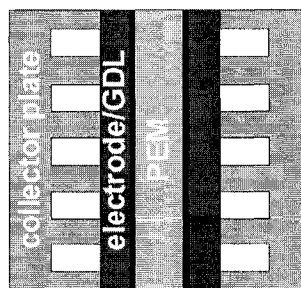


**Figure 3-1.** Schematic of the components of a typical PEMFC. The catalyst is between the PEM and electrode/GDL. The spaces in the collector plate represent the flow channels.

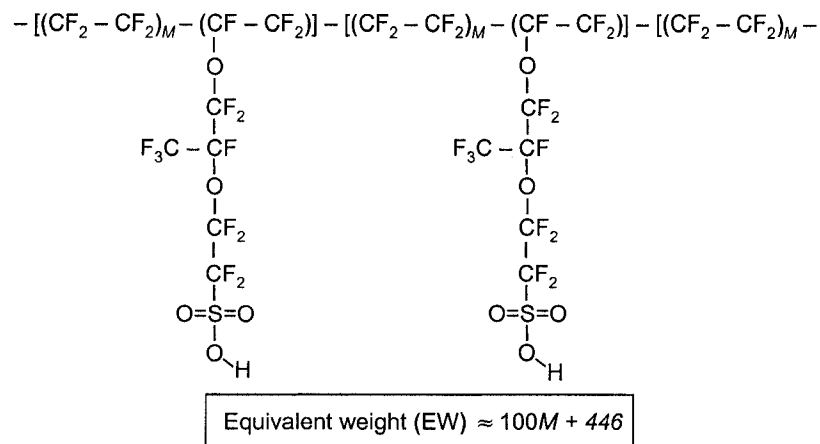


**Figure 3-2.** Representation of the chemical composition of Nafion. The backbone is composed of tetrafluoroethylene and perfluorosulfonate monomers which form the pendulum-like side chains. Water molecules associate with the SO<sub>3</sub>H groups, and for Nafion-117 the H<sub>2</sub>O/SO<sub>3</sub>H ratio,  $\lambda$ , ranges from ~2 to 22[2,6].

representation of the structure of Nafion in Figure 3-2, the hydrophobic TFE components form a backbone along which sulfonate terminated side chains are distributed. The sulfonic acid head group, composed of an SO<sub>3</sub>H moiety, is hydrophilic and facilitates the absorption of water. The exact morphology of Nafion at various levels of hydration is unclear. At low levels of hydration water exists in isolated domains, and as the amount of water increases percolation pathways are formed which creates an extended phase of water. A recent review by Mauritz and Moore[10] is an excellent source of primary references to research on Nafion.

Nafion membranes are typically referred to by a characteristic three-digit number; the first two digits indicate the equivalent weight, EW, of the polymer, and the last digit the thickness of the membrane. For example, in this research Nafion-117 is used, which has an equivalent weight, EW  $\approx 1100$  g eq<sup>-1</sup> and a thickness of 7 mils (*i.e.*, 0.007 inches or 178  $\mu$ m). Equivalent weight is the measure of the ionic concentration (*i.e.*, H<sup>+</sup>) within the ionomer. The length of the polymer backbone between adjacent side chains can be related approximately to the EW by the relation

EW  $\approx$  100M + 446, where M is the number of TFE groups between the side chains. Typically, Nafion membranes with EW  $\approx$  1100 are used for PEMFC applications and are available in a range of thickness from 50 (Nafion-112) to 254  $\mu$ m (Nafion-1110). The thinner PEMs are generally used for hydrogen PEMFCs in an attempt to maintain a uniform distribution of water in the PEM, and thicker membranes are used for direct-methanol fuel cells to slow the diffusion of methanol from the anode to the cathode. For acid-form Nafion-117, the number of water molecules per sulfonic acid head group,  $\lambda$ , ranges from a low of  $\sim$ 2 to 14 depending on relative humidity, and when in contact with H<sub>2</sub>O(l),  $\lambda \approx$  22 [2,6]. The water content of Nafion is often reported as a wt% relative to the dry membrane where 1.66 wt% corresponds to approximately one H<sub>2</sub>O molecule per SO<sub>3</sub>H moiety (*i.e.*,  $\lambda = 1$ ).

### 3.1.1. Proton Transport in Nafion

The protonic conductivity,  $\sigma$ , of Nafion-117 ranges from  $\sim$ 0.4 to 10 S m<sup>-1</sup> as  $\lambda$  increases from  $\sim$ 2.5 to 22 (see Table 3-1)[2,6]. For comparison, the electrical conductivity of Ag is  $63.0 \times 10^8$  S m<sup>-1</sup> and of sea water is 5 S m<sup>-1</sup>. Proton transport in Nafion may occur *via* a combination of mechanisms[11,12] including translational self-diffusion, Fickian diffusion[13], Grotthuss-type transport[14], and electro-

**Table 3-1.** Protonic conductivity of acid-form Nafion-117 as a function of water content at 30 °C.<sup>a</sup>

$n\text{H}_2\text{O}/\text{SO}_3\text{H}$	conductivity (S m <sup>-1</sup> )
2.5	0.4
3.0	1.0
4.9	1.7
5.7	3.5
6.2	3.0
9.0	4.2
10.0	4.8
13.3	6.2
21.9	10.0

a) The values were obtained graphically from Figure 7 in Ref.[2].

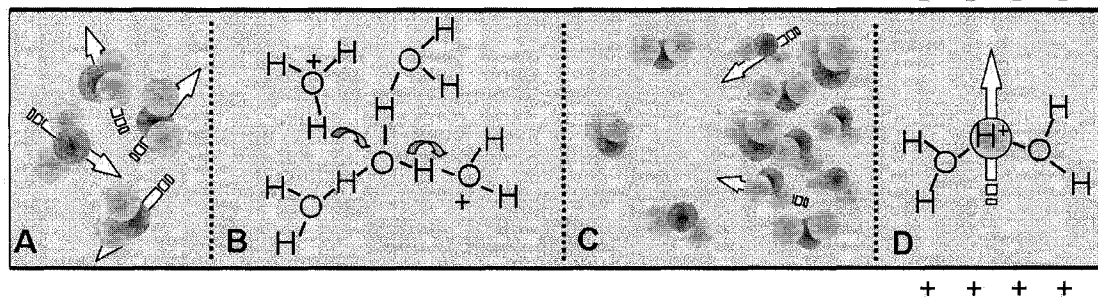


**Figure 3-3.** Proton transport in Nafion occurs *via* numerous mechanisms: (A) translational diffusion due to Brownian motion, (B) Grotthuss hopping, (C) Fickian or concentration gradient driven diffusion, and (D) electro-osmotic drag where water associated with protons is dragged through the PEM from anode to cathode in the presence of an electric field.

osmotic transport introduced by the electric field from anode to cathode[15] (see Figure 3-3).

Translational self-diffusion is the displacement of molecules due to Brownian motion in a system of uniform chemical composition [16]. For random motion, the displacement of the molecules diffusing at rate  $D$  typically follows a Gaussian distribution function, such that the root mean square displacement,  $\langle r^2 \rangle^{1/2}$ , in a time,  $t$ , is approximately  $(6Dt)^{1/2}$  [17].

Diffusion that occurs in the presence of a concentration gradient was recognized in 1855 by Fick[13] who adopted the mathematical equation of heat conduction derived previously by Fourier. For an isotropic medium, the rate of transfer of the diffusing substance through a unit area is proportional to the concentration gradient, and is described by Fick's first law:

$$J_i = -D \frac{\partial C}{\partial i} \quad (3-1)$$

where  $J_i$  is the rate of transfer per unit area or flux,  $C$  is the concentration of the diffusing substance,  $i$  is the space coordinate measured normal to the area, and  $D$  is the diffusion constant.

The transport of protons in water *via* an incoherent hopping mechanism was first postulated in 1806 by von Grotthuss[18]. Although the exact molecular

mechanism of Grotthuss transport remains unclear, the rate-limiting step is thought to involve cleavage of a hydrogen bond and a periodic series of isomerisations between  $\text{H}_9\text{O}_4^+$  and  $\text{H}_5\text{O}_2^+$ [14].

Electro-osmosis is an electrokinetic phenomenon in which the flow of liquid tangential to a stationary interface is caused by an applied electric field[19]. The first mathematical theory was provided by Helmholtz[20], and for a given liquid in contact with a certain solid, the rate of liquid transport is determined solely by the current[21].

The water content, translational self-diffusion rate, electro-osmotic drag coefficient, and ionic conductivity of Nafion-117 are known to be higher when the PEM is in contact with  $\text{H}_2\text{O}(l)$  versus water vapour[2,22,23]. As discussed in §2.3.2, by applying strong magnetic field gradients, the variation in the local magnetic field experienced by an ensemble of spins can be controlled and the subsequent attenuation of the detected NMR signal can be described as a function of motion[24,25]. A summary of  $^1\text{H}$  translational diffusion constants,  $D$ , for water in acid-form Nafion-117 as determined by  $^1\text{H}$  NMR spectroscopy is provided in Table

**Table 3-2.** Summary of  $^1\text{H}$  translational diffusion rates for pure  $\text{H}_2\text{O}(l)$  and  $\text{H}_2\text{O}$  in acid-form Nafion-117, as determined by NMR techniques at atmospheric pressure.

	Method <sup>a</sup>	T [K]	Condition <sup>b</sup>	$D$ [ $10^{-10} \text{ m}^2 \text{ s}^{-1}$ ]	Reference
$\text{H}_2\text{O}(l)$	SGSE	298		$23.0 \pm 0.2$	[1]
Nafion-117	PGSE	303	3.3 wt%	$0.60 \pm 0.06$	[2,6]
	PGSE	303	5.0 wt%	$1.20 \pm 0.08$	[2,6]
	SGSE	288	6.6 wt%	0.83	[9]
	PGSE	303	6.6 wt%	$2.10 \pm 0.06$	[2,6]
	PGSE	303	10.0 wt%	$3.70 \pm 0.15$	[2,6]
	PGSE	303	15.0 wt%	$4.40 \pm 0.07$	[2,6]
	SGSE	288	22.0 wt%	5.56	[9]
	PGSE	303	23.2 wt%	$5.80 \pm 0.21$	[2,6]
	PGSE	303	36.5 wt%	7.38	[2] <sup>c</sup>

a) SG = static gradient, PG = pulsed gradient, SE = spin echo

b)  $1.66 \text{ wt} \% \approx \lambda = 1$ , where  $\lambda = n\text{H}_2\text{O}/\text{SO}_3\text{H}$

c) Measured graphically from Figure 5 in Ref. [2].

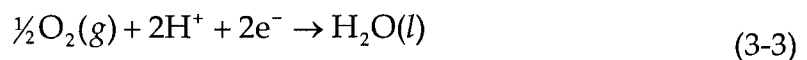
3-2. For Nafion with a high level of hydration, proton transport by Grotthuss hopping is expected to be significant because the rate of proton transport across the membrane is higher than the rate of water diffusion[6]; however, as Nafion becomes dehydrated the rate of proton conductivity and bulk diffusion coalesce[6]. The diffusion coefficient for H<sub>2</sub>O in maximally hydrated Nafion-117 (~36 wt%, λ = 22) at 298 K is ~7.4 × 10<sup>-10</sup> m<sup>2</sup> s<sup>-1</sup>[2,6]. In an operating PEMFC approximately one to three water molecules per H<sup>+</sup> are co-transported from the anode to cathode through the electric field *via* electro-osmotic drag, which diminishes with decreasing PEM water content[2,15,26]. Often a water concentration gradient is established across the PEM from anode to cathode due to electro-osmotic drag and the production of water at the cathode. Non-uniform distribution of water in the PEM results in Fickian diffusion from the cathode to the anode, which is called back-diffusion.

### 3.1.2. Catalysts and Reactions

The region where the catalysts reside between the PEM and the gas diffusion layer is considered the electrode. The electrochemical reactions take place at the interface of the catalyst, PEM, and gas diffusion layer – the so called three-phase boundary. For hydrogen fuel cells platinum is the most common catalyst for both oxidation of hydrogen at the anode and reduction of oxygen at the cathode[27]. H<sub>2</sub>(g) is oxidized at the anode over the nanoparticle electrocatalyst to produce protons and electrons:



The protons are transferred to the cathode through the PEM while the electrons pass through the external circuit. At the cathode, the protons and electrons reduce oxygen over the electrocatalyst to produce water:





The total reaction, with the resulting molar Gibbs' free energy,  $\Delta G_f^\circ$ , is:



Therefore, the theoretical maximum electrical potential for a PEMFC fuelled with hydrogen and producing  $\text{H}_2\text{O}(\text{l})$  is:

$$\frac{\Delta G_f^\circ}{2F} = 1.2299 \text{ V} \quad (3-5)$$

where  $F$  is the Faraday constant,  $96\,485 \text{ C mol}^{-1}$ .

Within the last decade the use of supported catalyst structures and improvements in preparative techniques have reduced the amount of platinum used by three orders of magnitude to  $< 0.5 \text{ mg cm}^{-2}$ [5,27]. For example, to increase the three-phase boundary, the catalyst is often prepared with a solution of the PEM. Unfortunately, platinum has an Achilles heel – poisoning. Besides being a clean alternative energy source, hydrogen PEMFCs are often promoted as a way to reduce our reliance on limited fossil fuel resources. In reality, most commercial  $\text{H}_2(\text{g})$  is obtained by steam reforming natural gas, and the reformat gas may contain CO, unconverted fuel, other hydrocarbons, and by-products such as hydrogen sulphide and ammonia[3,4,28]. Platinum has a higher affinity toward CO than toward  $\text{H}_2$  and as a result the catalyst sites can become occupied with CO[29], even at concentrations as low as 100 ppm. Pt-Ru catalysts have a higher tolerance to CO[30], and show a marked improvement in cell performance relative to Pt. Ru is thought to aid with the electrooxidation of CO on neighbouring Pt atoms[31], or weaken the Pt-CO bond strength[29].

A gas diffusion layer, GDL, typically a partially wet-proofed carbon-fibre material, in either paper form or woven into a cloth, is pressed between the catalyst surface and the current collector plates. The current collector plates are typically electrically and thermally conductive, and impermeable to gases. They are often

machined from a graphite based material such as a thermoplastic composite or metallic materials coated with *e.g.*, graphite, noble metals, metal nitrides, *etc.*, to prevent corrosion.

### 3.2. Water and PEMFCs

Water is present in the PEM, GDLs, catalysts, and flow fields of an operating PEMFC[32]. The performance and longevity of an operating PEMFC is related to the amount of water present in the different components of the cell[33]. For example, catalyst sites can be blocked by water that has pooled on the surface of the electrodes; subsequently, the catalyst is deprived of hydrogen or oxygen which reduces the performance of the cell and in the long-term can cause degradation of materials[33]. Related to electrode flooding is the behaviour of water within the GDLs. The GDLs serve a multitude of functions: to make contact between the electrode surface and the external electrical circuit that collects power from the fuel cell; to provide a pathway for the reactant gases or water to the catalyst layers; to transport excess product water from the cathode to the flow channels; and to prevent the PEM from sagging into the flow channels[27]. The rates that gases and water diffuse through the GDLs strongly affect the performance of the fuel cell, and the diffusion is impeded or blocked by water accumulated within them. Excessive water build-up also blocks the channels through which the  $H_2(g)$  and  $O_2(g)$  flow, thereby reducing the overall efficiency of the fuel cell. When fuel cells are bundled to operate together in stacks, water accumulation causes differences in cell-to-cell performance and variation in the pressure drops across the individual cells[34,35]. In addition, the amount of water present at the three-phase boundary between the PEM, carbon sheet, and gas flow channels at the catalyst sites must also be optimized[36]. Finally, anode catalysts that operate on impure hydrogen, typically containing CO, require water to oxidize the impurities[28].

### 3.3. Fuel Cell Diagnostic Techniques

Traditional fuel cell diagnostic methods provide critical information regarding global performance characteristics through numerical fitting of experimental polarization curves, and using techniques such as current interrupt and AC impedance spectroscopy[37]. These techniques do not, however, provide information regarding local water content or distribution. An important method by which insight into the amount and distribution of water in operating PEMFCs is obtained is through theoretical modeling. Many theoretical models to describe the thermo- and electrochemical operation of PEMFCs have been developed to reproduce and predict experimental outcomes in an effort to engineer more efficient and reliable PEMFCs. An introduction to PEMFC modeling and representative examples can be found in a text by Barbir[3] and a more thorough summary in recent reviews[38-41]. Theoretical models are validated and improved with experimental data, and thus the capability of models is often impeded by a lack of detailed experimental information regarding what happens *inside* an operating PEMFC. To thoroughly understand, model, and optimize a PEMFC the distribution of water within the cell must be known.

During the past decade numerous experimental techniques were developed to measure or observe *in situ* various phenomena within an operating PEMFC. These methods include electron paramagnetic resonance investigations of PEM degradation[42,43], the construction of PEMFCs using transparent materials[44-54], and the use of neutron imaging[55-63]. For example, numerous studies have used transparent PEMFCs to investigate the formation of  $\text{CO}_2(\text{g})$  in the anode flow field of direct methanol fuel cells[44], and the behaviour of water in gas diffusion layers[50]. Neutron imaging techniques are inherently sensitive to observing protons whilst insensitive to many materials typically used for constructing fuel cells (*e.g.*, Al,

graphite)[61], and have been applied to measure the total distribution of water. Also, Schneider *et al.*[59] have developed a method to simultaneously perform neutron imaging and locally resolved impedance spectroscopy. Both neutron imaging and now,  $^1\text{H}$  NMR microscopy (*vide infra*)[64-70], have enabled the visualization of areas within an operating PEMFC not observable by direct optical methods.

In parallel with our research, several other groups have also been investigating the application of  $^1\text{H}$  NMR microscopy to operating PEMFCs. This research is briefly summarized. Teranishi *et al.* commenced investigations using  $^1\text{H}$  NMR microscopy to measure water distribution across the PEM from anode to cathode during fuel cell operation[68]. The majority of their studies have focused on the Aciplex S-1112 PEM with a thickness of 340  $\mu\text{m}$ [68,70,71], although the use of Aciplex S-1104 and S-1102 PEMs (thickness 178 and 56  $\mu\text{m}$ , respectively)[69,72], Nafion-117, and Flemion PEMs has been reported[73]. The membrane electrode assemblies used for these investigations appear to be constructed with the PEM sandwiched by gas diffusion electrodes upon which platinum is dispersed[73,74]. Using a SE imaging experiment to obtain signal from a large 50  $\mu\text{m}$   $\times$  800  $\mu\text{m}$   $\times$  2.5 mm voxel, changes in water content in the S-1112 PEM during fuel cell start-up were monitored with a temporal resolution of 50 s[74]. A drop in cell voltage was correlated with an overall decline of water in the PEM during the first 200 s of operating with a small circuit resistance, and the anode side of the PEM dehydrated more rapidly than the cathode[74]. Their reports demonstrate that the overall water content in the PEM decreases with increasing current[68-70,73,74]. Also, this group previously observed that under certain circumstances a direct supply of water to the PEM of an operating PEMFC improved performance[75]. In recent conference proceedings[67], they reported the use of  $^1\text{H}$  NMR microscopy to determine water

distribution in the S-1112 PEM, with and without direct water supply. Using an in-plane resolution of  $800 \times 25 \mu\text{m}$  with a slice thickness of 5 mm, the region of the PEM in contact with  $\text{H}_2\text{O}(l)$  was found to be swollen relative to other areas of the PEM. Teranishi *et al.* have also used the results from their  $^1\text{H}$  NMR microscopy experiments[69] to parameterize a one-dimensional model for water transport in a PEM[70,71]. Recently, Minard *et al.*[76] reported preliminary results from  $^1\text{H}$  NMR microscopy experiments used to investigate the distribution of water in the plane (*i.e.*, from gas inlet to outlet) in a operating fuel cell.

The research presented in this Thesis provides, for the first time, images of the in-plane distribution of water in the PEM between the operating catalyst layers and of  $\text{H}_2\text{O}(l)$  in the cathode flow channels, and investigates their interdependence on fuel cell operating conditions.

#### 3.4. Summary

In this chapter, the components of a typical PEMFC were introduced. The structure and properties of Nafion, and the mechanisms of proton transport within the PEM were discussed. The fundamental reactions for hydrogen fuelled PEMFCs, which occur over electrocatalysts, were shown to provide a source of electrical current and a theoretical maximum potential for a single cell. The impact of water content on the conductive properties of Nafion, and the potential effects of  $\text{H}_2\text{O}(l)$  accumulation in the components of a PEMFC were emphasized. The inability of traditional PEMFC diagnostic techniques to measure the distribution and content of water within the cell, and the necessity of this information to achieve robust, stable, and high-performance PEMFCs has lead to the development of techniques to study *in-situ* the distribution of water in operating PEMFCs.

### 3.5. References

- [1] Harris, K. R.; Woolf, L. A. *J. Chem. Soc., Faraday Trans.* **1980**, *76*, 377-385.
- [2] Zawodzinski, T. A., Jr.; Derouin, C.; Radzinski, S.; Sherman, R. J.; Smith, V. T.; Springer, T. E.; Gottesfeld, S. J. *Electrochem. Soc.* **1993**, *140*, 1041-1047.
- [3] Barbir, F. *PEM Fuel Cells: Theory and Practice*; Elsevier Academic Press: San Diego, 2005.
- [4] Hoogers, G., Ed. *Fuel Cell Technology Handbook*; CRC Press LLC: Boca Raton, 2003.
- [5] Larminie, J.; Dicks, A. In *Fuel Cell Systems Explained*; 2nd ed.; John Wiley and Sons Ltd.: Chichester, 2003, 75-90.
- [6] Zawodzinski, T. A., Jr.; Neeman, M.; Sillerud, L. O.; Gottesfeld, S. J. *Phys. Chem.* **1991**, *95*, 6040-6044.
- [7] Grot, W. *Chem. Ing. Tech.* **1972**, *44*, 167-169.
- [8] Grot, W. *Chem. Ing. Tech.* **1975**, *47*, 617-617.
- [9] Jayakody, J. R. P.; Stallworth, P. E.; Mananga, E. S.; Farrington-Zapata, J.; Greenbaum, S. G. *J. Phys. Chem. B* **2004**, *108*, 4260-4262.
- [10] Mauritz, K. A.; Moore, R. B. *Chem. Rev.* **2004**, *104*, 4535-4585.
- [11] Paddison, S. J. *Annu. Rev. Mater. Res.* **2003**, *33*, 289-319.
- [12] Kreuer, K.-D.; Paddison, S. J.; Spohr, E.; Schuster, M. *Chem. Rev.* **2004**, *104*, 4637-4678.
- [13] Fick, A. *Ann. Phys. Lpz.* **1855**, *170*, 59.
- [14] Agmon, N. *Chem. Phys. Lett.* **1995**, *244*, 456-462.
- [15] Ise, M.; Kreuer, K. D.; Maier, J. *Solid State Ionics* **1999**, *125*, 213-223.
- [16] Crank, J. *The Mathematics of Diffusion*; Clarendon Press: Oxford, 1956.

- [17] Berne, B. J.; Pecora, R. In *Dynamic Light Scattering With Applications to Chemistry, Biology, and Physics*; John Wiley and Sons, Inc.: New York, 1976, 83-86.
- [18] von Grotthuss, C. J. T. *Ann. Chim.* **1806**, *58*, 54-73.
- [19] Kraemer, E. O.; Willams, J. W.; Alberty, R. A. In *A Treatise on Physical Chemistry*; 3rd ed.; Taylor, H. S., Glasstone, S., Eds.; D. Van Nostrand Company, Inc.: New York, 1951; Vol. 2, 628-632.
- [20] von Helmholtz, H. L. F. *Ann. Physik* **1879**, *7*, 337.
- [21] Perrin, F. J. *Chim. Phys.* **1904**, *2*, 607.
- [22] Siu, A.; Schmeisser, J.; Holdcroft, S. J. *Phys. Chem. B* **2006**, *110*, 6072-6080.
- [23] Zawodzinski, T. A., Jr.; Springer, T. E.; Davey, J.; Jestel, R.; Lopez, C.; Valerio, J.; Gottesfeld, S. J. *Electrochem. Soc.* **1993**, *140*, 1981-1985.
- [24] Callaghan, P. T. *Principles of Nuclear Magnetic Resonance Microscopy*; Oxford University Press: New York, 1991.
- [25] Kimmich, R. *NMR: Tomography, Diffusometry, Relaxometry*; Springer-Verlag: Berlin, 1997.
- [26] Fuller, T. F.; Newman, J. J. *Electrochem. Soc.* **1992**, *139*, 1332-1337.
- [27] Barbir, F. In *PEM Fuel Cells: Theory and Practice*; 73-113, Ed.; Elsevier Academic Press: San Diego, 2005, 115-145.
- [28] Larminie, J.; Dicks, A. *Fuel Cell Systems Explained*; 2nd ed.; John Wiley and Sons Ltd.: Chichester, 2003.
- [29] Ralph, T. R.; Hogarth, M. P. *Platinum Metals Rev.* **2002**, *46*, 117-135.
- [30] Gottesfeld, S.; Zawodzinski, T. A., Eds. *Polymer Electrolyte Fuel Cells*; Wiley-VCH: New York, 1997; Vol. 5.
- [31] Gasteiger, H. A.; Markovic, N.; Ross, P. N.; Cairns, E. J. *J. Phys. Chem.* **1994**, *98*, 617-625.

- [32] Eikerling, M.; Kornyshev, A. A.; Kucernak, A. R. *Phys. Today* **2006**, *59*, 38-44.
- [33] St-Pierre, J.; Wilkinson, D. P.; Knights, S.; Bos, M. L. *J. New Mater. Electrochem. Syst.* **2000**, *3*, 99-106.
- [34] Rodatz, P.; Büchi, F.; Onder, C.; Guzzella, L. *J. Power Sources* **2004**, *128*, 208-217.
- [35] Knights, S. D.; Colbow, K. M.; St-Pierre, J.; Wilkinson, D. P. *J. Power Sources* **2004**, *127*, 127-134.
- [36] Lee, S. J.; Mukerjee, S.; McBreen, J.; Rho, Y. W.; Kho, Y. T.; Lee, T. H. *Electrochim. Acta* **1998**, *43*, 3693-3701.
- [37] Barbir, F. In *PEM Fuel Cells: Theory and Practice*; Elsevier Academic Press: San Diego, 2005, 249-270.
- [38] Bıykoğlu, A. *Int. J. Hydrogen Energy* **2005**, *30*, 1181-1212.
- [39] Weber, A. Z.; Newman, J. *Chem. Rev.* **2004**, *104*, 4679-4726.
- [40] Wang, C.-Y. *Chem. Rev.* **2004**, *104*, 4727-4765.
- [41] Cheddie, D.; Munroe, N. *J. Power Sources* **2005**, *147*, 72-84.
- [42] Panchenko, A.; Dilger, H.; Möller, E.; Sixt, T.; Roduner, E. *J. Power Sources* **2004**, *127*, 325-330.
- [43] Panchenko, A.; Dilger, H.; Kerres, J.; Hein, M.; Ullrich, A.; Kaz, T.; Roduner, E. *Phys. Chem. Chem. Phys.* **2004**, *6*, 2891-2894.
- [44] Argyropoulos, P.; Scott, K.; Taama, W. M. *J. Appl. Electrochem.* **1999**, *29*, 661-669.
- [45] Argyropoulos, P.; Scott, K.; Taama, W. M. *Electrochim. Acta* **1999**, *44*, 3575-3584.
- [46] Nordlund, J.; Picard, C.; Birgersson, E.; Vynnycky, M.; Lindbergh, G. J. *Appl. Electrochem.* **2004**, *34*, 763-770.



- [47] Scott, K.; Argyropoulos, P.; Yiannopoulos, P.; Taama, W. M. *J. Appl. Electrochem.* **2001**, *31*, 823-832.
- [48] Theodorakakos, A.; Ous, T.; Gavaises, M.; Nouri, J. M.; Nikolopoulos, N.; Yanagihara, H. *J. Colloid Interface Sci.* **2006**, *300*, 673-687.
- [49] Tüber, K.; Poćza, D.; Hebling, C. *J. Power Sources* **2003**, *124*, 403-414.
- [50] Lu, G. Q.; Wang, C. Y. *J. Power Sources* **2004**, *134*, 33-40.
- [51] Yang, H.; Zhao, T. S.; Cheng, P. *Int. J. Heat Mass Tran.* **2004**, *47*, 5725-5739.
- [52] Yang, H.; Zhao, T. S.; Ye, Q. *J. Power Sources* **2005**, *139*, 79-90.
- [53] Yang, X. G.; Zhang, F. Y.; Lubawy, A. L.; Wang, C. Y. *Electrochem. Solid-State Lett.* **2004**, *7*, A408-A411.
- [54] Fushinobu, K.; Shimizu, K.; Miki, N.; Okazaki, K. *J. Fuel Cell Sci. Tech.* **2006**, *3*, 13-17.
- [55] Bellows, R. J.; Lin, M. Y.; Arif, M.; Thompson, A. K.; Jacobson, D. J. *Electrochem. Soc.* **1999**, *146*, 1099-1103.
- [56] Hickner, M. A.; Siegel, N. P.; Chen, K. S.; McBrayer, D. N.; Hussey, D. S.; Jacobson, D. L.; Arif, M. *J. Electrochem. Soc.* **2006**, *153*, A902-A908.
- [57] Pekula, N.; Heller, K.; Chuang, P. A.; Turhan, A.; Mench, M. M.; Brenizer, J. S.; Ünlü, K. *Nucl. Instrum. Methods Phys. Res., Sect. A* **2005**, *542*, 134-141.
- [58] Satija, R.; Jacobson, D. L.; Arif, M.; Werner, S. A. *J. Power Sources* **2004**, *129*, 238-245.
- [59] Schneider, I. A.; Kramer, D.; Wokaun, A.; Scherer, G. G. *Electrochem. Commun.* **2005**, *7*, 1393-1397.
- [60] Zhang, J.; Kramer, D.; Shimoi, R.; Ono, Y.; Lehmann, E.; Wokaun, A.; Shinohara, K.; Scherer, G. G. *Electrochim. Acta* **2006**, *51*, 2715-2727.
- [61] Geiger, A. B.; Tsukada, A.; Lehmann, E.; Vontobel, P.; Wokaun, A.; Scherer, G. G. *Fuel Cells* **2002**, *2*, 92-98.

- [62] Kramer, D.; Lehmann, E.; Frei, G.; Vontobel, P.; Wokaun, A.; Scherer, G. G. *Nucl. Instrum. Methods Phys. Res., Sect. A* **2005**, *542*, 52-60.
- [63] Kramer, D.; Zhang, J.; Shimoi, R.; Lehmann, E.; Wokaun, A.; Shinohara, K.; Scherer, G. G. *Electrochim. Acta* **2005**, *50*, 2603-2614.
- [64] Feindel, K. W.; Bergens, S. H.; Wasylishen, R. E. *ChemPhysChem* **2006**, *7*, 67-75.
- [65] Feindel, K. W.; Bergens, S. H.; Wasylishen, R. E. *J. Am. Chem. Soc.* **2006**, *128*, 14192-14199.
- [66] Feindel, K. W.; LaRocque, L. P. A.; Starke, D.; Bergens, S. H.; Wasylishen, R. E. *J. Am. Chem. Soc.* **2004**, *126*, 11436-11437.
- [67] Tsushima, S.; Teranishi, K.; Nishida, K.; Hirai, S. *Magn. Reson. Imaging* **2005**, *23*, 255-258.
- [68] Teranishi, K.; Tsushima, S.; Hirai, S. *Therm. Sci. Eng.* **2002**, *10*, 59-60.
- [69] Teranishi, K.; Tsushima, S.; Hirai, S. *Therm. Sci. Eng.* **2003**, *11*, 35-36.
- [70] Teranishi, K.; Tsushima, S.; Hirai, S. *Therm. Sci. Eng.* **2004**, *12*, 91-92.
- [71] Teranishi, K.; Tsushima, S.; Hirai, S. *J. Electrochem. Soc.* **2006**, *153*, A664-A668.
- [72] Teranishi, K.; Tsushima, S.; Hirai, S. *Electrochem. Solid-State Lett.* **2005**, *8*, A281-A284.
- [73] Tsushima, S.; Teranishi, K.; Hirai, S. *Energy* **2005**, *30*, 235-245.
- [74] Tsushima, S.; Teranishi, K.; Hirai, S. *Electrochem. Solid-State Lett.* **2004**, *7*, A269-A272.
- [75] Tsushima, S.; Teranishi, K.; Hirai, S. *Therm. Sci. Eng.* **2003**, *11*, 31-32.
- [76] Minard, K. R.; Viswanathan, V. V.; Majors, P. D.; Wang, L.-Q.; Rieke, P. C. *J. Power Sources* **2006**, *161*, 856-863.

## Chapter 4. PEMFCs and Experimental Setup

Portions of this chapter are reproduced with permission from: Feindel, K.W., Bergens, S.H., and Wasylshen, R.E., *ChemPhysChem*, **2006**, 7, 67-75 (Copyright 2006 Wiley Interscience); Feindel, K.W., Bergens, S.H., and Wasylshen, R.E., *J. Am. Chem. Soc.*, **2006**, 128, 14192-14199 (Copyright 2006 American Chemical Society).

### 4.1. Construction of PEMFCs

The basic design requirements of the PEMFCs for use in  $^1\text{H}$  NMR microscopy investigations were produced in a joint venture with Prof. S. H. Bergens, and D. Starke (Department of Chemistry Machine Shop). Instructions and tips for assembly and maintenance of the PEMFCs are in Appendix B.

#### 4.1.1. 30 mm PEMFC

The first PEMFC for NMR microscopy experiments was designed to fit within a 30 mm outer-diameter glass sample holder. A fundamental requirement for the materials used is that they be non-magnetic. Commercial fuel cells are generally constructed with conductive materials into which the gas flow channels are machined, such that the ribs of the channels can function as a current collector. However, pulsed RF or magnetic fields can induce currents or large voltages ( $10^2$  V) in conductors, and conductors attenuate RFs in the MHz region. Therefore only those conductive materials essential to the operation of the fuel cell were retained (*i.e.*, GDL/current collector and Au wire). A schematic of the design and photographs of the PEMFC are shown in Figure 4-1. Non-conductive polyoxymethylene (Delrin) was selected to machine the fuel cell housing for its hard, durable, and acid resistant properties. The fuel cell assembly consists of two half cylindrical blocks which can be attached with screws. A gas inlet and outlet are machined through the top of each half of the PEMFC body and lead to a combination of channels machined into the flat face of the cylinder half, which

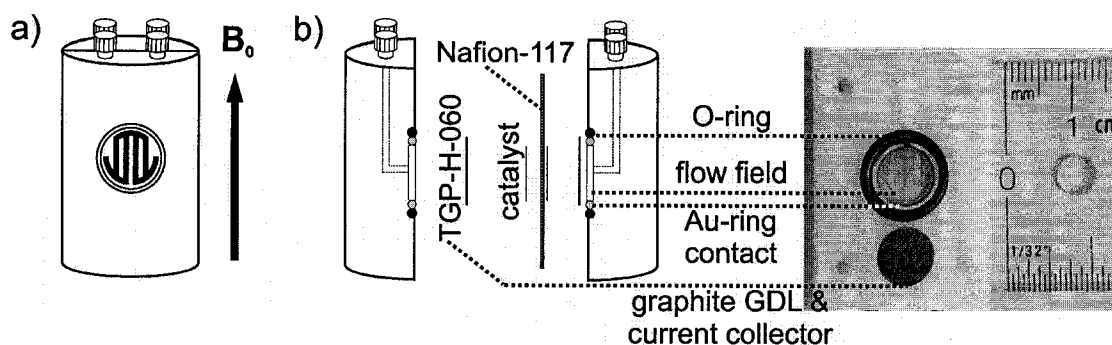


**Figure 4-1.** (a) Representation of the assembled PEMFC indicating the orientation and location of the flow fields and (b) assembly schematic and photograph indicating the components and their location. Photograph courtesy of S.H. Bergens.

constitutes the gas flow field. The gas tubes are fed through screws that have a channel machined through the centre and a Viton (copolymer of vinylidene fluoride and hexafluoropropylene) O-ring is placed on each gas tube between the screw and the cell assembly to create a gas-tight seal. The planes of the MEA and the gas flow fields are oriented parallel with the direction of the applied magnetic field,  $B_0$ . The faces of each flow field presses against a GDL and sandwiches the MEA. A Simriz (copolymer of TFE and perfluorovinyl ether) O-ring is seated around each flow field and creates a gas-tight seal against the PEM when the two halves of the fuel cell assembly are screwed together. Figure 4-1b shows a view of the disassembled PEMFC and a photograph of one half of the cell that illustrates some of the components. Au wire, used as the electrical circuit contact, enters through the rounded side of each cylinder half (see Figure 4-2a) and forms an unclosed ring around the flow field. A photograph of the assembled PEMFC with gas-feed tubes and RF shielded cables attached and supported in the scaffold is shown in Figure 4-2b. Either RG-6U or Belden 9264 RF shielded cables were used; numerous other cables were found to be magnetic.

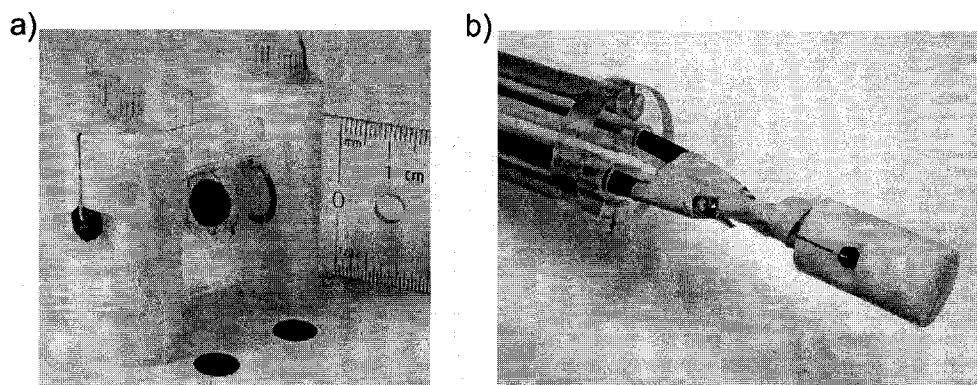


**Figure 4-2.** Photographs of (a) the disassembled PEMFC with the MEA suspended between the two halves of the cell and the discs of Toray TGP-H-060 and (b) the assembled PEMFC and the scaffold constructed to support the gas feed tubes and RF shielded cables. Photographs courtesy of S.H. Bergens.

#### 4.1.2. 10 mm PEMFC

A second PEMFC was designed and constructed to fit within a 10 mm birdcage resonator. A schematic of the design and photographs of the PEMFC are shown in Figure 4-3. If the birdcage is entered from the bottom, an object with maximum diameter 10.9 mm can be accommodated. In this design, the MEA is oriented perpendicular to  $B_0$ . One half of the PEMFC was machined from a single cylinder; the gas inlet/outlet and channel for the Au wire were machined from one end of the cylinder through to a threaded pedestal into which the horseshoe-shaped flow channel was machined. The other half of the PEMFC was machined in two parts: an inner cylinder containing the flow field and the channels for the inlet/outlet and Au wire, and an outer sheath with threads machined into the inner surface. The gas tubes were sealed as for the 30 mm PEMFC, however the O-rings were punched from the top of latex septa using machined stainless steel dies (see Appendix B). The channels through which the Au wire is placed are sealed in a similar manner. A Viton O-ring is seated around the Au ring and flow channel to create a gas-tight seal

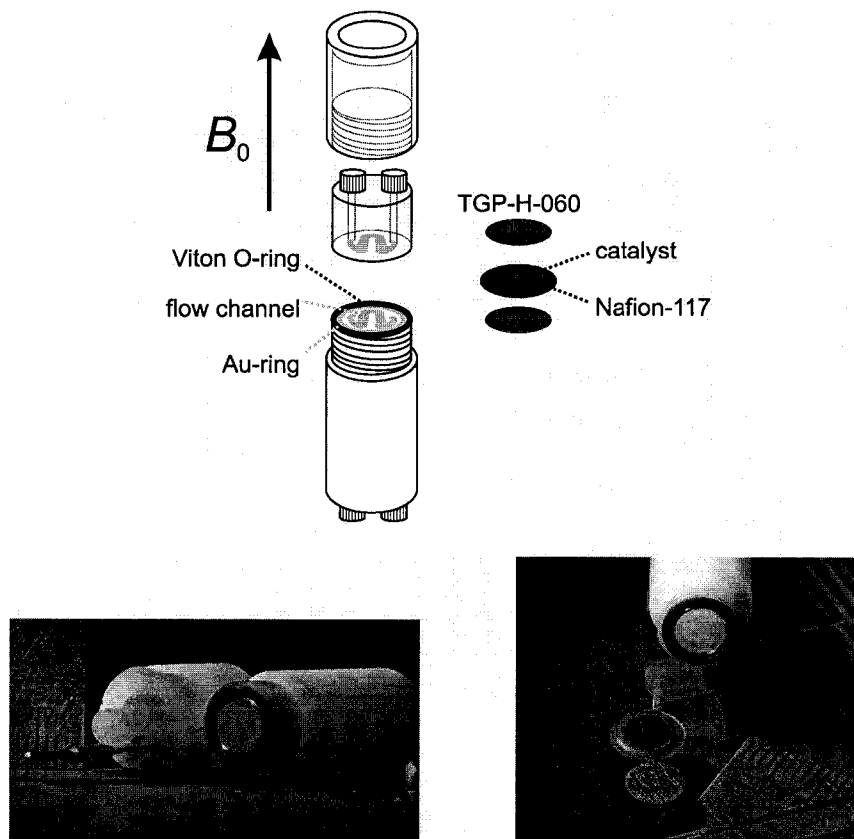


**Figure 4-3.** The assembly schematic (top) and photographs (bottom) show the orientation of the MEA with respect to  $B_0$  and the various components of the 10 mm PEMFC. Photographs courtesy of S.H. Bergens.

against the PEM when the cell is assembled. The assembly design of the PEMFC is similar to the commonly used Swagelok fittings.

#### 4.1.3. Preparation of the Membrane Electrode Assemblies

The MEAs used in preliminary investigations with the 30 mm PEMFC were prepared by L.P.A. LaRocque, at the time an undergraduate student completing research under the supervision of Prof. Bergens. Since January 2005 I have prepared all MEAs used in this research.

The MEAs were prepared according to a modified decal transfer method with materials typically used for PEMFCs fuelled with  $H_2(g)$  or  $MeOH(aq)$ [5]. The PEM is Nafion-117, *i.e.*, 1100 equivalent weight with an as-received thickness of 7 mils. The

Nafion was prepared by boiling in 3% H<sub>2</sub>O<sub>2</sub> for 1 h, followed by boiling for 2 h in 0.5 M H<sub>2</sub>SO<sub>4</sub> (99.9999%). Subsequently, the Nafion was boiled in triple distilled H<sub>2</sub>O(l) for 2.5 h, changing the H<sub>2</sub>O(l) after the first 30 min and again after a further 1 h. Immediately before the catalysts were to be pressed, the Nafion was placed in a vacuum oven at 60 °C for 45 min. The catalysts were prepared as an ink. First, a mixture of 11.5 μL of triple-distilled water per mg of catalyst was sonicated for 45 min. Unsupported HiSpec 1000 Pt black (specific surface area 27 m<sup>2</sup>·g<sup>-1</sup>) and HiSpec 6000 Pt-Ru black (specific surface area 70 m<sup>2</sup>·g<sup>-1</sup>) were used for the cathode and anode catalyst, respectively. Second, 5 mg of 5 wt% Nafion solution (ElectroChem Inc. EC-NS-05) per mg of catalyst was added and the solution was sonicated for 3 h. Once the catalyst inks were prepared they were painted onto Teflon tape that had been lightly sanded with 400-grit sand paper. Templates were used to position the catalyst decals and to restrict the catalyst paint to a circular region of diameter equal to that of the flow field. The Teflon tape was heated to 60 °C, cleaned with acetone and then with dichloromethane prior to painting with the catalysts. The catalyst decals were aligned on the dried Nafion and the components were hot-pressed at a temperature of 126 ± 1 °C for 60 s at a pressure of ~10 MPa. The geometric area of the catalyst decals for the 30 mm PEMFC was ~0.5 cm<sup>2</sup>, with catalyst loadings of ~2-3 mg cm<sup>-2</sup>. The MEAs for the 10 mm PEMFC had geometric areas of ~0.2 cm<sup>2</sup> and catalyst loadings of ~2-3 mg cm<sup>-2</sup>. Toray TGP-H-060 carbon paper (thickness ~190 μm) cut into discs of diameter equal to that of the Au ring, were employed as the gas diffusion layer and current collector.

## 4.2. Experimental Methods

### 4.2.1. Gas Supply and Measuring PEMFC Performance

Pre-purified H<sub>2</sub>(g) (99.995 %) and industrial grade O<sub>2</sub>(g) (99.0 %) obtained from Praxair were supplied at ambient pressure to the PEMFC from compressed gas

cylinders. Gas flow meters were used to control the rate at which pure, humidified  $\text{H}_2(\text{g})$  or dry  $\text{D}_2(\text{g})$  and  $\text{O}_2(\text{g})$  were fed through Teflon tubing to the PEMFC. If necessary, the  $\text{H}_2(\text{g})$  stream could be humidified by flowing the gas through a bubbler containing triple-distilled  $\text{H}_2\text{O}(\text{l})$  at temperatures up to  $90\text{ }^\circ\text{C}$ . The PEMFCs were typically operated at  $20\text{ }^\circ\text{C}$  with dry  $\text{H}_2(\text{g})$  and  $\text{O}_2(\text{g})$  in a counter-flow arrangement. An example gas inlet/outlet configuration for the 30 mm PEMFC is shown in Figure 4-4a and the direction of gas flow in the anode and cathode channels for this configuration, viewed from anode to cathode, is illustrated in Figure 4-4b. An SSI model 300 LC systolic pump was used to flow either triple distilled  $\text{H}_2\text{O}(\text{l})$  or  $\text{D}_2\text{O}(\text{l})$  through the Teflon tubing into the PEMFC. The current drawn from the cell was controlled with a Bourns  $500\ \Omega$  variable resistor, and the current and voltage were monitored using Radio Shack 22-805 multimeters. At a set external resistance the current and voltage were unrestricted and allowed to self-adjust to changes in operating conditions. Shown in Figure 4-5 is an example of the current, voltage, and power response to a change in  $\text{O}_2(\text{g})$  flow rate. The maximum power output from the 30 mm and 10 mm PEMFCs was  $\sim 40\text{ mW}$  (75 to 140 mA, 0.50 to 0.25 V) and  $\sim 25\text{ mW}$  (40 mA, 0.63 V), respectively. Typical polarization curves measured from the 30 mm and 10 mm PEMFCs are shown in Figure 4-6.

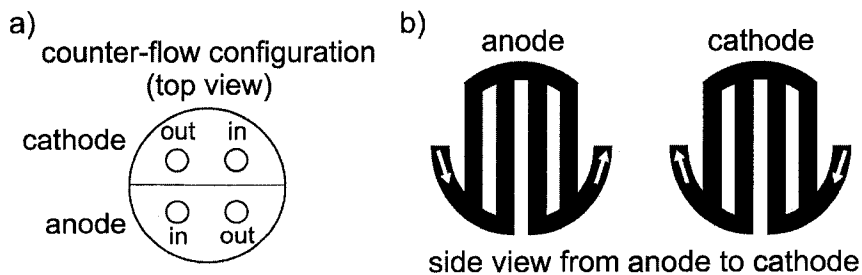


**Figure 4-4.** Representation of (a) the top of the 30 mm PEMFC showing the typical counter-flow configuration of the gas inlets and outlets, and (b) the direction of gas flow in the anode and cathode flow channels as viewed from the anode side of the PEMFC.



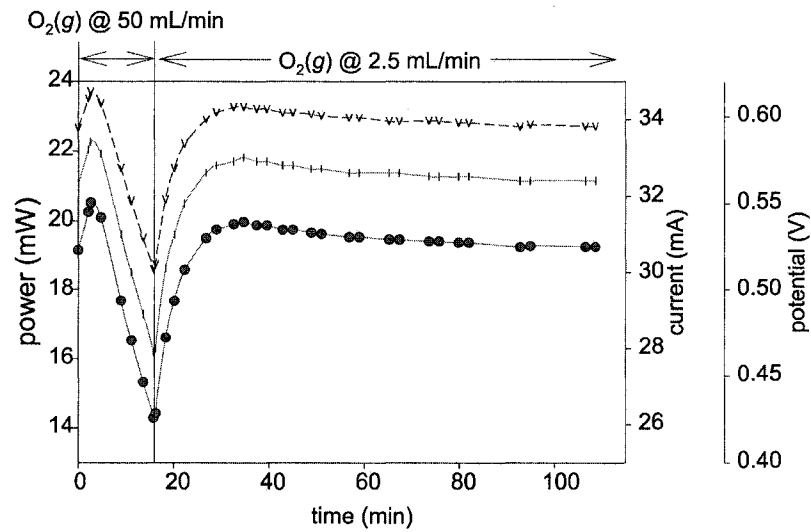


Figure 4-5. Plot of power, potential, and current versus time for the 30 mm PEMFC showing a mutual response of the potential and current. Power(●), potential(V), current(I).

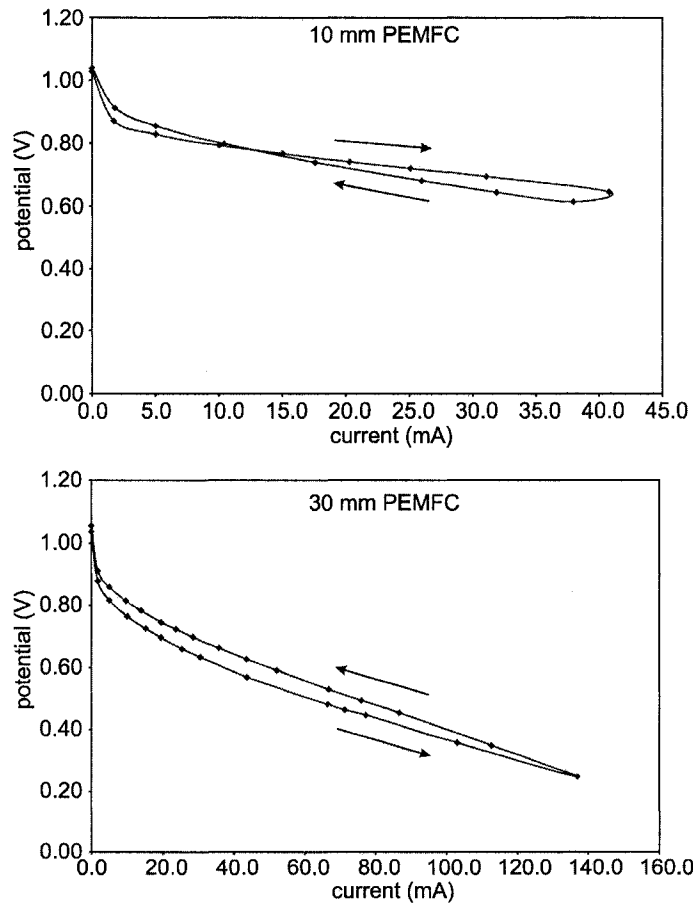


Figure 4-6. Example polarization curves showing the range of current and voltage of the operating 10 mm (top) and 30 mm (bottom) PEMFCs.

We incorporated some practical considerations with respect to the gas flow rates and the current drawn from the cell. The amount of water required to humidify a gas or the humidity ratio,  $\chi$  ( $\text{g}_{\text{water}}/\text{g}_{\text{gas}}$ ), can be calculated according to:

$$\chi = \frac{M_w}{M_{\text{gas}}} \frac{\phi p_{\text{vs}}}{(P - \phi p_{\text{vs}})} \quad (4-1)$$

where  $M_w$  is the molecular weight of water,  $M_{\text{gas}}$  is the molecular weight of the gas being humidified,  $\phi$  is the relative humidity,  $p_{\text{vs}}$  is the saturation pressure (readily found in tables of thermodynamic properties[6]), and  $P$  is total pressure. For our PEMFCs a constant operating temperature of 20 °C was assumed, and the gases were supplied at ambient pressure, therefore  $p_{\text{vs}} = 2.339$  kPa and  $P = 100$  kPa. To achieve 100 % relative humidity (*i.e.*,  $\phi = 1$ ) of  $\text{H}_2(\text{g})$  and  $\text{O}_2(\text{g})$ ,  $0.2140 \text{ g}_{\text{water}}/\text{g}_{\text{hydrogen}}$  and  $0.0135 \text{ g}_{\text{water}}/\text{g}_{\text{oxygen}}$  are required. We typically operated our PEMFCs with dry  $\text{H}_2(\text{g})$  at  $5.0 \text{ mL min}^{-1}$  and dry  $\text{O}_2(\text{g})$  at  $2.5 \text{ mL min}^{-1}$ , and thus  $1.475 \times 10^{-6}$  and  $7.373 \times 10^{-7} \text{ g}_{\text{water}} \text{ s}^{-1}$ , a total of  $2.212 \times 10^{-6} \text{ g}_{\text{water}} \text{ s}^{-1}$  were required to fully humidify the  $\text{H}_2(\text{g})$  and  $\text{O}_2(\text{g})$ , respectively. The rate of water production,  $m_{\text{water}}$  ( $\text{mol s}^{-1}$ ), produced by the reduction of oxygen in a fuel cell can be calculated from Eq. 2 according to Faraday's law:

$$m_{\text{water}} = \frac{I}{2F} \quad (4-2)$$

where  $I$  is the operating current and  $F$  is the Faraday constant,  $96\,485 \text{ C mol}^{-1}$ . Thus, to produce  $2.212 \times 10^{-6} \text{ g}_{\text{water}} \text{ s}^{-1}$  a total cell current of 23.7 mA is required, corresponding to a current density of  $47.4 \text{ mA cm}^{-2}$  for the 30 mm PEMFC. Note that all of the water produced by the reduction of oxygen at this current is required to humidify fully both gases and, at the indicated flow rates, the amount of water required to humidify fully the anode gas stream is twice that required for the cathode gas stream. Since water is only produced at the cathode, and water is

required for proton transport from the anode to cathode, a large concentration gradient from cathode to anode is required to enable back-diffusion of water and facilitate humidification of the anode gas stream.

#### 4.2.2. $^1\text{H}$ NMR Microscopy: Setup

$^1\text{H}$  NMR microscopy experiments were performed using a 7.05 T vertical wide-bore (89 mm) superconducting magnet ( $^1\text{H}$  frequency  $\approx 300$  MHz), Bruker Avance 300 console, and Micro-2.5 imaging accessory. The Bruker water-cooled gradient unit which can produce maximum  $1.0 \text{ T m}^{-1}$  ( $100 \text{ Gauss cm}^{-1}$ ) gradients was maintained at  $20^\circ\text{C}$ , and this was assumed to be the operating temperature of the PEMFC. The schematic for a typical  $^1\text{H}$  NMR microscopy experiment performed on an operating PEMFC in our lab is illustrated in Figure 4-7. Bruker 30 mm or 10 mm inner-diameter  $^1\text{H}$ -tuned birdcage resonators were used for both excitation and detection of the FID. The design of the resonators is similar to that reported by

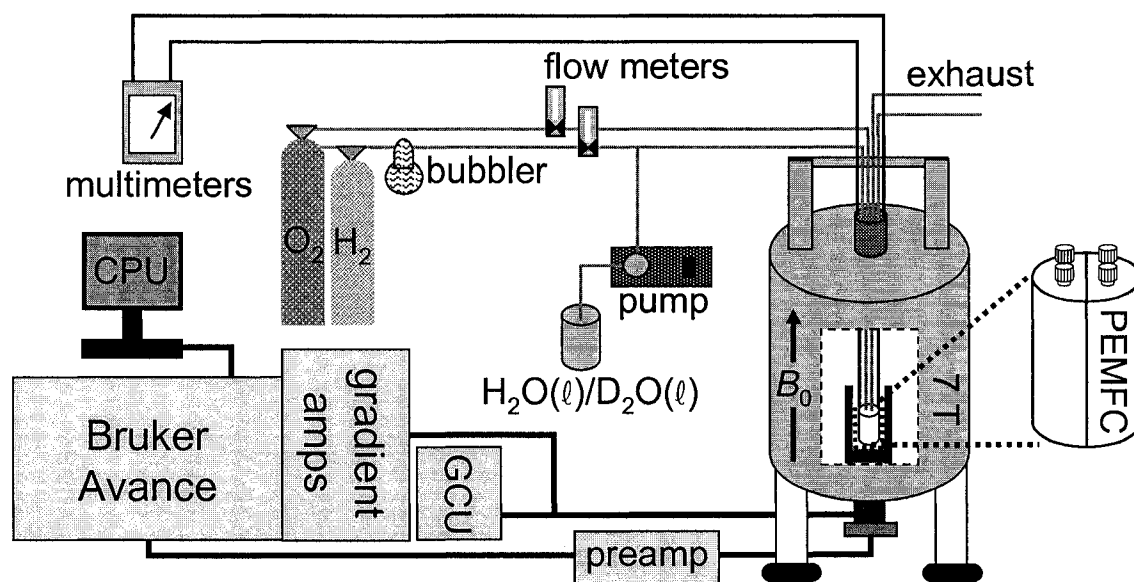


**Figure 4-7.** Schematic of a typical setup used to perform NMR microscopy studies of an operating PEMFC in the vertical wide-bore 7.05 T magnet. The bubbler was filled with pure  $\text{H}_2\text{O}(\ell)$  and could be used to humidify the  $\text{H}_2(\text{g})$  stream at temperatures up to 363 K. GCU = gradient cooling unit.

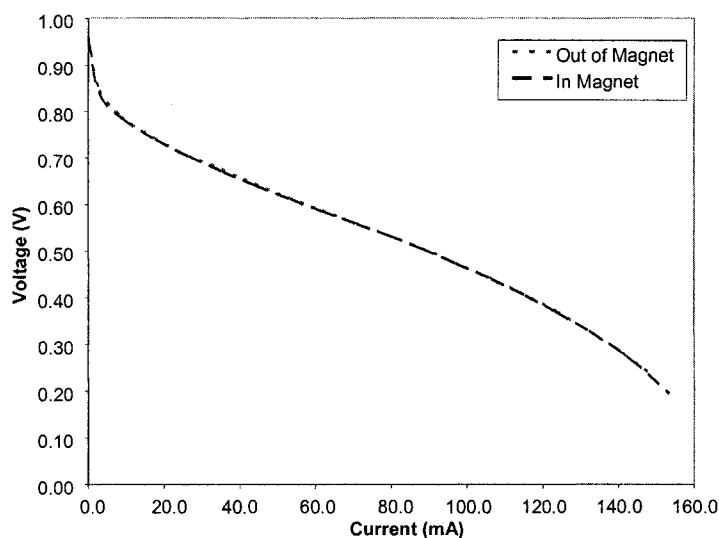


**Figure 4-8.** Example polarization curve measured from the 30 mm PEMFC operating in- and outside the external applied magnetic field.

Crozier *et al.*[7,8] with the rungs electroplated on a TFE substrate, a distributed capacitor design with inter-rung feeding, and a co-cylindrical RF shield. Each Au lead exiting the PEMFC was attached to two RF shielded cables which, along with the gas lines, were supported by a scaffold (see Figure 4-2b) inserted through the top of the magnet bore. As shown by the polarization curves for the 30 mm PEMFC in Figure 4-8, the performance was not affected by the external applied static or pulsed magnetic fields.

#### 4.2.3. $^1\text{H}$ NMR Microscopy: Considerations

Pre-treatment and the amount of water in Nafion are known to affect the  $^1\text{H}$  NMR relaxation times[2-4,9]. A summary of  $^1\text{H}$  NMR  $T_1$  values for pure  $\text{H}_2\text{O}(l)$  at various temperatures and for  $\text{H}_2\text{O}$  in Nafion-117 is provided in Table 4-1. There is a large spread in the  $T_1$  values measured for Nafion. Neither Chen *et al.*[4] nor Fontanella *et al.*[2] reported any membrane pre-treatment to remove possible paramagnetic contaminants. MacMillan *et al.*[3] completed a procedure to convert the Nafion to acid form, and to remove paramagnetics, raw polymer light weight

**Table 4-1.** Summary of  $^1\text{H}$  NMR spin-lattice relaxation times,  $T_1$ , for pure  $\text{H}_2\text{O}(l)$  and  $\text{H}_2\text{O}$  in Nafion-117.

	T [K]	Condition <sup>a</sup>	$T_1$ [ms]	Reference
$\text{H}_2\text{O}(l)$	273		$1730 \pm 35$	[1]
	293		$3150 \pm 63$	[1]
	298		$3570 \pm 71$	[1]
	373		$12\,750 \pm 255$	[1]
Nafion-117	298	4.0 wt%	42	[2] <sup>b</sup>
	298	5.9 wt%	250	[3] <sup>c</sup>
	297	9.8 wt%	57	[4] <sup>d</sup>
	298	10.4 wt %	84	[2] <sup>b</sup>
	298	15.9 wt%	1300	[3] <sup>c</sup>
	297	18.0 wt%	124	[4] <sup>d</sup>
	298	20.8 wt%	110	[2] <sup>b</sup>

a)  $1.66 \text{ wt \%} \approx \lambda = 1$ , where  $\lambda = n\text{H}_2\text{O}/\text{SO}_3\text{H}$

b) Values measured graphically from Figure 6 in Ref. [2].

c) Values measured graphically from Figure 3 in Ref. [3].

d) Values measured graphically from Figure 3 in Ref. [4].

oligomers, and precursor fragments remaining from synthesis; however, their procedure differs from that commonly used for fuel cell applications. Although specific values are not reported, Zawodzinski *et al.*[10] report that for purified, acid-form Nafion-117, the  $^1\text{H}$   $T_1$  values ranged from  $\sim 80$  to 200 ms. In general, the PEM in an operating PEMFC is not saturated with water and the  $T_1$  is reduced significantly when in contact with paramagnetics such as the catalyst layers or  $\text{O}_2(g)$ [11,12]. As well, hot-pressing was found to significantly reduce the ability of Nafion to take up water[13]. In practice,  $T_R = 1.0 \text{ s}$  was found sufficiently long to prevent significant saturation of the  $^1\text{H}$  NMR signal from water in the PEM of a MEA.

For systems with short  $T_2$  values, small diffusion constants, or if weak gradients are used, relaxation broadening will dominate the minimum achievable physical resolution[14]. The longest  $^1\text{H}$   $T_2$  reported for  $\text{H}_2\text{O}$  in Nafion-117 is 750 ms (15.9 wt%, 293 K)[15]; however, the  $T_2$  values observed by Zawodzinski *et al.*[10] were generally half their observed  $T_1$  values. To obtain  $\Delta x \approx 10 \mu\text{m}$  with a typical NMR microscopy gradient strength of  $1.0 \text{ T m}^{-1}$  a linewidth of  $\nu_{1/2} \approx 425 \text{ Hz}$  would be

required, and therefore  $T_2^*$  would have to be 7.4 ms or longer. In an operating PEMFC the  $^1\text{H}$   $T_2^*$  is dependent on temperature, the water content of the PEM, and the homogeneity of the magnetic field experience by the protons. Thus,  $T_2^*$  will vary depending upon the conditions under which the PEMFC is operating, the materials used, and the subsequent ability to make  $B_0$  homogeneous. In addition, the  $^1\text{H}$  NMR chemical shift for OH moieties in Nafion is known range over approximately 5 ppm, increasing with decreasing water content (*e.g.*, 8.5 to 11.9 ppm relative to external TMS for  $\lambda$  between 2.1 and 0.5, respectively)[16]. The resulting spread in  $^1\text{H}$  NMR frequencies may also result in imaging blurring.

#### 4.3. Summary

PEMFCs were designed and constructed with components to facilitate their operation within the available 10 mm and 30 mm birdcage resonators, and within the strong magnetic fields and pulse RF fields necessary for  $^1\text{H}$  NMR microscopy experiments. The PEMFCs were typically operated on controlled flows of pure dry  $\text{H}_2(\text{g})$  and  $\text{O}_2(\text{g})$ , such that the gases were only humidified by the water produced at the cathode. The cell power output was controlled with a variable resistor without restrictions on the current or voltage. The  $T_1$  and  $T_2$  relaxation rates for water in the Nafion-117, as prepared, are expected to be  $< 200$  ms.

#### 4.4. References

- [1] Krynicki, K. *Physica* **1966**, *32*, 167-178.
- [2] Fontanella, J. J.; Edmondson, C. A.; Wintersgill, M. C.; Wu, Y.; Greenbaum, S. G. *Macromolecules* **1996**, *29*, 4944-4951.
- [3] MacMillan, B.; Sharp, A. R.; Armstrong, R. L. *Polymer* **1999**, *40*, 2471-2480.
- [4] Chen, R. S.; Stallworth, P. E.; Greenbaum, S. G.; Fontanella, J. J.; Wintersgill, M. C. *Electrochim. Acta* **1995**, *40*, 309-313.

- [5] Cao, D.; Bergens, S. H. *Electrochim. Acta* **2003**, *48*, 4021-4031.
- [6] *ASHRAE Handbook, Fundamentals*; SI Edition ed.; ASHRAE: Atlanta, 2001.
- [7] Crozier, S.; Luescher, K.; Forbes, L. K.; Doddrell, D. M. *J. Magn. Reson. B* **1995**, *109*, 1-11.
- [8] Crozier, S.; Forbes, L. K.; Roffmann, W. U.; Luescher, K.; Doddrell, D. M. *Meas. Sci. Technol.* **1996**, *7*, 1083-1086.
- [9] Boyle, N. G.; McBrierty, V. J.; Douglass, D. C. *Macromolecules* **1983**, *16*, 75-80.
- [10] Zawodzinski, T. A., Jr.; Neeman, M.; Sillerud, L. O.; Gottesfeld, S. *J. Phys. Chem.* **1991**, *95*, 6040-6044.
- [11] Glasel, J. A. In *Water: A Comprehensive Treatise*; Franks, F., Ed.; Plenum Press: New York, 1972; Vol. 1.
- [12] Hausser, R.; Noack, F. *Z. Naturforsch.* **1965**, *20A*, 1668-1675.
- [13] Cappadonia, M.; Erning, J. W.; Niaki, S. M. S.; Stimming, U. *Solid State Ionics* **1995**, *77*, 65-69.
- [14] Callaghan, P. T. *Principles of nuclear magnetic resonance microscopy*; Oxford University Press: New York, 1991.
- [15] MacMillan, B.; Sharp, A. R.; Armstrong, R. L. *Polymer* **1999**, *40*, 2471-2480.
- [16] Batamack, P.; Fraissard, J. *Catal. Lett.* **1997**, *49*, 129-136.

## Chapter 5. $^1\text{H}$ NMR Microscopy: Non-Operating PEMFCs

Portions of this chapter are reproduced with permission from: Feindel, K.W., Bergens, S.H., and Wasylshen, R.E., *ChemPhysChem*, **2006**, 7, 67-75 (Copyright 2006 Wiley Interscience).

### 5.1. Slice Selection and Image Content

To attain the objectives of this research the various regions inside of an operating PEMFC need to be identified and differentiated. A major benefit of using NMR microscopy is the ability to acquire images from specific defined regions. Filling the anode and cathode flow fields with water allows rapid acquisition of images to determine the alignment of the PEMFC within the gradients and to check the system for leaks and blockages. Once the PEMFC was seated in the birdcage resonator a set of images was obtained from three orthogonal slices. In practice slices were defined and images acquired only from areas of interest, rather than encompassing the entire PEMFC. Isolating small areas in the PEMFC requires fastidious modification of the slice orientation, often down to fractions of a degree and microns. For most experiments the areas of interest were the cathode and anode flow fields and the area between them that contains the MEA.

#### 5.1.1. 30 mm PEMFC

Shown in Figure 5-1 are the three basic classifications of slice orientations relative to a representation of the 30 mm PEMFC. Figure 5-1a shows a vertical *in-plane* slice through the PEMFC which was typically positioned to contain the plane of the MEA or a flow field. The vertical slice orthogonal to the in-plane slice (Figure 5-1b) and the mutually orthogonal *axial* slice (Figure 5-1c) provided *cross-sectional* views of the PEMFC. An example image obtained from the PEMFC when flooded with water using each of the three slice orientations is also shown in Figure 5-1. The image from the in-plane slice shows the design of the flow fields. The cross-



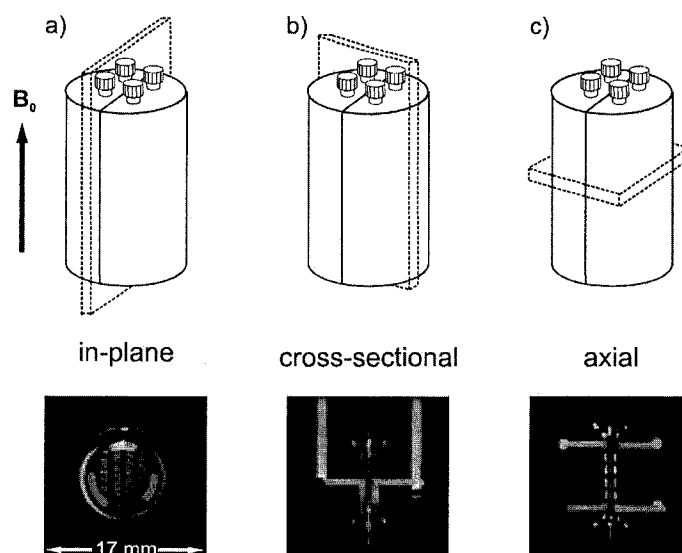


**Figure 5-1.** A schematic indicating the orientation of the three basic mutually orthogonal slices relative to the 30 mm PEMFC and representative  $^1\text{H}$  NMR microscopy images acquired using a SE sequence. Image acquisition parameters: for all images, flip-angle ( $\alpha$ ) =  $90^\circ$ ,  $T_E$  = 5.2 ms,  $\text{MTX} = 128^2$ ; experiment time = 3 h 24 min 48 s; a) slice =  $750\ \mu\text{m}$ ,  $T_R$  = 2 s,  $\text{FOV} = 30\ \text{mm} \times 17\ \text{mm}$  ( $h \times v$ ;  $\text{PE} \times \text{FE}$ ), pixel size =  $234\ \mu\text{m} \times 134\ \mu\text{m}$ , 4 echoes, 1 image, 48 averages; b) slice = 1.0 mm,  $T_R$  = 3 s,  $\text{FOV} = 30\ \text{mm} \times 17\ \text{mm}$  ( $h \times v$ ;  $\text{PE} \times \text{FE}$ ), pixel size =  $234\ \mu\text{m} \times 134\ \mu\text{m}$ , 8 echoes, 1 image, 32 averages; c) slice = 1.0 mm,  $T_R$  = 3 s,  $\text{FOV} = 17\ \text{mm} \times 30\ \text{mm}$  ( $h \times v$ ;  $\text{FE} \times \text{PE}$ ), pixel size =  $134\ \mu\text{m} \times 234\ \mu\text{m}$ , 8 echoes, 1 image, 32 averages.

sectional image was obtained from a slice positioned to include the feed tubes from the top of the PEMFC to the flow channels. Similarly, the image from the axial slice contains the feed tubes, and the individual flow channels are visible as well as the PEM between the flow channels. Figure 5-2 contains a series of images of the water-filled PEMFC showing various orientations of a surface projection generated from a three dimensional dataset acquired with a GE sequence. Visible in the images are the pattern of the flow field, the inlet/outlets, and some of the surrounding PEM.

The physical dimensions of the areas of interest are shown in Figure 5-3. Nafion-117 is known to swell to approximately  $200\ \mu\text{m}$  when in contact with liquid water[1], and each of the Toray-H-060 GDLs is  $190\ \mu\text{m}$  thick. The ability to align slices accurately depends on both the resolution and S/N of the reference image. A series of slices oriented axially most effectively facilitated alignment of an in-plane

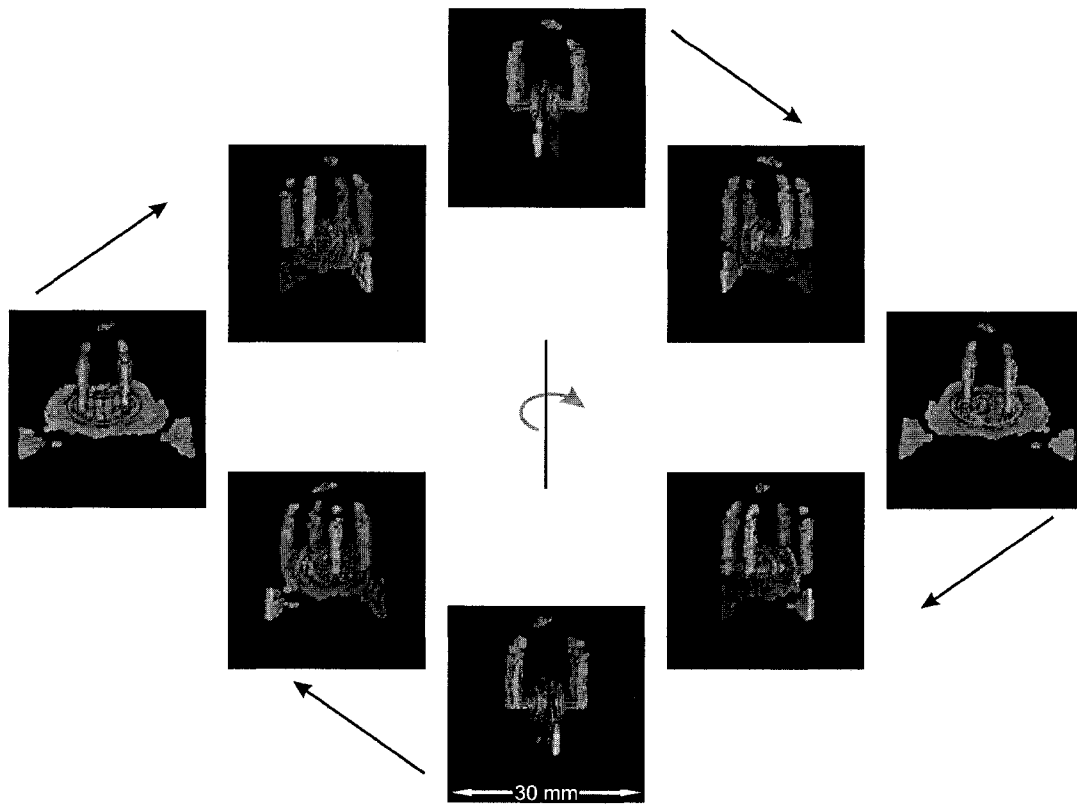


**Figure 5-2.** A series of images acquired from the 30 mm PEMFC filled with water showing various orientations of a surface projection generated from a three-dimensional GE sequence. Image acquisition parameters:  $\alpha = 30^\circ$  ( $100 \mu\text{s}$ ,  $\text{BW} = 12.8 \text{ kHz}$ ),  $T_R = 200 \text{ ms}$ ,  $T_E = 0.85 \text{ ms}$ ,  $\text{FOV} = 30 \text{ mm} \times 30 \text{ mm} \times 60 \text{ mm}$ ,  $\text{MTX} = 128^3$ , pixel size =  $234 \mu\text{m} \times 234 \mu\text{m} \times 469 \mu\text{m}$ , 16 averages, experiment time = 14 h 33 min 49 s.

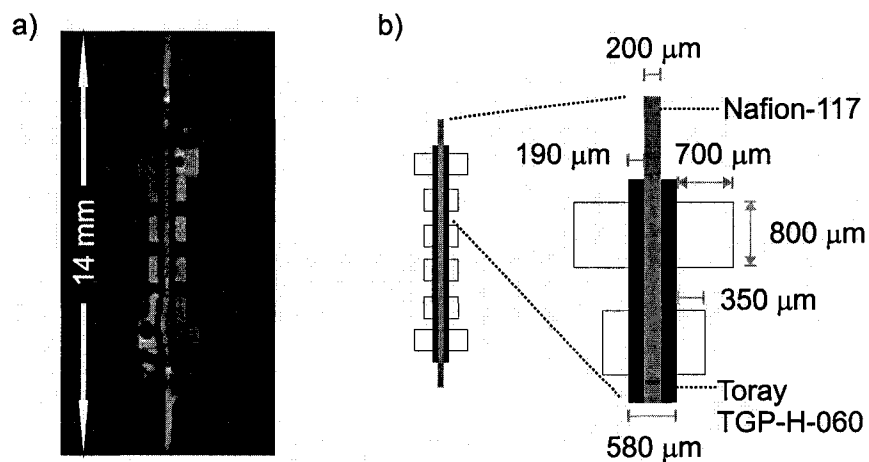


**Figure 5-3.** An axial image of the 30 mm PEMFC filled with water and a schematic showing the dimensions of the PEM, GDLs, and flow channels. Image parameters: SE,  $\alpha = 90^\circ$  ( $1.0 \text{ ms}$ ,  $\text{BW} = 6 \text{ kHz}$ ),  $T_R = 1.5 \text{ s}$ ,  $T_E = 4.7 \text{ ms}$ ,  $\text{FOV} = 14 \text{ mm} \times 14 \text{ mm}$  ( $h \times v$ ;  $\text{PE} \times \text{FE}$ ),  $\text{MTX} = 256^2$ , pixel size =  $55 \mu\text{m} \times 55 \mu\text{m}$ , 16 averages, experiment time = 1 h 42 min 24 s.

slice intended to include the MEA along the z-direction. The resolution needs to be high enough (*i.e.*, image pixels small enough) such that the boundaries between the MEA and the flow fields are well defined. As mentioned previously each pixel represents the average signal within the originating voxel. The resulting blurring may misrepresent the location of an object by approximately a pixel.

The in-plane distribution of water is typically investigated with a set of in-plane slices. In practice a slice thickness of 500  $\mu\text{m}$  is suitable to isolate the MEA from the flow fields, and two neighbouring slices each of 500  $\mu\text{m}$  thickness are required to encompass each flow field. The  $^1\text{H}$  NMR signal from water in the GDLs was not detectable; therefore, the GDL beyond the central slice isolated the  $^1\text{H}$  NMR signal in the MEA from that of water in the flow fields. Of particular interest for these investigations was the distribution of water within the MEA and flow fields and if it correlated with the operating conditions of the PEMFC. Shown in Figure 5-

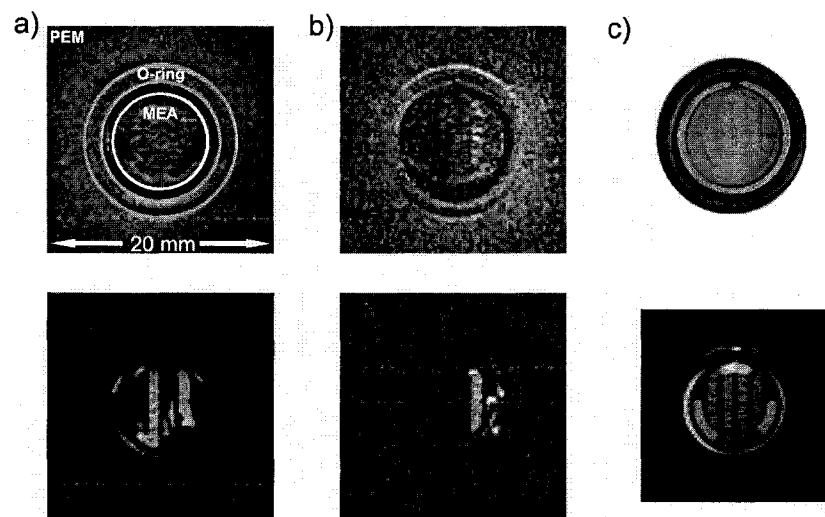


**Figure 5-4.** Images of the MEA (top) and cathode flow field (bottom) of the 30 mm PEMFC obtained from slices of thickness a) 500  $\mu\text{m}$  b) 650  $\mu\text{m}$ . Note that the slice thickness of 650  $\mu\text{m}$  is too large to isolate the MEA from the flow fields. c) Photograph of the region within the O-ring (top) and image of a flow field filled with water. Image parameters: a) and b) SE,  $\alpha = 90^\circ$  (1.0 ms, BW = 6 kHz),  $T_R = 1.0$  s,  $T_E = 3.2$  ms, FOV = 30 mm  $\times$  30 mm (h  $\times$  v; PE  $\times$  FE), MTX = 128<sup>2</sup>, pixel size = 234  $\mu\text{m}$   $\times$  234  $\mu\text{m}$ , 8 echoes, 1 image, 1 average, experiment time = 128 s.

4 are images obtained from in-plane slices of 500  $\mu\text{m}$  and 650  $\mu\text{m}$ . The image obtained from the 650  $\mu\text{m}$  slice centred on the MEA reveals a consequence of inappropriate choice of slice dimensions (Figure 5-4b) if one were to assume that the slice contained only the MEA. The distribution of water in the MEA appears to mimic the flow field pattern in the locations where  $\text{H}_2\text{O}(l)$  accumulates in the cathode flow field. The image obtained from the 500  $\mu\text{m}$  slice, however, reveals that the distribution of water in the MEA does not mimic the neighbouring flow field pattern. In the absence of  $\text{H}_2\text{O}(l)$  in the flow fields such a misrepresentation would not be apparent.

#### 5.1.2. 10mm PEMFC

Shown in Figure 5-5 are the two basic classifications of slice orientations relative to a representation of the 10 mm PEMFC. Due to the placement of the MEA plane perpendicular to  $B_0$ , any vertically positioned slice will provide a cross-sectional view. Images obtained from the PEMFC when filled with water are shown in Figure 5-5. Figure 5-5a shows a vertical cross-sectional slice through the PEMFC. The plane of the MEA and flow channels were incorporated using axial slices (Figure 5-5b). The image from the axial slice shows the design of the flow channels.

#### 5.2. Influence of Materials on the NMR Signal

As mentioned in §4.1.1, high-frequency electromagnetic radiation, such as RF waves in the MHz range, are effectively attenuated by conductors[2]. The through-plane conductivity of the TGP-H-060 carbon paper used in our experiments is 1250  $\text{S m}^{-1}$ [3] which, for a thickness of 190  $\mu\text{m}$ , will attenuate a 300 MHz electromagnetic plane-wave by approximately one-fifth. With the plane of the membrane electrode assembly oriented parallel to  $B_0$ , the maximum signal achievable is dependent upon the orientation of the PEMFC within the birdcage resonator. A quadrature-driven birdcage resonator generates a circularly polarized  $B_1$  field, which can be

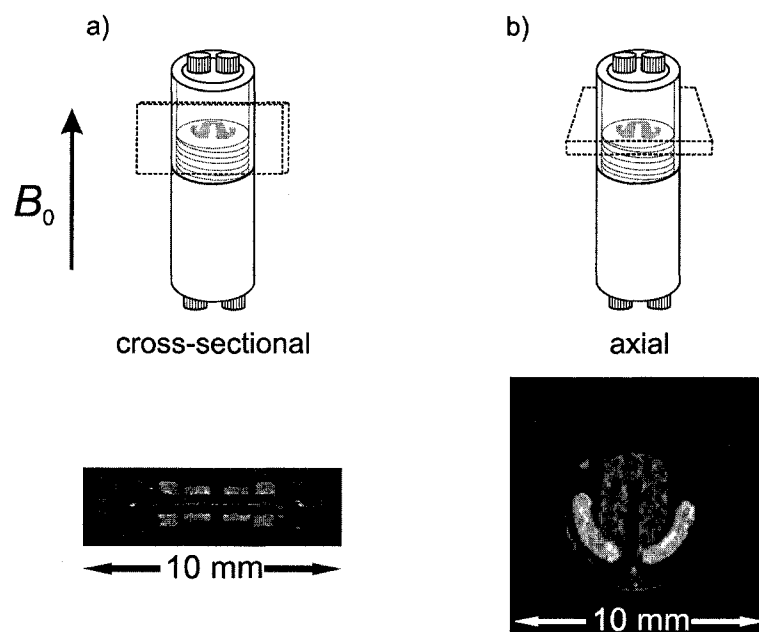


**Figure 5-5.** A schematic indicating the two basic slice orientations relative to the 10 mm PEMFC and representative SE  $^1\text{H}$  NMR microscopy images. Image parameters: a)  $\alpha = 90^\circ$  (1.0 ms, BW = 6 kHz), slice = 500  $\mu\text{m}$ ,  $T_R = 1.5$  s,  $T_E = 5.6$  ms, FOV = 10 mm  $\times$  3.5 mm (h  $\times$  v; PE  $\times$  FE), MTX = 256<sup>2</sup>, pixel size = 39  $\mu\text{m}$   $\times$  14  $\mu\text{m}$ , composite of 4 images from 4 echoes, 64 averages, experiment time = 6 h 49 min 36 s; b)  $\alpha = 90^\circ$  (1.0 ms, BW = 6 kHz), slice = 550  $\mu\text{m}$ ,  $T_R = 1.0$  s,  $T_E = 3.4$  ms, FOV = 10 mm  $\times$  10 mm (h  $\times$  v; FE  $\times$  PE), MTX = 128<sup>2</sup>, pixel size = 78  $\mu\text{m}$   $\times$  78  $\mu\text{m}$ , 8 echoes, 1 image, 1 average, experiment time = 128 s.

represented by two plane-polarized fields oscillating perpendicular to each other and to  $B_0$ . The PEMFC was rotated to a position within the birdcage where maximum  $^1\text{H}$  signal intensity was obtained; positions rotated by  $n\pi/2$ , where  $n$  is an integer, yield equivalent signal intensity.

The image shown in Figure 5-4a was obtained from a 500  $\mu\text{m}$  slice containing the MEA; however, in practice we have found that the  $^1\text{H}$  NMR signal acquired results from water in the PEM only, herein referred to as  $\text{H}_2\text{O}(pem)$ . This is also visible in the axial image in Figure 5-3, where there is an apparent dead space between the central line resulting from  $\text{H}_2\text{O}(pem)$  and the flow channels. Figure 5-6 shows a SE image acquired of the 10 mm PEMFC filled with water, obtained in the 10 mm diameter birdcage resonator with a vertical FE direction. The GDLs used in

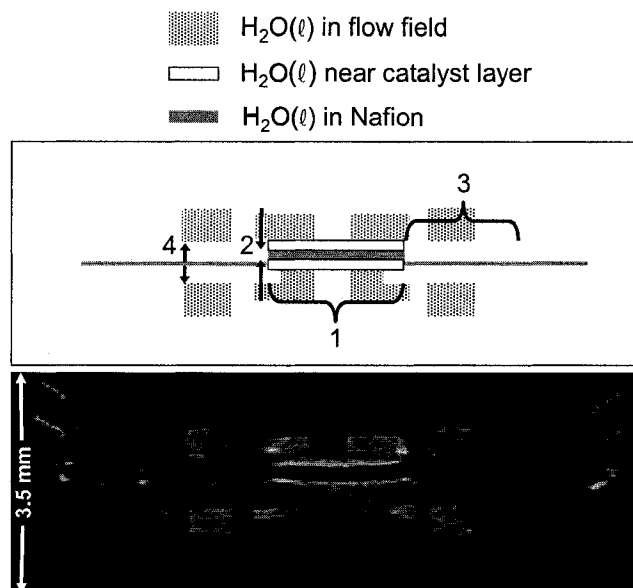


**Figure 5-6.** Bottom:  $^1\text{H}$  NMR microscopy image of the 10 mm PEMFC filled with  $\text{H}_2\text{O}(l)$  obtained with a SE sequence from a  $500\ \mu\text{m}$  slice,  $\alpha = 90^\circ$  (1.0 ms, BW = 6 kHz),  $T_R = 777\ \text{ms}$ ,  $T_E = 4.3\ \text{ms}$ , FOV =  $10\ \text{mm} \times 3.5\ \text{mm}$  ( $h \times v$ ; PE  $\times$  FE), MTX =  $128^2$ , pixel size =  $78\ \mu\text{m} \times 27\ \mu\text{m}$ , composite of 8 images obtained from 8 echoes, 32 averages, experiment time = 53 min 4 s. The angled stripes at the edges of the image are from  $\text{H}_2\text{O}(l)$  in the threads of the PEMFC housing. Top: Representation of bottom image. Region 1: Indicates the area without Toray carbon paper; Region 2:  $\sim 200\ \mu\text{m}$  between the bright bands indicating the approximate thickness of the PEM; Region 3: Indicates the area with Toray carbon paper; Region 4:  $\sim 700\ \mu\text{m}$  separates the signal acquired from  $\text{H}_2\text{O}(l)$  in the flow fields, larger than the  $\sim 580\ \mu\text{m}$  expected from the physical thickness of the Toray ( $2 \times 190\ \mu\text{m}$ ) and Nafion-117 in contact with  $\text{H}_2\text{O}(l)$ .

this case were ring-shaped pieces of Toray TGP-H-060 and the central part of the image (Figure 5-6, Region 1) shows the regions of the MEA that were not in contact with the GDLs. The cross-section of the PEM is shown in this region (Figure 5-6, Region 2), with a thickness of  $\sim 200\ \mu\text{m}$  (approximately the thickness of Nafion-117 when in contact with  $\text{H}_2\text{O}(l)$ [4]). Dark lines are visible at the faces of the MEA that are likely due to nullification of the  $^1\text{H}$  signal at the catalyst layers. The region of the image in Figure 5-6, from which the apparent proton density is negligible (Region 3), contains the Toray carbon paper. The thickness of this region ( $\sim 700\ \mu\text{m}$ ), however, is larger than the physical thickness of the Toray and PEM ( $\sim 580\ \mu\text{m}$ ); the Toray prevents detection of the  $^1\text{H}$  NMR signal from most of the PEM and from the water-

Toray interface (Figure 5-6, Region 4). Water contained in the catalyst layers or GDLs is difficult to observe due to the effects of the properties of the material on the  $^1\text{H}$  NMR signal; rapid relaxation of the transverse magnetization (*i.e.*, measurable NMR signal) results from several influences including the magnetic susceptibility differences, the electrical conductivity, and the paramagnetic nature of some materials[5]. Magnetic susceptibility differences introduce inhomogeneity in the local magnetic field, proportional to both the difference in magnetic susceptibility and the applied external magnetic field. This inhomogeneity results in variations in the NMR resonance frequency of nuclei in that area, and a rapid relaxation of transverse magnetization. Except for simple geometries such as a sphere or cylinder, however, the distortion imparted on a magnetic field by susceptibility effects must be solved numerically[6]. As the carbon paper is conductive, eddy currents could be induced by the applied magnetic field gradients, also disrupting the local magnetic field. An immediate approach to avoid these deleterious effects due to the carbon paper is to design model PEMFCs without carbon GDLs. With the GDLs, however,  $^1\text{H}$  NMR microscopy can provide a *unique* view of water within the PEM between the operating catalysts, separate from other regions of the PEMFC.

For FE experiments, if the spin system is not stationary, image artefacts may evolve due to the length of time that the read gradient is applied. As a result of the translational self-diffusion of water, the bulk  $^1\text{H}$  NMR signal in the flow fields is attenuated over the duration of the NMR acquisition period. At restricted boundaries, however, where the rate of diffusion is relatively slow, this attenuation can be reduced resulting in bright bands at the boundary or so-called "edge-enhancement"[7]. Such diffusive attenuation effects have been shown to become significant when the root mean-squared displacement,  $\langle r^2 \rangle^{1/2}$ , over the acquisition period,  $T_A$ , approaches the pixel size[7]. The bright horizontal lines above and

below the PEM in Figure 5-6, although reminiscent of edge-enhancement, are predominantly caused by a reduction of the  $^1\text{H}$   $T_1$  at the catalyst surface; the NMR signal from water away from this region is partially saturated due to the relatively short delay between excitation pulses,  $T_R = 777$  ms. For fast diffusion, linewidth broadening may reduce the physical resolution of an image and incoherent displacement beyond the voxel length scale to be resolved results in a fading of the voxel contrast. In this case, the time between signal excitation and acquisition is important;  $\langle r^2 \rangle^{1/2}$  can be crudely related to  $T_E$  such that  $\langle r^2 \rangle^{1/2} \approx (6DT_E)^{1/2}$ . For water in Nafion-117, with  $D = 5.8 \times 10^{-10} \text{ m}^2 \text{ s}^{-1}$  ( $\sim 23$  wt%; 298 K)[8] and  $T_E = 5$  ms,  $\langle r^2 \rangle^{1/2} \approx 4 \mu\text{m}$ .

### 5.3. Image Algebra – What is the Difference?

One of the primary objectives of this research was to obtain a visual perspective on the distribution of water in operating PEMFCs. Observing qualitative changes in the distribution of water in the flow fields was relatively simple: there was either signal or no signal. However, variation in  $\text{H}_2\text{O}(pem)$  was not as immediately apparent unless the change was drastic. This was in part a result of the way the images are displayed, *i.e.*, the depth of the gray or color scale, relative to the actual range of the acquired NMR signal. Instructions and tips for displaying images on the same intensity scale are in Appendix C. To facilitate better perceptual acuity to changes in  $\text{H}_2\text{O}(pem)$ , the difference in the signal intensity between two images was calculated and displayed. The images in Figure 5-7a were obtained from the 30 mm PEMFC when  $\text{H}_2\text{O}(l)$  had accumulated in the cathode flow field (bottom) and those in Figure 5-7b were obtained after the  $\text{H}_2\text{O}(l)$  was purged with an  $\text{O}_2(g)$  flow rate of  $50 \text{ mL min}^{-1}$ . Subtracting the images in (b) from those in (a) yields the corresponding difference images that show the change in  $^1\text{H}$  NMR signal and therefore water content.



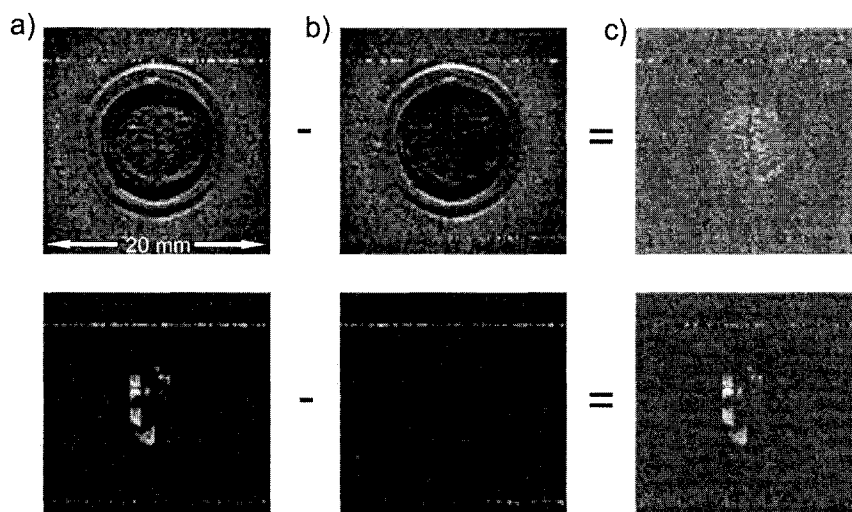


**Figure 5-7.** An example of the calculation of difference images to show the change in water content the MEA (top) and the cathode flow field (bottom) of the 30 mm PEMFC. The images were obtained when: (a)  $\text{H}_2\text{O}(l)$  had accumulated in the cathode flow field, and b) after the  $\text{H}_2\text{O}(l)$  was purged with an  $\text{O}_2(g)$  flow rate of  $50 \text{ mL min}^{-1}$ . The images in (c) show the result of subtracting the images in (b) from those in (a). Image acquisition parameters: a) and b) SE,  $\alpha = 90^\circ$  (1.0 ms, BW = 6 kHz), slice =  $500 \mu\text{m}$ ,  $T_R = 1.0 \text{ s}$ ,  $T_E = 3.2 \text{ ms}$ , FOV =  $30 \text{ mm} \times 30 \text{ mm}$  ( $h \times v$ ; PE  $\times$  FE), MTX =  $128^2$ , pixel size =  $234 \mu\text{m} \times 234 \mu\text{m}$ , 8 echoes, 1 image, 1 average, experiment time = 128

#### 5.4. Summary

This chapter presented  $^1\text{H}$  NMR microscopy images acquired from the 30 mm and 10 mm PEMFCs filled with  $\text{H}_2\text{O}(l)$ . The images show the dimensions of the flow fields and MEA and facilitated alignment of slices encompassing specific areas such as the MEA. Influences of the materials used to construct the PEMFCs on the  $^1\text{H}$  NMR microscopy signal were considered, and the carbon GDL was found to prevent detection of the signal. In practice, the  $^1\text{H}$  NMR signal obtained from slices containing the MEA and GDLs results from only water in the PEM,  $\text{H}_2\text{O}(pem)$ . As well, the use of difference images was introduced as a method for observing changes in the distribution and content of water between two images.

## 5.5. References

- [1] Gebel, G.; Aldebert, P.; Pineri, M. *Polymer* **1993**, *34*, 333-339.
- [2] Cheng, D. K. *Field and wave electromagnetics*; Addison-Wesley: New York, 1989.
- [3] Barbir, F. In *PEM Fuel Cells: Theory and Practice*; 73-113, Ed.; Elsevier Academic Press: San Diego, 2005, 115-145.
- [4] Hinatsu, J. T.; Mizuhata, M.; Takenaka, H. *J. Electrochem. Soc.* **1994**, *141*, 1493-1498.
- [5] Feindel, K. W.; Bergens, S. H.; Wasylshen, R. E. *ChemPhysChem* **2006**, *7*, 67-75.
- [6] Bakker, C. J.; Bhagwandien, R.; Moerland, M. A.; Ramos, L. M. *Magn. Reson. Imaging* **1994**, *12*, 767-774.
- [7] Callaghan, P. T. *Principles of nuclear magnetic resonance microscopy*; Oxford University Press: New York, 1991.
- [8] Zawodzinski, T. A., Jr.; Neeman, M.; Sillerud, L. O.; Gottesfeld, S. *J. Phys. Chem.* **1991**, *95*, 6040-6044.

## Chapter 6. The Distribution of Water in an Operating PEMFC

Portions of this chapter are reproduced with permission from: Feindel, K.W., LaRocque, L.P.A., Starke, D., Bergens, S.H., and Wasylishen, R.E., *J. Am. Chem. Soc.*, **2004**, *126*, 11436-11437 (Copyright 2004 American Chemical Society) and Feindel, K.W., Bergens, S.H., and Wasylishen, R.E., *J. Am. Chem. Soc.*, **2006**, *128*, 14192-14199 (Copyright 2006 American Chemical Society).

### 6.1. Introduction

In an operating PEMFC water is in the PEM, catalysts, GDLs, flow fields, and gas streams. One of the major benefits of using PEMFCs as a source of power is that water is produced as exhaust at the cathode. Unfortunately, the effectiveness of the most commonly used PEMs (*i.e.*, perfluorosulfonated ionmers) depends critically on water. As a result, maintaining conditions such that PEMFCs can perform optimally over a wide range of operating conditions (*e.g.*, power demands, temperatures, orientations, *etc.*) is a major obstacle delaying widespread manufacturing and implementation of PEMFCs. Solving this problem has been particularly difficult due to the lack of experimental information regarding the dynamic distribution of water in operating PEMFCs. Proton NMR microscopy provides the opportunity to investigate the impact of parameters such as gas flow rate or humidification, temperature, and circuit resistance on the amount of water throughout a PEMFC, and to correlate the observations with changes in fuel cell performance.

In this chapter, results from the preliminary  $^1\text{H}$  NMR microscopy investigations of the operating 30 mm PEMFC[2] are presented first. During this exploratory period of experiments, the ability of GE and SE experiments to reveal the distribution of water in an operating PEMFC was investigated. Second, the feasibility of using  $^1\text{H}$  NMR microscopy to monitor the distribution of water in the

PEM between the catalyst layers (*i.e.*, the MEA) was demonstrated[3]. The interdependence of gas flow rates, gas inlet/outlet configuration, cell power output, and MEA water content is investigated. In addition, the results from  $^1\text{H}$  NMR microscopy experiments are discussed in relation to predictions from relevant theoretical models.

## 6.2. Experimental Details

Pre-purified  $\text{H}_2(\text{g})$  (99.995%) and industrial grade  $\text{O}_2(\text{g})$  (99.0%) were supplied at ambient pressure to the 30 mm PEMFC from compressed gas cylinders *via* flow meters. All gases were obtained from Praxair. Dry gases were used, and unless otherwise stated, the  $\text{H}_2(\text{g})$  flow rate was  $5 \text{ mL min}^{-1}$  and  $\text{O}_2(\text{g})$  flow rate was  $2.5 \text{ mL min}^{-1}$ .

Unless otherwise stated, a typical slice-selective SE imaging sequence[4] was used to obtain images from a  $30 \text{ mm} \times 30 \text{ mm}$  FOV. Five slices of thickness  $500 \mu\text{m}$  were oriented such that the entire PEM and most of each GDL were contained within the central slice and the anode and cathode flow fields contained in the neighbouring slices. The FE direction was parallel with the plane of the MEA and  $B_0$ . 128 FE and 128 PE steps were used, yielding an in-plane pixel size of  $234 \mu\text{m} \times 234 \mu\text{m}$ . In all experiments, the receiver BW was 101010.1 Hz, the time between  $^1\text{H}$  NMR signal excitation and acquisition of the first echo,  $T_E$ , was 3.2 ms, and in total eight echoes were co-added after each excitation. The length of the RF excitation pulse was 1.0 ms with a BW of 6 kHz and a flip angle,  $\alpha$ , of  $90^\circ$ . The repeat time between successive  $^1\text{H}$  NMR signal excitations,  $T_R$ , was 1.0 s, resulting in a time of 128 s per experiment.

## 6.3. Diffusion of Water away from the MEA

To initiate our investigations a baseline condition of the PEMFC was first established. Prior to drawing a current from the PEMFC (*i.e.*, prior to producing

water), humidified  $\text{H}_2(\text{g})$  and dry  $\text{O}_2(\text{g})$  were used to flush the flow fields until the amount of water imaged in the PEM,  $\text{H}_2\text{O}(\text{pem})$ , inside and around the MEA appeared constant in the  $^1\text{H}$  NMR microscopy images. The image shown in Figure 6-1A, acquired with the PEMFC at a potential of  $\sim 1$  V, represents the amount of water in the PEM as established by the humidified  $\text{H}_2(\text{g})$  and dry  $\text{O}_2(\text{g})$ . To draw attention to the region outside of the MEA, a GE imaging sequence was used. The detectable NMR response in regions near the catalyst relaxes quickly due to the local inhomogeneities in the applied magnetic field, and as a result only the  $^1\text{H}$  NMR signal from water in more homogeneous regions (*i.e.*, the PEM surrounding the catalyst region) was observed. Subsequently the PEMFC was operated at  $52 \text{ mA}\cdot\text{cm}^{-2}$  and  $0.73$  V for 6 h. As shown in Figure 6-1B the amount of  $\text{H}_2\text{O}(\text{pem})$  surrounding the MEA and outside the O-ring seals increased.

The protons transferred from the anode through the PEM to the cathode are co-transported with water *via* electro-osmotic drag. Thus, water enters the PEM at the anode from the humidified  $\text{H}_2(\text{g})$  to facilitate electro-osmotic drag. During the 6 h period of operation approximately  $5.2 \times 10^{-2}$  g of water was produced by the

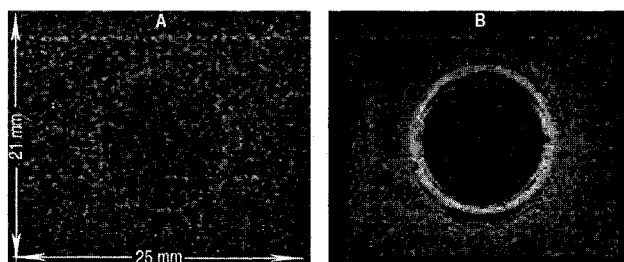


**Figure 6-1.**  $^1\text{H}$  NMR microscopy images acquired with a GE sequence from a slice containing the MEA of the 30 mm PEMFC, showing the PEM around the MEA: (A) before current was passed through the cell and (B) after operating the fuel cell at  $\sim 52 \text{ mA cm}^{-2}$  and  $\sim 0.73$  V for 6 h. Comparison of images A and B demonstrates the diffusion of water through the Nafion membrane away from the MEA. Image acquisition parameters:  $\alpha = 30^\circ$  (  $1.0$  ms,  $\text{BW} = 6$  kHz), slice =  $700 \mu\text{m}$ ,  $T_R = 200$  ms,  $T_E = 1.9$  ms,  $\text{FOV} = 30 \text{ mm} \times 21 \text{ mm}$  (  $h \times v$ ;  $\text{PE} \times \text{FE}$ ),  $\text{MTX} = 128^2$ , pixel size =  $234 \mu\text{m} \times 164 \mu\text{m}$ , 32 averages, experiment time = 13 min 39 s.

reduction of oxygen at the cathode (see §4.2.1) and a portion of the water diffused back into the PEM. Comparison of the images in Figure 6-1A and 6-1B reveals that some of the water within the PEM also diffused radially down the concentration gradient outward from the MEA. The apparent  $^1\text{H}$  spin density in areas where the local magnetic field is inhomogeneous (*e.g.*, near the MEA) appears negligible when using a GE. GE experiments are generally used for homogeneous systems, or if contrast due to small susceptibility differences is desired, *e.g.*, imaging a plant stem[5]. This observation suggests that such diffusion will reduce flooding of cathode catalyst sites near the edges of MEAs and will decrease the amount of  $\text{H}_2\text{O}(pem)$  between the catalyst layers. The rate of proton transport through the PEM *via* electro-osmotic drag is known to be higher with greater PEM water content[6,7] and therefore, diminishing the amount of  $\text{H}_2\text{O}(pem)$  between the catalyst layers may decrease fuel cell performance. The relative effects of the counter-acting phenomena on fuel cell performance is likely related to a number of physical factors including the circumference and area of the catalyst decal, and the volume of PEM surrounding the catalyst decals.

#### 6.4. Water in the MEA and Flow Fields

As mentioned in Chapter 3, blocking of the gas flow channels by  $\text{H}_2\text{O}(l)$  is problematic and is typically indicated by unexpected drops in power output and/or pressure changes within the fuel cell. Many factors that influence the performance of a PEMFC are interrelated. For example, decreasing the resistive load on the circuit will increase the current and the larger number of protons transported through the PEM from anode to cathode will co-transport more water from the anode, and at the cathode more oxygen will be reduced to water.

As shown by the image in Figure 6-2A, less water appears to be contained in the MEA than in the region of the PEM in direct contact with the  $\text{H}_2\text{O}(l)$  pooled

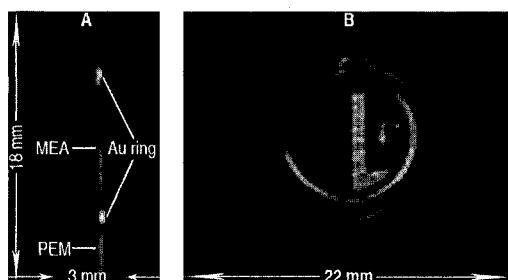


**Figure 6-2.**  $^1\text{H}$  NMR microscopy images of the 30 mm PEMFC operating at  $\sim 52 \text{ mA cm}^{-2}$  and  $\sim 0.73 \text{ V}$  acquired with a SE sequence with  $\alpha = 90^\circ$ : (A) After operating for  $\sim 30 \text{ h}$ , slice = 1.0 mm,  $T_R = 3.0 \text{ s}$ ,  $T_E = 5.0 \text{ ms}$ , FOV = 3.5 mm  $\times$  30 mm (h  $\times$  v; FE  $\times$  PE), MTX = 196  $\times$  128, pixel size = 15  $\mu\text{m}$   $\times$  234  $\mu\text{m}$ , 8 echoes, 1 image, 128 averages, experiment time = 13 h 39 min. (B) View of partially blocked cathode flow field after operating for  $\sim 72 \text{ h}$ ; outside rings indicate pooling of water around the Au ring; slice = 700  $\mu\text{m}$  slice,  $T_R = 2.0 \text{ s}$ ,  $T_E = 3.2 \text{ ms}$ , FOV = 30 mm  $\times$  22 mm (h  $\times$  v; PE  $\times$  FE), MTX = 128<sup>2</sup>, pixel size = 234  $\mu\text{m}$   $\times$  172  $\mu\text{m}$ , 16 echoes, 1 image, 4 averages, experiment time = 17 min.

around the Au ring contact. If sufficient water does not diffuse back into the PEM at the cathode or evaporate into the  $\text{O}_2(\text{g})$  flow,  $\text{H}_2\text{O}(\text{l})$  will form in the GDL and accumulate in the cathode flow field. Transient water blockages in the cathode flow channels were observed (see Figure 6-2B), depending on the conditions under which the PEMFC was operated, and resulted in fluctuations in fuel cell performance. A rheostat was used to regulate the resistive load placed on the operating PEMFC and the voltage and current were allowed to self-regulate. Thus any change in fuel cell power output was observed as a variation in both current and voltage. To prevent dehydration of the PEM at the anode due to electro-osmotic drag, the  $\text{H}_2(\text{g})$  stream is often saturated with water prior to entering the anode flow field. However, if sufficient water is not transported into the PEM and across to the cathode,  $\text{H}_2\text{O}(\text{l})$  may also accumulate in the anode flow field.

#### 6.4.1. In-Plane Distribution of $\text{H}_2\text{O}$

In this section, the use of  $^1\text{H}$  NMR microscopy to study the *in-plane* variation of  $\text{H}_2\text{O}(\text{pem})$  between the catalyst layers of an operating MEA is demonstrated. In particular, the dynamic interaction of cell power output, gas flow rates, and water

content were investigated and visualized experimentally for the first time[3]. Such information has long been sought, but continues to elude other methods currently used for *in-situ* PEMFC diagnosis. The effect of co- versus counter-flow gas configurations on the in-plane distribution of water in the PEM and the flow channels of a PEMFC operating with dry H<sub>2</sub>(g) and dry O<sub>2</sub>(g) was also investigated. In addition, the effects of H<sub>2</sub>O(l) accumulation in the cathode flow field on fuel cell power output are described and the experimental observations are related to predictions from relevant theoretical models.

To initiate our investigations a baseline condition of the PEMFC was first established. We found that a practical method to observe changes in water content and distribution in the operating PEMFC is to begin with no H<sub>2</sub>O(l) in the flow fields and with the MEA at low water content. Using a <sup>1</sup>H NMR microscopy image of a low water content MEA as a reference allows separation of the effects of different water sources on distribution. For example, the growth and distribution of water from humidified gas streams can be observed if no current is drawn through the cell while the gases are flowing. The only source of water, then, would be from the humidified gas. In this study we use dry gas streams to observe the water produced by the reduction of oxygen at the cathode. The following indicates how gas flow rate, cell current, and <sup>1</sup>H NMR microscopy are used together to determine *in-situ* the effects of the amount of water on cell performance.

Prior to operating the PEMFC, the anode flow field was filled with H<sub>2</sub>O(l) to fully hydrate the PEM. After purging H<sub>2</sub>O(l) from the anode, the flow rates of the dry H<sub>2</sub>(g) and O<sub>2</sub>(g) were set to 5.0 and 2.5 mL min<sup>-1</sup>, respectively. The gas inlets/outlets were in the counter-flow configuration shown in Figure 6-3. The power output was set to 24.8 mW cm<sup>-2</sup> (21.0 mA, 0.590 V) to allow the cell to



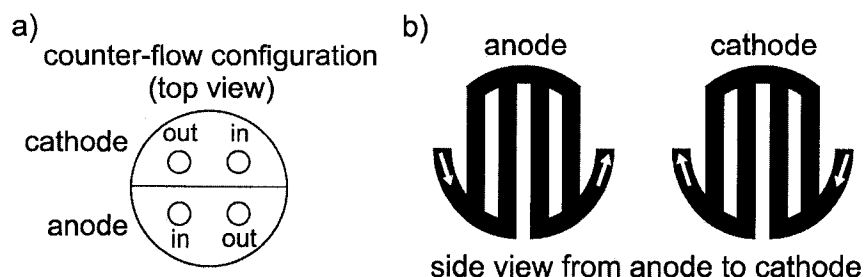


**Figure 6-3.** (a) Representation of the top of the PEMFC showing the gas inlets/outlets in a counter-flow configuration, (b) the direction of gas flow through the cathode and anode flow channels as viewed from the anode side of the PEMFC.

establish a self-determined steady-state of water in the MEA. Shown in Figure 6-4a are  $^1\text{H}$  NMR microscopy images from 500  $\mu\text{m}$  slices containing the MEA and the cathode flow field, acquired from the PEMFC after operating for 35 minutes. During this period, a significant amount of  $\text{H}_2\text{O}(l)$  accumulated in the cathode flow field. The water originated from the fully hydrated PEM and from reduction of oxygen at the cathode. To remove this  $\text{H}_2\text{O}(l)$  we typically operated the PEMFC at a reduced current and increased  $\text{O}_2(g)$  flow rate. In general, flushing  $\text{H}_2\text{O}(l)$  from the cathode flow field was more difficult if the current drawn from the cell was not reduced to decrease the amount of water produced. The current was reduced to 1.8 mA and at  $t = 0$  the  $\text{O}_2(g)$  flow rate was increased from 2.5 to 50  $\text{mL min}^{-1}$ . The  $^1\text{H}$  NMR microscopy images show that by  $t = 5$  min (Figure 6-4b) most of the  $\text{H}_2\text{O}(l)$  was flushed from the cathode flow field, while the difference image indicates that water was not removed from the PEM. The  $\text{H}_2\text{O}(l)$  removed from the cathode flow field resulted in a slight increase in the cell voltage from 0.908 to 0.912 V at 1.8 mA. Once  $\text{H}_2\text{O}(l)$  is removed from the cathode flow field, the time required to remove  $\text{H}_2\text{O}(pem)$  is affected by the current drawn from the cell. Specifically, we found that higher currents typically dehydrate the PEM more rapidly. This effect is due to the increase in water transported through the PEM from the anode to the cathode *via* electro-osmotic drag[8,9]. The water produced at the cathode by reduction of

**Table 6-1.** The corresponding power density, current, and voltage measured from the 30 mm PEMFC for the images shown in Figure 6-4.

Signal Decline Image	Power Density / $\text{mW cm}^{-2}$	Current / mA	Potential / V
a	3.3	1.8	0.908
b	3.3	1.8	0.912
c	31.8	21.6	0.736
d	28.6	20.5	0.698

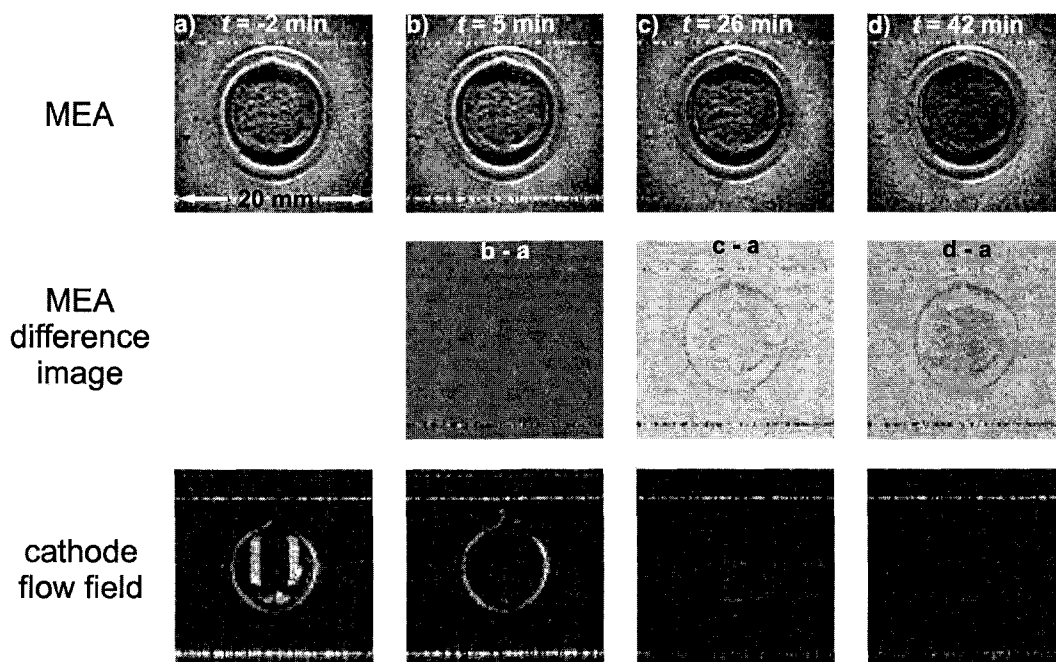


**Figure 6-4.**  $^1\text{H}$  NMR microscopy images of the MEA (top), MEA difference images (middle), and cathode flow field (bottom) obtained from the PEMFC operating on dry  $\text{H}_2(\text{g})$  and  $\text{O}_2(\text{g})$ .  $t = 0$  was when the  $\text{O}_2(\text{g})$  flow rate was increased from 2.5 to 50  $\text{mL min}^{-1}$ . Image acquisition parameters: slice = 500  $\mu\text{m}$ ,  $T_R = 1.0$  s,  $T_E = 3.2$  ms, FOV = 30 mm  $\times$  30 mm ( $h \times v$ ; PE  $\times$  FE), MTX = 128<sup>2</sup>, pixel size = 234  $\mu\text{m} \times$  234  $\mu\text{m}$ , 8 echoes, 1 image, 1 average, experiment time = 128 s.

oxygen cannot replenish the  $\text{H}_2\text{O}(\text{pem})$  because of evaporation into the high flow of  $\text{O}_2(\text{g})$ . For example, after removing most of the  $\text{H}_2\text{O}(\text{l})$  from the cathode flow field, at  $t = 23$  min the external circuit load was changed to increase the cell power output to 29.5  $\text{mW cm}^{-2}$  (20.8 mA, 0.709 V). After a brief improvement in performance due to complete removal of  $\text{H}_2\text{O}(\text{l})$  from the cathode flow field, subsequent dehydration of the PEM resulted in a decrease in the cell power output. The images in Figure 6-

4c, at  $t = 26$  min, show that while there is still some  $\text{H}_2\text{O}(pem)$ , the dark area in the central region of the difference image indicates that the amount of  $\text{H}_2\text{O}(pem)$  remaining is slightly less than the amount at  $t = -2$  min. At high  $\text{O}_2(g)$  flow rates the PEMFC acts as a water pump, humidifying the gas stream with  $\text{H}_2\text{O}(pem)$  and water produced by the reduction of oxygen. Further operation over the following 16 minutes to  $t = 42$  min (Figure 6-4d) dehydrates the PEM to the extent that the cell's performance is affected, causing a decline from  $31.8 \text{ mW cm}^{-2}$  (21.6 mA, 0.736 V) at  $t = 26$  min to  $28.6 \text{ mW cm}^{-2}$  (20.5 mA, 0.698 V).

The use of NMR microscopy in combination with monitoring cell performance demonstrates that a high  $\text{O}_2(g)$  flow rate can quickly remove  $\text{H}_2\text{O}(l)$  from the cathode flow field and initially improves power output. Subsequent dehydration of the PEM and decrease in power output occurs when the MEA is no longer in contact with  $\text{H}_2\text{O}(l)$  in the flow field. As well, for this counter-flow configuration, the difference images indicate that the removal of  $\text{H}_2\text{O}(pem)$  appears uniform in distribution. The images in Figure 6-4b to 6-4d represent a snapshot of the  $\text{H}_2\text{O}(pem)$  in transition to a steady state. Prolonged operation of the PEMFC with a high  $\text{O}_2(g)$  flow rate ultimately dehydrates the PEM such that the performance cannot be recovered without decreasing the gas flow rate and humidifying the gas(es).

The  $^1\text{H}$  NMR microscopy images shown in Figure 6-5 illustrate the recovery of  $\text{H}_2\text{O}(pem)$  by water generated at the cathode of the operating fuel cell and the accumulation of  $\text{H}_2\text{O}(l)$  in the cathode flow field after the  $\text{O}_2(g)$  flow rate is decreased. The images in Figure 6-5a were acquired 3 min prior to decreasing the  $\text{O}_2(g)$  rate from 50 to  $2.5 \text{ mL min}^{-1}$ , and the top image therefore represents a low water content PEM. Reducing the  $\text{O}_2(g)$  flow rate slows the evaporation of water

**Table 6-2.** The corresponding power density, current, and voltage measured from the 30 mm PEMFC for the images shown in Figure 6-5.

Signal Recovery Image	Power Density/ $\text{mW cm}^{-2}$	Current / mA	Potential / V
a	37.7	31.1	0.606
b	42.6	33.1	0.644
c	41.9	32.8	0.638
d	40.3	32.2	0.626

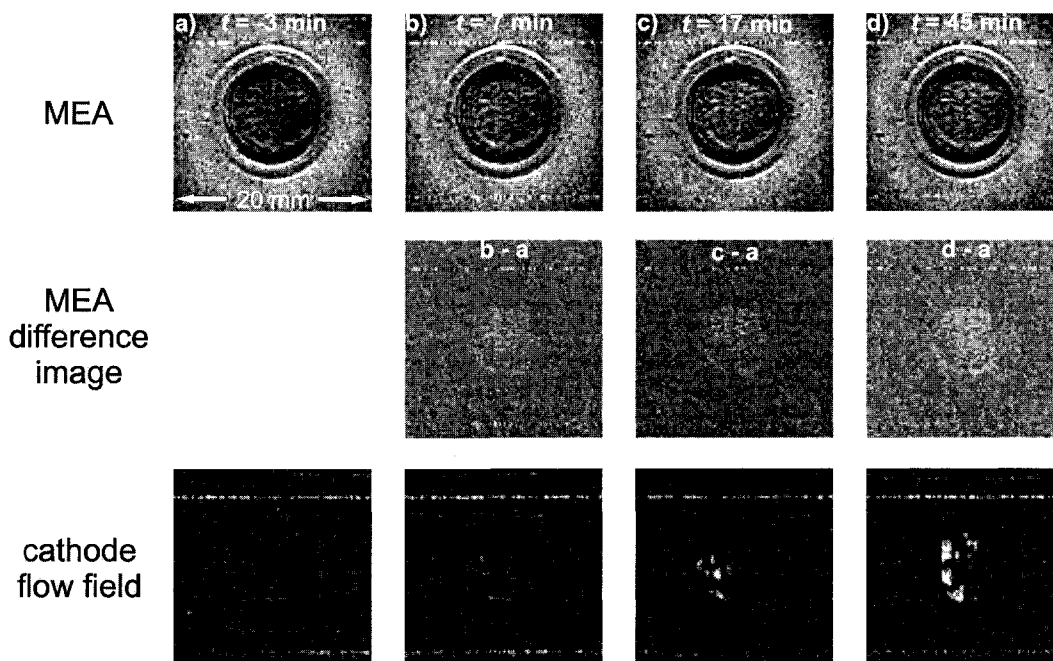


**Figure 6-5.**  $^1\text{H}$  NMR microscopy images of the MEA (top), MEA difference images (middle), and cathode flow field (bottom) obtained from the PEMFC operating on dry  $\text{H}_2(\text{g})$  and  $\text{O}_2(\text{g})$ .  $t = 0$  is when the  $\text{O}_2(\text{g})$  flow rate was *decreased* from 50 to 2.5  $\text{mL min}^{-1}$ . See text for discussion.

from the cathode to enable hydration of the PEM. Beginning with the low initial water content PEM facilitates the observation of this process. Seven minutes after reducing the  $\text{O}_2(\text{g})$  flow rate the amount of  $\text{H}_2\text{O}(\text{pem})$  has increased (Figure 6-5b). This recovery is evident in the MEA image and in the bright area in the central region of the MEA difference image. As  $\text{H}_2\text{O}(\text{l})$  begins to accumulate in the cathode flow field the cell power output peaks at  $42.6 \text{ mW cm}^{-2}$  (33.1 mA, 0.644 V). Figures 6-5c and 6-5d show that the amount of  $\text{H}_2\text{O}(\text{pem})$  continues to increase, but with

sustained  $\text{H}_2\text{O}(l)$  accumulation in the cathode flow field, the cell power output declines. The difference images indicate that the recovery of  $\text{H}_2\text{O}(pem)$  is uniform and that the accumulation of  $\text{H}_2\text{O}(l)$  occurs in the outlet half of the cathode flow field. This demonstrates that the PEMFC is effectively self-humidifying. These experiments illustrate that  $^1\text{H}$  NMR microscopy is an effective *in-situ* diagnostic tool for optimizing fuel cell operating conditions.

As described in Chapter 3, proton transport in Nafion may occur *via* a combination of mechanisms including translational self-diffusion, Grotthuss-type transport, Fickian diffusion, and electro-osmotic transport introduced by the electric-field from anode to cathode. Electro-osmotic proton conduction involves the co-transport of water and, per proton, more molecules of water are transported with increasing PEM water content[8]. The water content, translational self-diffusion rate, and electro-osmotic drag coefficient in Nafion-117 are known to be highest when the PEM is in contact with  $\text{H}_2\text{O}(l)$ [6,7]. An experimental study by Büchi and Srinivasan[1] of a fuel cell operating on dry anode and cathode gases in a counter flow configuration lead them to postulate a model for self-humidification of the gas streams (Figure 6-6). Several theoretical models for water transport in a PEMFC operating on dry reactant gases in a counter-flow arrangement predict similar behavior[10-13]. According to these studies, a water concentration gradient exists across the thickness of the MEA from the cathode to anode because water is only produced at the cathode. This phenomenon was also previously observed with  $^1\text{H}$  NMR microscopy[14,15].

At the anode inlet/cathode outlet side of the cell, the water concentration gradient is largest because the anode gas enters dry and the cathode gas exits humidified by the water produced from the reduction of oxygen. Further, in our cell,  $\text{H}_2\text{O}(l)$  produced at the cathode preferentially accumulates near the  $\text{O}_2(g)$  outlet.

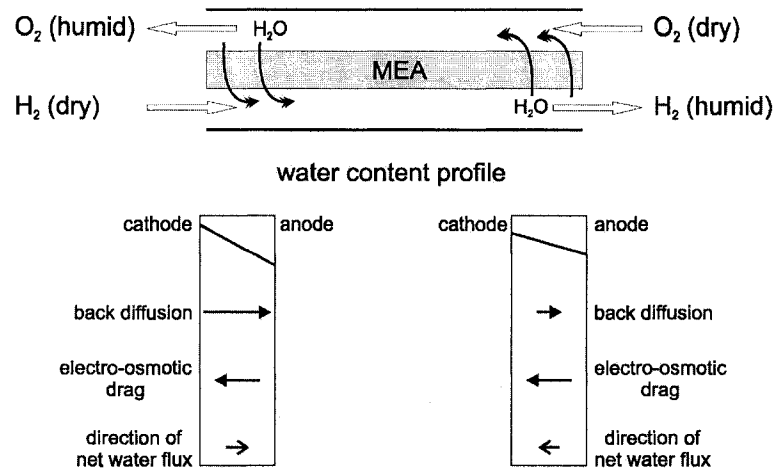


**Figure 6-6.** Schematic of the model postulated by Büchi and Srinivasan[1] for water flux across the MEA in a self-humidifying counter-flow PEMFC. See text for discussion.

In this region the net flux of water across the PEM may be from cathode to anode; the concentration gradient may facilitate sufficient back-diffusion to surmount the water transported from anode to cathode *via* electro-osmotic drag. In addition, the local electro-osmotic drag coefficient may be reduced if catalytic sites are rendered inactive by the accumulation of  $\text{H}_2\text{O}(l)$  in the cathode flow field. Now consider the anode outlet/cathode inlet side of the cell where the anode gas exits humidified and the cathode gas enters dry. In this region the net flux of water is likely from the anode to the cathode. A water concentration gradient across the PEM from cathode to the anode remains, however, the magnitude of the gradient is smaller than at the cathode outlet. Therefore, the amount of water transported by back-diffusion from cathode to anode will be less than the amount of water transported from anode to cathode *via* electro-osmotic drag.

#### 6.4.2. Effect of Gas Flow Direction

The influence of the gas inlet and outlet configuration on the in-plane distribution of  $\text{H}_2\text{O}(pem)$ , on the distribution of  $\text{H}_2\text{O}(l)$  in cathode flow field, and on performance of the cell was also investigated. Starting from an initial dry MEA

condition as described in §6.4.1, the cell was operated with all four of the possible gas inlet/outlet configurations shown in Figure 6-7 (left). The power output was adjusted to allow the amount of  $\text{H}_2\text{O}(pem)$  to reach a constant level and to facilitate accumulation of  $\text{H}_2\text{O}(l)$  in the cathode flow field. For each configuration, images are shown for two series of experiments.

Figures 6-7a and 6-7b show images acquired from the cell operating in the two counter-flow gas configurations. As established by the difference images, the in-plane distribution of  $\text{H}_2\text{O}(pem)$  for both counter-flow configurations is uniform. As discussed above, in the counter-flow configurations the distribution of  $\text{H}_2\text{O}(pem)$  remains relatively uniform because the dry gases enter the cell directly across the MEA from the exiting humidified gases. This relatively uniform distribution of  $\text{H}_2\text{O}(pem)$  imparted by the counter-flow configurations will encourage more homogeneous proton conduction and catalyst activity across the MEA. Now looking at the cathode flow field, for both counter-flow configurations  $\text{H}_2\text{O}(l)$  typically begins to accumulate in the outlet half of the cathode flow field. After operating for several hours at higher currents, or when the cell is operated with the PEM saturated with water immediately before operating the cell,  $\text{H}_2\text{O}(l)$  blockages may also envelop central regions of the flow field.

Figures 6-7c and 6-7d show images acquired from the cell operating in the two co-flow gas configurations. For both co-flow configurations the distribution of  $\text{H}_2\text{O}(pem)$ , indicated by the difference images, is not uniform; the area of the PEM near the gas inlets contains less water than the region of the PEM near the gas outlet, as predicted by several theoretical models (*vide infra*). We propose that the dry gases entering the flow fields in parallel on opposite sides of the MEA will draw water from the same region, and this will dehydrate the PEM at the inlets. We note

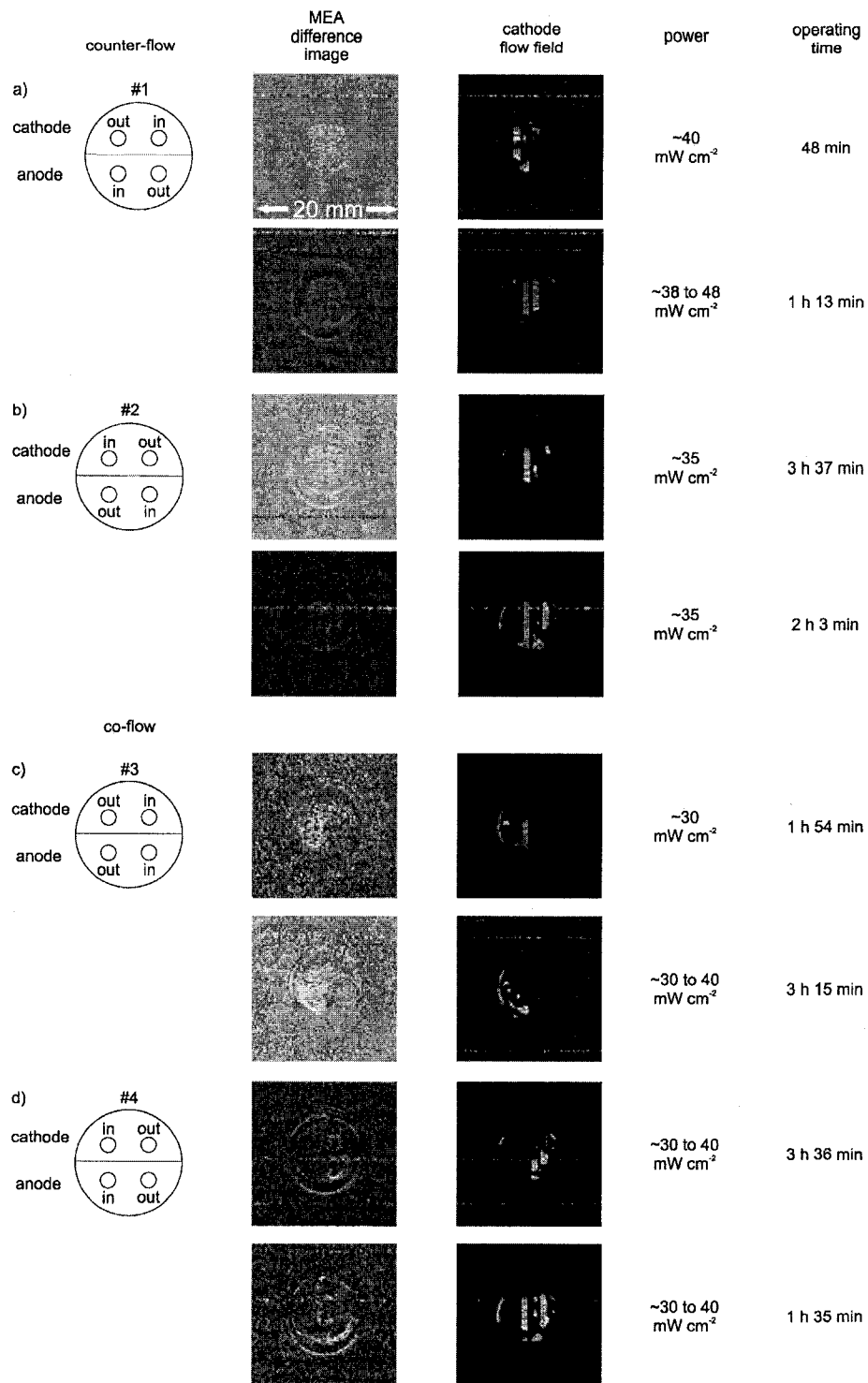


**Figure 6-7.** The four possible gas inlet/outlet configurations (left) and two representative examples of the resulting water distribution for each. The MEA difference images show the distribution of  $H_2O(pem)$  relative to a low water-content PEM. The cathode flow field images show the location of  $H_2O(l)$  accumulation. The approximate power density and operating time of the PEMFC are shown on the right.



that this non-uniform distribution of water from outlet to inlet will cause in-plane diffusion of water from regions of high to low water content. With the co-flow configurations we find that longer operating times and/or increased cell currents are often required to facilitate  $\text{H}_2\text{O}(l)$  accumulation in the cathode flow field. The resistance to proton transport through the PEM is known to increase as the amount of water in the PEM diminishes[16,17]. Therefore, regions of the PEM that contain less water will exhibit reduced proton transport and, as a consequence the catalysts over such a region of the PEM will operate less effectively. In addition, the resulting non-uniform distribution of potentials across the MEA will likely result in an in-plane proton current and an associated parasitic electron shunt current across the catalyst/electrode plane. We postulate that, in the absence of  $\text{H}_2\text{O}(l)$  in the cathode flow field, the distribution of  $\text{H}_2\text{O}(pem)$  represented by the NMR microscopy images indicates the relative activity of the operating catalysts in the MEA. Now considering the cathode flow field, in both co-flow configurations,  $\text{H}_2\text{O}(l)$  typically accumulates only in the outlet region. The second set of images for configuration #4, however, show that the distribution of  $\text{H}_2\text{O}(l)$  in the cathode flow field is more central. In effect, the lower half of the PEM toward the gas inlets is more hydrated in comparison to the same region in the first set of images for this configuration.

The performance of a PEMFC operating in a co-flow gas configuration with dry feed gases is often poor and unstable, and therefore most investigations of co-flow gas configurations typically incorporate humidification of one or both gas feeds. In general, co-flow models predict a low current density in the inlet region of low humidity reactant gases due to the low water content of the membrane in this region[12,13,18-20]. Along the channel from gas inlet to outlet the current densities and water content increase[18-20], but current densities may decrease at the outlet if  $\text{H}_2\text{O}(l)$  is present[12,21]. These results suggest that net water flux across the

membrane is toward the cathode near the inlets and toward the anode near the outlets[18]. A recent model investigating the effect of partial membrane drying predicted that along-the-channel non-uniformity of  $H_2O(pem)$  would generate a parasitic in-plane proton current[22]. Our observations provide the first direct experimental images of the non-uniform in-plane distribution of water in a PEMFC operating in co-flow gas configurations. To summarize various observations from experiment and predictions from theoretical models, the schematic in Figure 6-8 illustrates our postulated flux of water in a dry or low-humidity co-flow PEMFC. Note, however, that in fuel cells with active areas of several  $100\text{ cm}^2$  with long gas flow channels and high flow rates, convective transport inside the channel dominates parallel diffusive fluxes in the GDLs or PEM[20].

Although  $H_2O(l)$  accumulates in the cathode flow field in both co- and counter-flow gas configurations creating a large concentration gradient from cathode to anode, we have not observed  $H_2O(l)$  in the anode flow field when using dry gas feeds. Therefore, in either co- or counter-flow configurations, achieving

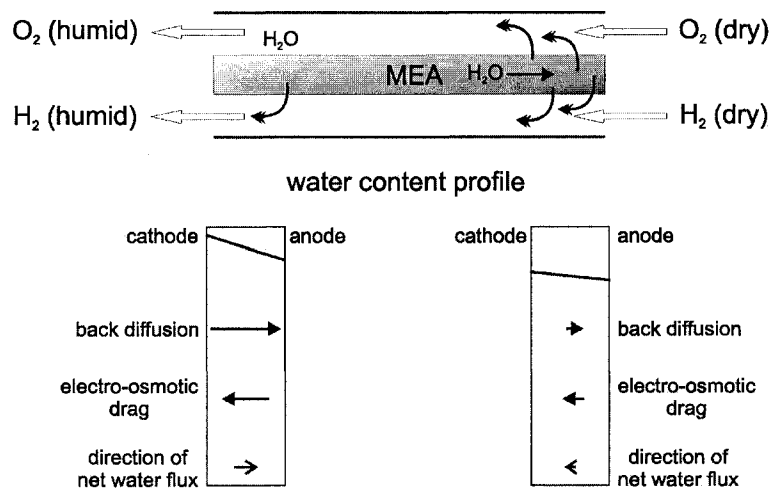


**Figure 6-8.** Schematic of a model for water flux across the MEA in a self-humidifying co-flow PEMFC. The darker shading indicates a region with low water content. See text for discussion.

adequate back-diffusion to fully humidify the  $\text{H}_2(\text{g})$  stream is unlikely. Thus, even at currents below that theoretically required to fully humidify both gas streams (see §4.2.1), cathode flooding may occur.

#### 6.4.3. Effect of $\text{H}_2\text{O}(\text{l})$ Accumulation in the Cathode Flow Field on Performance

The task of maintaining the delicate balance of  $\text{H}_2\text{O}(\text{pem})$  of an operating fuel cell such that ionic conductivity is maximized, while preventing the accumulation of  $\text{H}_2\text{O}(\text{l})$  in the GDL and subsequently the cathode flow field is difficult. We have often noted that the performance of our PEMFC is improved with a small amount of  $\text{H}_2\text{O}(\text{l})$  in the cathode flow field. Thus, for each of the gas inlet and outlet configurations for our PEMFC we investigated the relationship between the onset of  $\text{H}_2\text{O}(\text{l})$  accumulation in the cathode flow field and the power output of the cell operated with a constant external circuit resistance. Figure 6-9 contains representative  $^1\text{H}$  NMR microscopy images of the cathode flow field and PEMFC performance data for each of the four gas-flow configurations. Prior to acquisition of each series of images, a high  $\text{O}_2(\text{g})$  flow rate of  $50 \text{ mL min}^{-1}$  was used to remove  $\text{H}_2\text{O}(\text{l})$  from the cathode flow field and to reduce the amount of  $\text{H}_2\text{O}(\text{pem})$ . The first image in each series was acquired at, or shortly after,  $t = 0$  when the  $\text{O}_2(\text{g})$  flow rate was decreased to  $2.5 \text{ mL min}^{-1}$ . Thus, the water that subsequently hydrates the PEM and accumulates in the cathode flow field is produced by the reduction of oxygen at the cathode. In all gas flow configurations (Figure 6-9a to d) the second NMR microscopy image in each series corresponds to the time at which  $\text{H}_2\text{O}(\text{l})$  is first visible in the cathode flow field. For all configurations, the power output from the cell is highest at this time. The water content in Nafion-117 is known to be higher when in contact with  $\text{H}_2\text{O}(\text{l})$  versus water vapour, and results in a corresponding increase in ionic conductivity[6,7]. Before  $\text{H}_2\text{O}(\text{l})$  is visible in the image of the

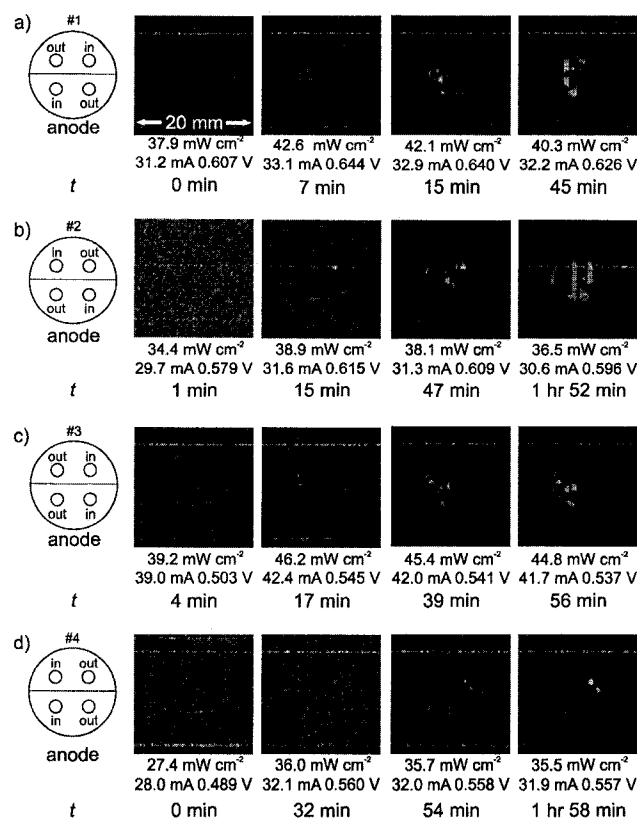


**Figure 6-9.** <sup>1</sup>H NMR microscopy images summarizing the effect of the onset of H<sub>2</sub>O(l) accumulation in the cathode flow field and the subsequent impact of further water build-up on the cell power output. At  $t = 0$  the O<sub>2</sub>(g) flow rate was decreased to 2.5 mL/min. Note that the maximum performance observed for each configuration occurs at the onset of H<sub>2</sub>O(l) accumulation (second image), followed by a slow decline in performance as water continues to build-up in the cathode flow channels.

cathode flow field, flooding of the catalysts and GDL must be occurring. As mentioned earlier, the NMR microscopy methods used herein do not reveal water at the catalyst surface or in the GDLs, however, a novel fluorescence microscopy technique for the *ex-situ* visualization of H<sub>2</sub>O(l) transport in GDLs has recently been developed[23]. As H<sub>2</sub>O(l) continues to build up in the cathode flow field (third and final images), the power output from the cell slowly declines. Only with more severe flooding of the cathode does a substantial decrease in cell performance occur.

A plethora of models have been developed to investigate the impact of gas flow configuration and/or gas humidification on the performance of fuel cells and along-the-channel water distribution (*i.e.*, inlet to outlet)[18,19,21,24-29], including a

number of studies investigating the impact of using both dry anode and dry cathode feed gases[10-13,30]. Variable water content in the PEM, and related properties, are often tied to the amount of water present in the gas along the flow channels. A recent study of water management in PEMFCs by Berg *et al.*[13] noted that capping the membrane water content in their model at a value below that expected for a PEM in contact with  $\text{H}_2\text{O}(l)$  may have contributed to some deviations of their model from experimental data. Few along-the-channel models, however, have incorporated the effects of the presence of  $\text{H}_2\text{O}(l)$  in the catalyst layer, GDL, or flow channels[11,12,18,28]. A two-phase model developed by Pasaogullari and Wang[18] predicted that for low humidity cases the oxygen concentration decreased sharply at the onset of flooding in the GDL; however, at this point the cell also exhibited the highest current density for both of the under-humidified cases. Similarly, Sena *et al.* found that for a PEMFC operating between 298 K and 310 K on dry  $\text{H}_2(g)$  and humidified  $\text{O}_2(g)$  or  $\text{O}_2/\text{N}_2$  mixtures at atmospheric pressure, limiting effects due to oxygen diffusion to the catalyst were minimal. For Nafion-117, water transport through the membrane was found to become a limiting effect at high current densities[31]. Thus, at this juncture, in combination with our observations from experiment, we infer that for a low-humidity PEMFC operating at low current densities any detrimental effect on performance due to minimal accumulation of  $\text{H}_2\text{O}(l)$  at the catalyst layer or GDL is superseded by the improved ionic conductivity of the PEM when in contact with  $\text{H}_2\text{O}(l)$ .

## 6.5. Conclusions

Using  $^1\text{H}$  NMR microscopy, images of the in-plane distribution of water within the PEM of an MEA in an operating PEMFC were revealed for the first time. When the self-humidified PEMFC was operated with a high  $\text{O}_2(g)$  flow rate of 50 mL

min<sup>-1</sup>, the <sup>1</sup>H NMR microscopy images revealed that following removal of H<sub>2</sub>O(*l*) from the cathode flow field, dehydration of the PEM ensued resulting in a decline in the power output of the cell. Subsequent decrease of the O<sub>2</sub>(*g*) flow rate to 2.5 mL min<sup>-1</sup> resulted in an increase in content of water in the PEM, followed by accumulation of H<sub>2</sub>O(*l*) in the cathode flow field. <sup>1</sup>H NMR microscopy was also employed to investigate the influence of co- versus counter-flow gas configurations on the in-plane distribution of water in PEM of the operating PEMFC. The co-flow configurations resulted in dehydration of the PEM at the inlets while the counter-flow configurations effected a more uniform distribution of H<sub>2</sub>O(*pem*). Also, at the onset of H<sub>2</sub>O(*l*) accumulation in the cathode flow field the power output of the cell peaks, while further build up of water results in a decline in power output. These observations are qualitatively in agreement with numerous theoretical fuel cell models.

This study demonstrates the unique ability of <sup>1</sup>H NMR microscopy to investigate *in-situ* the dynamic interplay of power output, gas flow rate, and water content and distribution in an operating PEMFC. Clearly, <sup>1</sup>H NMR microscopy will continue to reveal critical information regarding the distribution of water inside operating PEMFCs and is a powerful tool for diagnosing, understanding, and optimizing the effects of fuel cell materials, components, and designs.

#### 6.6. References

- [1] Büchi, F. N.; Srinivasan, S. *J. Electrochem. Soc.* **1997**, *144*, 2767-2772.
- [2] Feindel, K. W.; LaRocque, L. P. A.; Starke, D.; Bergens, S. H.; Wasylishen, R. E. *J. Am. Chem. Soc.* **2004**, *126*, 11436-11437.
- [3] Feindel, K. W.; Bergens, S. H.; Wasylishen, R. E. *J. Am. Chem. Soc.* **2006**, *128*, 14192-14199.

- [4] Callaghan, P. T. *Principles of Nuclear Magnetic Resonance Microscopy*; Oxford University Press: New York, 1991.
- [5] Callaghan, P. T. In *Encyclopedia of Nuclear Magnetic Resonance*; Harris, R. K., Ed.; John Wiley and Sons, Inc.: Chichester, 1996; Vol. 7, 4665-4671.
- [6] Zawodzinski, T. A., Jr.; Derouin, C.; Radzinski, S.; Sherman, R. J.; Smith, V. T.; Springer, T. E.; Gottesfeld, S. J. *Electrochem. Soc.* **1993**, *140*, 1041-1047.
- [7] Zawodzinski, T. A., Jr.; Neeman, M.; Sillerud, L. O.; Gottesfeld, S. J. *Phys. Chem.* **1991**, *95*, 6040-6044.
- [8] Ise, M.; Kreuer, K. D.; Maier, J. *Solid State Ionics* **1999**, *125*, 213-223.
- [9] Kraemer, E. O.; Williams, J. W.; Albery, R. A. In *A Treatise on Physical Chemistry*; 3rd ed.; Taylor, H. S., Glasstone, S., Eds.; D. Van Nostrand Company, Inc.: New York, 1951; Vol. 2.
- [10] Hsing, I. M.; Futerko, P. *Chem. Eng. Sci.* **2000**, *55*, 4209-4218.
- [11] Janssen, G. J. M. *J. Electrochem. Soc.* **2001**, *148*, A1313-A1323.
- [12] Ge, S. H.; Yi, B. L. *J. Power Sources* **2003**, *124*, 1-11.
- [13] Berg, P.; Promislow, K.; St Pierre, J.; Stumper, J.; Wetton, B. J. *Electrochem. Soc.* **2004**, *151*, A341-A353.
- [14] Teranishi, K.; Tsushima, S.; Hirai, S. *J. Electrochem. Soc.* **2006**, *153*, A664-A668.
- [15] Tsushima, S.; Teranishi, K.; Hirai, S. *Electrochem. Solid-State Lett.* **2004**, *7*, A269-A272.
- [16] Siu, A.; Schmeisser, J.; Holdcroft, S. *J. Phys. Chem. B* **2006**, *110*, 6072-6080.
- [17] Zawodzinski, T. A., Jr.; Springer, T. E.; Davey, J.; Jestel, R.; Lopez, C.; Valerio, J.; Gottesfeld, S. J. *Electrochem. Soc.* **1993**, *140*, 1981-1985.
- [18] Pasaogullari, U.; Wang, C. Y. *J. Electrochem. Soc.* **2005**, *152*, A380-A390.
- [19] Fuller, T. F.; Newman, J. J. *Electrochem. Soc.* **1993**, *140*, 1218-1225.

- [20] Freunberger, S. A.; Santis, M.; Schneider, I. A.; Wokaun, A.; Büchi, F. N. *J. Electrochem. Soc.* **2006**, *153*, A396-A405.
- [21] Dutta, S.; Shimpalee, S.; Van Zee, J. W. *J. Appl. Electrochem.* **2000**, *30*, 135-146.
- [22] Kulikovskiy, A. A. *Electrochim. Acta* **2004**, *49*, 5187-5196.
- [23] Litster, S.; Sinton, D.; Djilali, N. *J. Power Sources* **2006**, *154*, 95-105.
- [24] Bernardi, D. M.; Verbrugge, M. W. *J. Electrochem. Soc.* **1992**, *139*, 2477-2491.
- [25] Nguyen, T. V.; White, R. E. *J. Electrochem. Soc.* **1993**, *140*, 2178-2186.
- [26] Yi, J. S.; Nguyen, T. V. *J. Electrochem. Soc.* **1998**, *145*, 1149-1159.
- [27] Futerko, P.; Hsing, I. M. *Electrochim. Acta* **2000**, *45*, 1741-1751.
- [28] You, L. X.; Liu, H. T. *Int. J. Heat Mass Tran.* **2002**, *45*, 2277-2287.
- [29] Cao, J.; Djilali, N. *J. Energ. Resour-ASME* **2005**, *127*, 26-36.
- [30] Chan, S. H.; Goh, S. K.; Jiang, S. P. *Electrochim. Acta* **2003**, *48*, 1905-1919.
- [31] Sena, D. R.; Ticianelli, E. A.; Paganin, V. A.; Gonzalez, E. R. *J. Electroanal. Chem.* **1999**, *477*, 164-170.



## Chapter 7. Use of Hydrogen-Deuterium Exchange to Introduce Image

### Contrast

#### 7.1. Introduction

Variations in the amount or distribution of water in the PEM of an operating PEMFC may be subtle. For example, if the PEMFC is operated with a constant current output and constant gas flow rates, there may be little change in the water content of the PEM. Thus, obtaining information about the redistribution of water in a PEMFC operating under steady-state conditions or when the PEM is fully hydrated may be difficult using  $^1\text{H}$  NMR microscopy. The use of  $\text{H}_2\text{O}$ - $\text{D}_2\text{O}$  exchange was found to introduce contrast in  $^1\text{H}$  NMR microscopy images and facilitate the study of water exchange in the roots of a maize seedling[1]. Similarly, Ilvonen *et al.* studied water flow velocity and distribution in wood xylem using  $\text{H}_2\text{O}$ - $\text{D}_2\text{O}$  exchange[2].  $^1\text{H}$  NMR microscopy was also used recently to investigate the mutual diffusion of  $\text{H}_2\text{O}$  and  $\text{D}_2\text{O}$  in a Nafion ball[3].

In this chapter, the information that may be obtained by using H-D exchange to modify the contrast in  $^1\text{H}$  NMR microscopy images of an operating PEMFC was investigated. The methods employed reduce the  $^1\text{H}$  NMR signal by using either  $\text{D}_2\text{O}(l)$  or  $\text{D}_2(g)$  to achieve H-D exchange with water in the PEM. Subsequently, the PEMFC was operated with  $\text{H}_2(g)$  and the recovery of the  $^1\text{H}$  NMR signal was monitored.

#### 7.2. Experimental Details

Pre-purified  $\text{H}_2(g)$  (99.995%) or  $\text{D}_2(g)$  (99.70%) and industrial grade  $\text{O}_2(g)$  (99.0%) were supplied at ambient pressure to the 30 mm PEMFC from compressed gas cylinders *via* flow meters. All gases were obtained from Praxair.  $\text{D}_2\text{O}(l)$  (99.9%) was obtained from Cambridge Isotopes or General Intermediates of Canada. Dry gases were used, and unless otherwise stated, the  $\text{H}_2(g)$  or  $\text{D}_2(g)$  flow rate was 5 mL

$\text{min}^{-1}$  and  $\text{O}_2(\text{g})$  flow rate was  $2.5 \text{ mL min}^{-1}$ . Typical operating currents and voltages of the PEMFC were shown by the polarization curve in Figure 4-6. For this study the PEMFC was operated at external resistances that, in the absence of flooding of the catalyst by water, resulted in power densities ranging from approximately 15 to  $50 \text{ mW cm}^{-2}$ . Prior to cycling  $\text{D}_2\text{O}(\text{l})$  through either the cathode or anode with a syringe pump, any  $\text{H}_2\text{O}(\text{l})$  accumulated in the cathode flow channels was purged using a  $\text{O}_2(\text{g})$  flow rate of  $50 \text{ mL min}^{-1}$ . A flow of  $\text{N}_2(\text{g})$  (99.93 %) was used to remove any  $\text{H}_2(\text{g})$  from the anode gas lines and flow channels before  $\text{D}_2\text{O}(\text{l})$  was cycled through the anode flow channels.  $\text{D}_2\text{O}(\text{l})$  exiting the PEMFC was collected in a container flushed with  $\text{O}_2(\text{g})$  for subsequent reuse.

A typical slice-selective spin-echo imaging sequence[4] was used to obtain images from a  $30 \text{ mm} \times 30 \text{ mm}$  field of view. Five slices of thickness  $500 \mu\text{m}$  were oriented such that the entire PEM and most of each GDL were contained within the central slice and the anode and cathode flow fields contained in the neighbouring slices. The FE direction was parallel with the plane of the MEA and  $B_0$ . 128 FE and 128 PE steps were used, yielding an in-plane pixel size of  $234 \mu\text{m} \times 234 \mu\text{m}$ . In all experiments, the receiver BW was 101010.1 Hz, the time between  $^1\text{H}$  NMR signal excitation and acquisition of the first echo,  $T_E$ , was 3.2 ms, and in total eight echoes were co-added after each excitation. The length of the RF excitation pulse was 1.0 ms with a BW of 6 kHz and a flip angle,  $\alpha$ , of  $90^\circ$ . The repeat time between successive  $^1\text{H}$  NMR signal excitations,  $T_R$ , was 1.0 s, resulting in a total time of 128 s per experiment.

### 7.3. Contrast Introduced *via* Use of $\text{D}_2\text{O}(\text{l})$

The configuration of the gas inlets/outlets is shown in Figure 7-1a and in Figure 7-1b the direction of gas flow in the anode and cathode flow fields for this

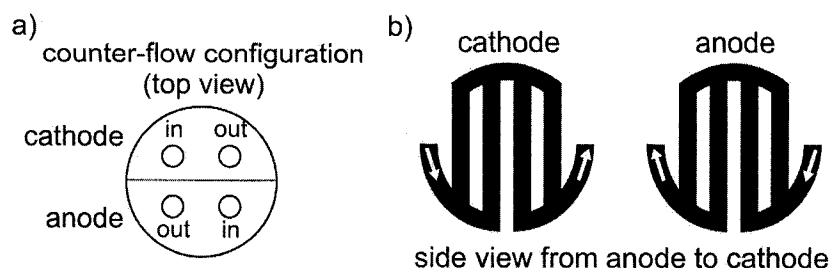


**Figure 7-1.** (a) Representation of the top of the PEMFC showing the gas inlets/outlets in a counter-flow configuration, (b) the direction of gas flow through the cathode and anode flow channels as viewed from the anode side of the PEMFC.

counter-flow configuration are indicated relative to the perspective of the images herein, *i.e.*, viewed from the anode side of the PEMFC. Figure 7-2a shows a  $^1\text{H}$  NMR microscopy image from a  $500\ \mu\text{m}$  thick slice containing the MEA, acquired after operating the PEMFC on dry  $\text{H}_2(\text{g})$  and dry  $\text{O}_2(\text{g})$  for  $\sim 4\ \text{h}$  at  $\sim 14\ \text{mW cm}^{-2}$  (11 mA, 0.63 V, electrode area  $\sim 0.5\ \text{cm}^2$ ) and four minutes prior to pumping  $\text{D}_2\text{O}(\text{l})$  into the cell (*i.e.*,  $t = -4\ \text{min}$ ). This image represents a steady-state amount and distribution of water in the PEM (Nafion-117) which was determined by the gas flow and the water produced from the reduction of oxygen at the cathode. At  $t = 0$  the circuit with the

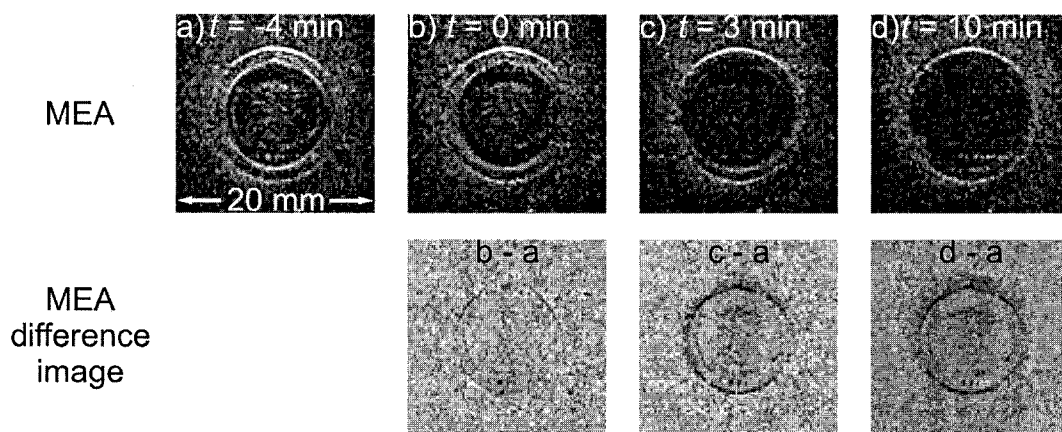


**Figure 7-2.**  $^1\text{H}$  NMR microscopy images from a  $500\ \mu\text{m}$  slice containing the MEA (top) and MEA difference images (bottom) acquired from the PEMFC (a) while operating on dry  $\text{H}_2(\text{g})$  and  $\text{O}_2(\text{g})$  four minutes prior to pumping  $\text{D}_2\text{O}(\text{l})$  in the cell, (b) and (c) when  $\text{D}_2\text{O}(\text{l})$  was cycled through the cathode flow field starting at  $t = 0$ , and (d) after the  $\text{D}_2\text{O}(\text{l})$  was purged from the PEMFC with  $\text{O}_2(\text{g})$ . The MEA difference images show the decline in  $^1\text{H}$  NMR signal.

external resistance was disconnected (*i.e.*,  $I = 0$  mA). The  $\text{H}_2(\text{g})$  and  $\text{O}_2(\text{g})$  flows were stopped and  $\text{D}_2\text{O}(\text{l})$  was pumped into the cathode flow field. The images in Figure 7-2b to d show the decline of the  $^1\text{H}$  NMR signal as  $\text{D}_2\text{O}$  replaces  $\text{H}_2\text{O}$  in the PEM. Changes in image contrast occur in areas of the PEM that contain  $\text{H}_2\text{O}$ ; a dry PEM will show no change in  $^1\text{H}$  NMR signal upon hydration with  $\text{D}_2\text{O}(\text{l})$ . Each MEA difference image shows the loss of  $^1\text{H}$  NMR signal relative to the image in Figure 7-2a. The  $^1\text{H}$  NMR signal decreases rapidly in the MEA region within the O-ring, such that by  $t = 3$  min there is little signal remaining. When no further reduction in the  $^1\text{H}$  NMR signal from the MEA region was noticeable, the  $\text{D}_2\text{O}(\text{l})$  was purged from the cathode flow channels with  $\text{O}_2(\text{g})$  at a flow rate of  $50 \text{ mL min}^{-1}$  and the image in Figure 7-2d was acquired.

After being in contact with  $\text{D}_2\text{O}(\text{l})$  the PEM is expected to be completely hydrated. Shown in Figure 7-3a is an image acquired after purging the  $\text{D}_2\text{O}(\text{l})$  from the cathode and three minutes prior to starting the  $\text{H}_2(\text{g})$  flow or drawing a current

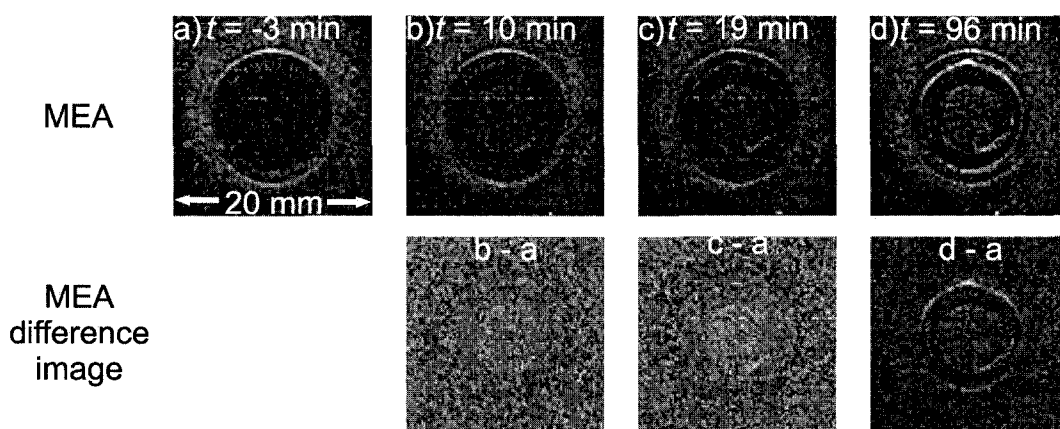


**Figure 7-3.**  $^1\text{H}$  NMR microscopy images from a  $500 \mu\text{m}$  slice containing the MEA (left) and MEA difference images (right) acquired from the PEMFC (a) after purging  $\text{D}_2\text{O}(\text{l})$  from the cathode flow field with  $\text{O}_2(\text{g})$ , and (b) to (d) after operating on dry  $\text{H}_2(\text{g})$  and  $\text{O}_2(\text{g})$  for the indicated time. At  $t = 0$  the  $\text{H}_2(\text{g})$  flow was started and current was drawn from the PEMFC. The MEA difference images show the increase in  $^1\text{H}$  NMR signal as  $\text{H}_2\text{O}$  replaces  $\text{D}_2\text{O}$  in the PEM upon operating the cell with  $\text{H}_2(\text{g})$  as fuel and a faint dark ring from  $\text{D}_2\text{O}$  diffusing away from the MEA.

from the PEMFC. This image represents a high water (D<sub>2</sub>O) content, but low <sup>1</sup>H density PEM. At  $t = 0$  the H<sub>2</sub>(g) and O<sub>2</sub>(g) flow rates were set to 5.0 and 2.5 mL min<sup>-1</sup>, respectively. The external resistive circuit was reconnected and the PEMFC power output adjusted to ~25 mW cm<sup>-2</sup> (19.5 mA, 0.623 V). The power output of 25 mW cm<sup>-2</sup> indicated that the cathode flow field was flushed sufficiently with O<sub>2</sub>(g) to remove D<sub>2</sub>O(l) from the GDL and the surface of the catalysts. Often, after cycling H<sub>2</sub>O(l) or D<sub>2</sub>O(l) through the flow channels only a low power output was attainable (*e.g.*, < 5 mW cm<sup>-2</sup>). The expected performance was not achieved until high gas flow rates of 25 to 50 mL min<sup>-1</sup> were used, which likely removed excess H<sub>2</sub>O(l) from the GDL and catalysts. After operating the cell with H<sub>2</sub>(g) as fuel for 10 min (Figure 7-3b), the recovery of the <sup>1</sup>H NMR signal was evident in the central region of both the image of the MEA and the difference image. The <sup>1</sup>H NMR signal continued to strengthen, and after operating for ~90 min there was a relatively uniform distribution of water in the PEM of the MEA and water is evident along the Au-ring. The difference images in Figure 7-3b to d also reveal a faint ring-shaped region beyond the MEA. This darker region indicates that D<sub>2</sub>O is being transported from the MEA region into the surrounding PEM. Diffusion radially outward from the MEA was also observed during fuel-cell start-up with a dry membrane (§6.3)[5].

The H-D exchange in the D<sub>2</sub>O-saturated PEM is expected to be facilitated by operating the PEMFC, as H<sub>2</sub>(g) is oxidized at the anode and protons are transported through the PEM to the cathode. Several reactions describe the exchange process:



The rate constant at 28 °C for proton exchange in pure H<sub>2</sub>O(l) is  $7.1 \pm 0.4 \times 10^9 \text{ L mol}^{-1} \text{ s}^{-1}$  and for deuteron exchange in D<sub>2</sub>O(l) is  $4.3 \pm 0.5 \times 10^9 \text{ L mol}^{-1} \text{ s}^{-1}$ [6]. The mean

lifetime of a water molecule in solution is related to pH, and for acidic environments the mean lifetime (in seconds) can be approximated by the relation  $10^{\text{pH}-9.85}$ [6]. Acid-form Nafion is a very strong Brønsted acid, with strength comparable to that of  $\text{CF}_3\text{SO}_3\text{H}$ [7]. Thus, H-D exchange in water saturated Nafion will be fast on the NMR timescale (*i.e.*,  $< \mu\text{s}$ ). If current is not drawn from the cell, H-D exchange with water in the PEM will only occur *via* contact of the gas at the surface of the PEM or by permeation of  $\text{H}_2(\text{g})$  into the PEM. The permeability of fully humidified  $\text{H}_2(\text{g})$  through Nafion-117 at 273 K is  $\sim 8.5 \times 10^{-10} \text{ mol m}^{-1} \text{ s}^{-1}$ [8], whereas the rate of proton consumption for a current of 20 mA is  $\sim 2.1 \times 10^{-7} \text{ mol s}^{-1}$ . Therefore, flowing  $\text{H}_2(\text{g})$  through the anode flow channels without drawing a current from the PEMFC is not expected to lead to significant exchange.

As described in §3.1.1, water transport in Nafion can occur *via* translational self-diffusion, Fickian diffusion, and in an operating PEMFC *via* electro-osmotic drag. After cycling  $\text{D}_2\text{O}(\text{l})$  through the flow channels the MEA should be near maximal hydration; however, the PEM surrounding the MEA may not be saturated. Thus, the diffusion of  $\text{D}_2\text{O}$  outward from the MEA will occur *via* a combination of mechanisms. The diffusion coefficient for  $\text{H}_2\text{O}$  in Nafion-117 ( $\sim 36 \text{ wt}\%$ ,  $\lambda = 22$ ) at 298 K is  $\sim 7.4 \times 10^{-10} \text{ m}^2 \text{ s}^{-1}$  [9]. A preliminary  $^1\text{H}$  NMR microscopy investigation of a ball of Nafion saturated with  $\text{H}_2\text{O}$  and subsequently placed in  $\text{D}_2\text{O}(\text{l})$  determined a  $\text{H}_2\text{O}$ - $\text{D}_2\text{O}$  mutual diffusion coefficient in Nafion of  $2.5 \times 10^{-10} \text{ m}^2 \text{ s}^{-1}$  [3]. For comparison, at 298 K the self-diffusion coefficients of  $\text{H}_2\text{O}(\text{l})$ , 50 mol %  $\text{H}_2\text{O}$ - $\text{D}_2\text{O}(\text{l})$ , and  $\text{D}_2\text{O}(\text{l})$  are  $23.0 \pm 0.2 \times 10^{-10} \text{ m}^2 \text{ s}^{-1}$ [10],  $20.29 \pm 0.04 \times 10^{-10} \text{ m}^2 \text{ s}^{-1}$ , and  $18.72 \pm 0.04 \times 10^{-10} \text{ m}^2 \text{ s}^{-1}$ [11,12]. Assuming that the diffusion coefficients of  $\text{D}_2\text{O}$  and  $\text{H}_2\text{O}$  in Nafion-117 scale as for the pure liquids, an estimation of the upper limit for the diffusion coefficient of  $\text{D}_2\text{O}$  in Nafion-117 is  $\sim 6 \times 10^{-10} \text{ m}^2 \text{ s}^{-1}$ . The mean square displacement,

$\langle r^2 \rangle^{1/2}$ , of a particle with diffusion coefficient,  $D$ , after a time,  $t$ , can be treated as a random walk process[13], where in one dimension  $\langle r^2 \rangle^{1/2} = (2Dt)^{1/2}$ . The maximum rate of linear displacement of  $D_2O$  due to diffusion in Nafion-117 is then calculated to be  $\sim 1.2 \mu\text{m s}^{-1}$  or  $\sim 4.3 \text{ mm h}^{-1}$ . As a result, H-D exchange in the PEM beyond the region in contact with  $D_2O(l)$  (*i.e.*, outside the O-rings) is expected to be on the order of hours. The dark ring visible in the MEA difference image shown in Figure 7-3d extends approximately 7 mm beyond the O-rings,  $\sim 100$  min after  $D_2O(l)$  was cycled through the cathode flow field.

A summary of the influence of co- and counter-flow gas configurations on exchange-contrast introduced using  $D_2O(l)$  and the subsequent operation of the PEMFC on  $H_2(g)$  is illustrated in Figure 7-4. The corresponding approximate power output and operating time of the PEMFC are provided in Table 7-1. The MEA difference images were obtained as described in §7.3 for Figures 7-2 and 7-3. The signal loss images indicate regions where  $H_2O$  in the PEM was replaced with  $D_2O$ . The H-D exchange that occurred when the PEMFC was subsequently operated with  $H_2(g)$  as fuel is shown in the signal recovery images.

The dark regions in the signal loss images for the two counter-flow configurations (Figure 7-4a and b) are relatively uniform. This indicates that operating the PEMFC with counter-flow gas configurations distributes water throughout the PEM between the catalyst layers in the MEA, and is consistent with the  $^1\text{H}$  NMR microscopy results presented in Chapter 6[14]. In co-flow configuration #3 (Figure 7-4c), the loss of the  $^1\text{H}$  NMR signal occurred predominantly at the gas outlets and indicates that the water content of the PEM was low in the region near the gas inlets. Prior to cycling  $D_2O(l)$  through the cathode, the cell was operated for  $\sim 20$  h with a power output of  $\sim 30 \text{ mW cm}^{-2}$  and

**Table 7-1.** The time that the PEMFC operated on  $H_2(g)$  at the indicated power density prior to acquiring the image of the MEA used in the calculation of the signal recovery image shown in Figure 7-4.

Signal Recovery Image	Operating Time	Power Density / $mW\ cm^{-2}$
a	22 h 4 min	~32-30
b	1 h 39 min	~25
c	55 min	~9-35
d	1 h 29 min	~4-31

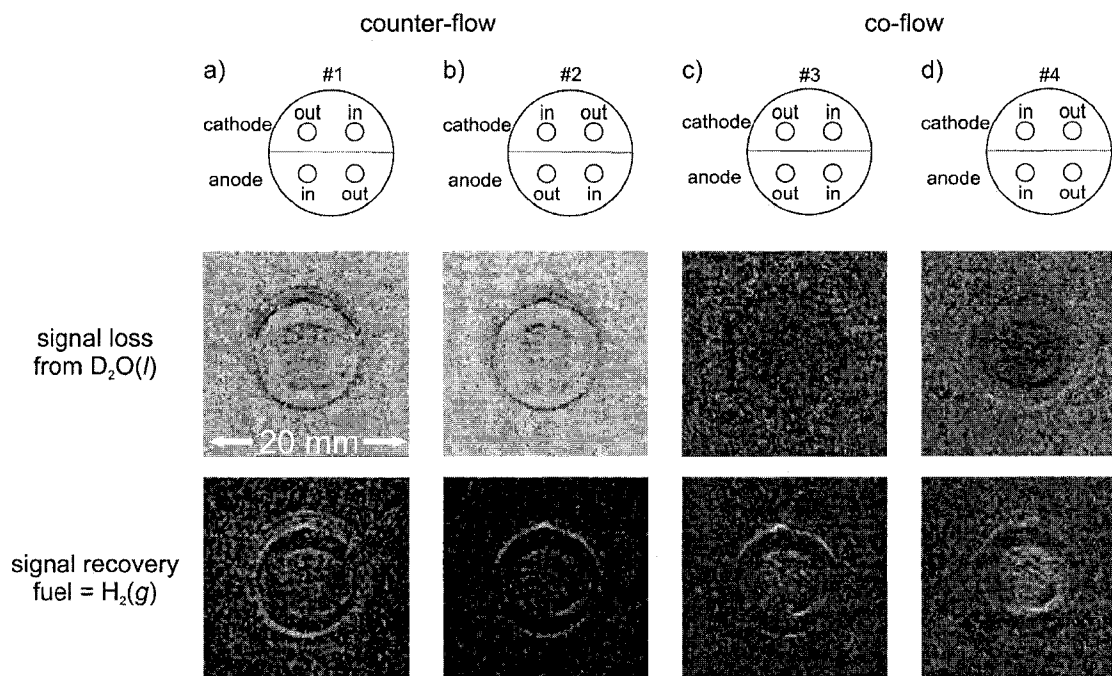


**Figure 7-4.** Representation of the top of the PEMFC indicating the gas inlet/outlet configurations (top), MEA difference image showing the decline in  $^1H$  NMR signal in the PEM caused by cycling  $D_2O(l)$  through either the cathode or anode flow field (middle), and MEA difference imaging showing the increase in  $^1H$  NMR signal in the PEM upon operating the PEMFC on dry  $H_2(g)$  as fuel (bottom).

had not been flooded with  $H_2O(l)$  or  $D_2O(l)$  for several days. The content and distribution of water in the PEM, as determined by the gas-flow configuration and power output, is expected to have reached a steady-state and have higher water content in the PEM near the gas outlets[14]. In contrast, for co-flow configuration #4 the loss of  $^1H$  signal was more uniform across the MEA in comparison to that



observed for configuration #3. Prior to operating the PEMFC in configuration #4 at  $\sim 4$  to  $31 \text{ mW cm}^{-2}$  for 90 min,  $\text{D}_2\text{O}(l)$  was cycled through the cathode flow field. The resulting water content of the PEM was sufficiently high to compensate for water removed by the dry gases entering the flow channels. The uniform distribution of water observed for configuration #4 also indicates that the amount of water in the PEM had not reached a steady-state after operating for 90 min.

Saturating the MEA with  $\text{D}_2\text{O}(l)$  and then operating the PEMFC with  $\text{H}_2(g)$  as fuel results in H-D exchange with water in the PEM. The exchange occurs uniformly across the plane of the MEA for all gas flow configurations as shown by the signal recovery images in Figure 7-4. This, in conjunction with the uniform loss of signal for configuration #4, indicates that for co-flow configurations saturation of the MEA with liquid water can postpone dehydration of the PEM at the gas inlets.

#### 7.4. Contrast Introduced by Alternating between $\text{H}_2(g)$ and $\text{D}_2(g)$ as Fuel

Changes in the distribution of water in the MEA of an operating PEMFC can be monitored in  $^1\text{H}$  NMR microscopy images by comparing images of low and high water content PEMs (§6.3, 6.4) [5,14], and by using  $\text{D}_2\text{O}(l)$  to introduce image contrast in saturated PEMs (§7.3). Due to the relatively constant water content and distribution in the PEM of a fuel cell operating at steady state, investigating the variation of water within the PEM using proton density images is difficult. Here we demonstrate that contrast can be introduced into the  $^1\text{H}$  NMR microscopy images of an operating PEMFC by alternately fuelling the PEMFC with  $\text{H}_2(g)$  and  $\text{D}_2(g)$ .

Shown in Figure 7-5a is a  $^1\text{H}$  NMR microscopy image acquired after the PEMFC operated on  $\text{H}_2(g)$  and  $\text{O}_2(g)$  in counter-flow configuration #1 (see Figure 7-4a) with a power output of  $\sim 30 \text{ mW cm}^{-2}$  for 7 h. The PEM was well hydrated and a small amount of  $\text{H}_2\text{O}(l)$  was in the cathode flow field. At  $t = 0$  the circuit with the variable resistor was disconnected (*i.e.*,  $I = 0 \text{ mA}$ ) while the fuel was switched from

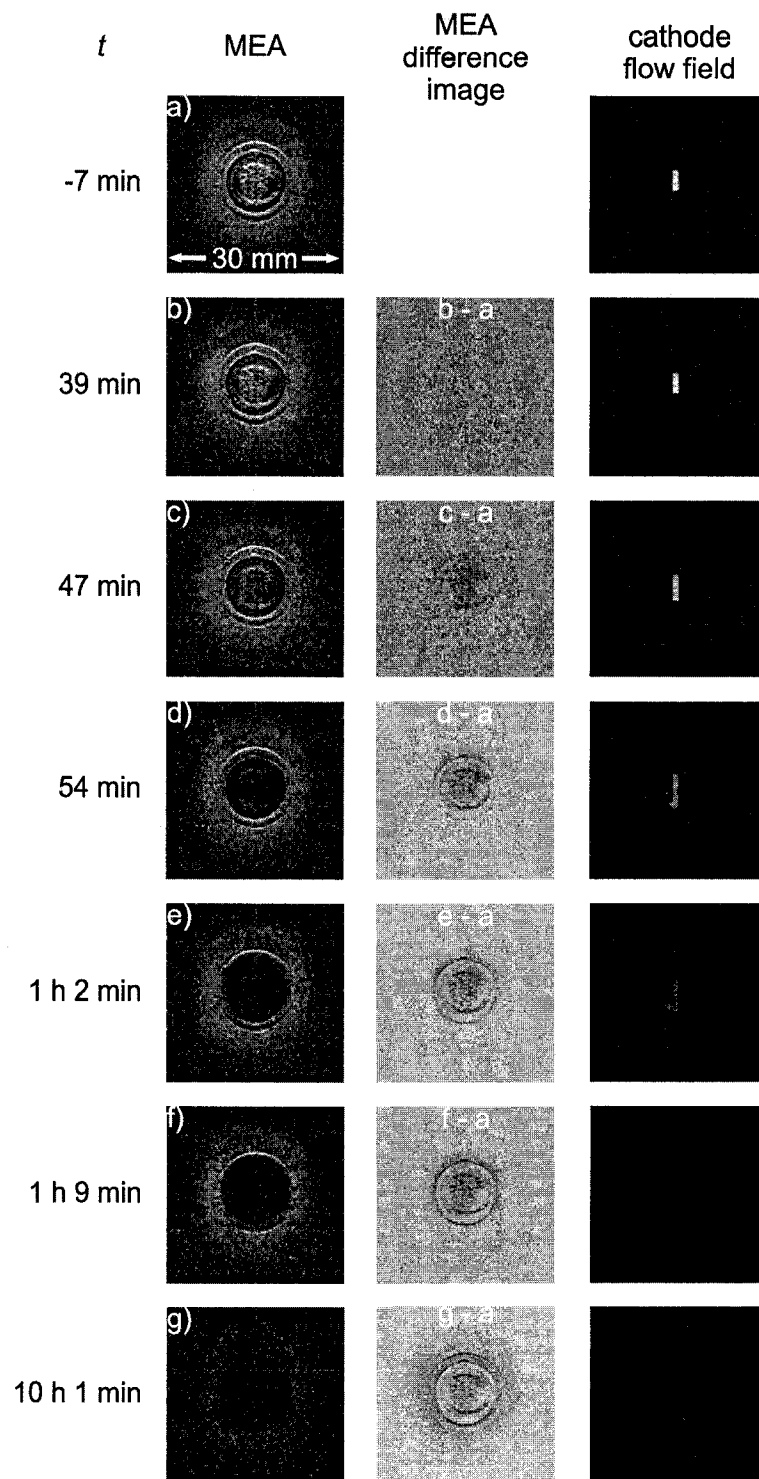


**Figure 7-5.**  $^1\text{H}$  NMR microscopy images from  $500\ \mu\text{m}$  slices containing the MEA (left), the cathode flow field (right), and the MEA difference images (centre) showing the decrease in  $^1\text{H}$  NMR signal while operating the PEMFC on  $\text{D}_2(\text{g})$  as fuel with a power output of  $\sim 30\ \text{mW cm}^{-2}$  (22 mA, 0.67 V). At  $t = 0$ , the fuel was switched from  $\text{H}_2(\text{g})$  to  $\text{D}_2(\text{g})$ .

$\text{H}_2(\text{g})$  to  $\text{D}_2(\text{g})$ . When the circuit was reconnected, the cell power output was the same as measured when using  $\text{H}_2(\text{g})$  as fuel. If either the reaction at the anode catalyst or the H-D exchange with water in the Nafion was the rate-determining step for the overall PEMFC processes, one would expect a change in the cell power output due to an isotope effect. The exchange current density for electrochemical reactions is analogous to the rate constant in chemical reactions. For a Pt catalyst at 25 °C, and 1 atm, the exchange current densities for the anode and cathode of a  $\text{H}_2/\text{O}_2$  PEMFC are  $\sim 10^{-4}$  and  $\sim 10^{-9}$  A  $\text{cm}^{-2}$ , respectively[15]. As a result, the reduction of oxygen at the cathode is much slower than hydrogen oxidation at the anode, and is the rate-determining step. In theory, the open circuit voltage of a  $\text{D}_2/\text{O}_2$  PEMFC should be marginally higher than for a  $\text{H}_2/\text{O}_2$  PEMFC since the Gibb's free energy of formation,  $\Delta G_f^\circ$ , for  $\text{D}_2\text{O}(\text{l})$  is  $\sim 5$  kJ  $\text{mol}^{-1}$  larger than for  $\text{H}_2\text{O}(\text{l})$ . Both the adsorption energy on metal surfaces and the dissociation energy of  $\text{D}_2(\text{g})$  are higher than for  $\text{H}_2(\text{g})$  because of the lower zero-point energy for the deuterium-containing species. There are reports of a four-fold decrease in power output when using a low partial pressure (0.7 kPa) of  $\text{D}_2(\text{g})$  versus  $\text{H}_2(\text{g})$ [16,17]. The effect was attributed to proton-tunnelling between adjacent sulfonate groups at the surface of the PEM and becomes less important with increasing partial pressure of  $\text{D}_2(\text{g})$ [16,17].

After using  $\text{D}_2(\text{g})$  as fuel for 39 min (Figure 7-5b), the difference image shows a faint indication that the  $^1\text{H}$  NMR signal in the MEA is starting to decline. The amount of water in the cathode flow field increased as the H-D exchange was more apparent (Figures 7-5c to e), and after 1 h 9 min little  $^1\text{H}$  NMR signal remained in the MEA or in the flow field. Although the water accumulated in the cathode flow field was no longer visible in the images, no unusual fluctuations in power output were observed that would suggest removal of the water from the flow field[14]. After

operating the PEMFC with  $D_2(g)$  for a period of 10 h a significant decline of the  $^1H$  NMR signal was evident outside of the MEA in the surrounding PEM (Figure 7-5g).

When operating with  $D_2(g)$  as fuel, significant loss of the  $^1H$  NMR signal in the MEA or cathode flow field does not appear to occur during the first 40 min. In the following 30 min, however, the  $^1H$  NMR signal in both the MEA and cathode flow field disappears. Due to the known dependence of water transport properties in Nafion on water content, H-D exchange in the PEM is likely affected by the amount and distribution of water in the PEM, as well as other factors such as the volume of the MEA and the surrounding PEM, and the rate of  $D_2(g)$  consumption. Operating the PEMFC with a current of 23.5 mA uses approximately  $1.22 \times 10^{-7}$  mol  $s^{-1}$  of  $D_2(g)$  and produce the same amount of water at the cathode. As shown in the images in Figure 7-5b, the  $2.9 \times 10^{-4}$  mol of  $D_2(g)$  consumed and  $\sim 5.3 \mu L$  of water produced over 40 minutes does not appear to affect the  $^1H$  NMR signal. However, in the following 30 min the exchange within the MEA and in the water accumulated in the cathode flow field appears complete. The origin of this observation is not clear. Upon switching to  $D_2(g)$  as fuel, initially  $H_2(g)$  will be adsorbed on the surface of the GDL and the catalyst, and the PEM will contain  $H_2O$  and  $H_3O^+$ . A delay may be introduced as the adsorbed  $H_2$  is oxidized prior to adsorption of  $D_2(g)$  by the catalyst. Upon oxidation of  $D_2(g)$ , H-D exchange will occur with  $H_2O$  in the PEM to form HOD and eventually  $D_2O$ . As H-D exchange occurs, water in the PEM may diffuse away from the MEA due to a concentration gradient, be transported *via* intradiffusion, or through the PEM to the cathode *via* electro-osmotic drag. Each of these processes will expand the volume over which H-D exchange occurs. In theory, if the rates of the water transport processes were known, the amount of

water contained in the PEM could be calculated from the rate of fuel consumption and the period of time required for complete exchange to occur.

The images in Figure 7-6 show the recovery of the  $^1\text{H}$  NMR signal due to H-D exchange after the fuel was switched from  $\text{D}_2(\text{g})$  to  $\text{H}_2(\text{g})$ . Prior to acquiring the images in Figure 7-6a the PEMFC was operated using  $\text{D}_2(\text{g})$  as fuel with a power output of  $\sim 30 \text{ mW cm}^{-2}$  (23.5 mA, 0.70 V) for  $\sim 3$  h in counter-flow configuration #1 (see Figure 7-4a). Approximately 1 h after operating with  $\text{H}_2(\text{g})$  as fuel and a power output of  $\sim 30 \text{ mW cm}^{-2}$ , the  $^1\text{H}$  NMR signal in the MEA and the cathode flow field was evident (Figure 7-6b). As shown in Figure 7-6c and d the intensity of the  $^1\text{H}$  NMR signal continued to increase over a period of 2 h.

When the fuel was switched from  $\text{H}_2(\text{g})$  to  $\text{D}_2(\text{g})$ , or *vice versa*, there was a significant delay before change in the  $^1\text{H}$  NMR signal was observed. The decline in

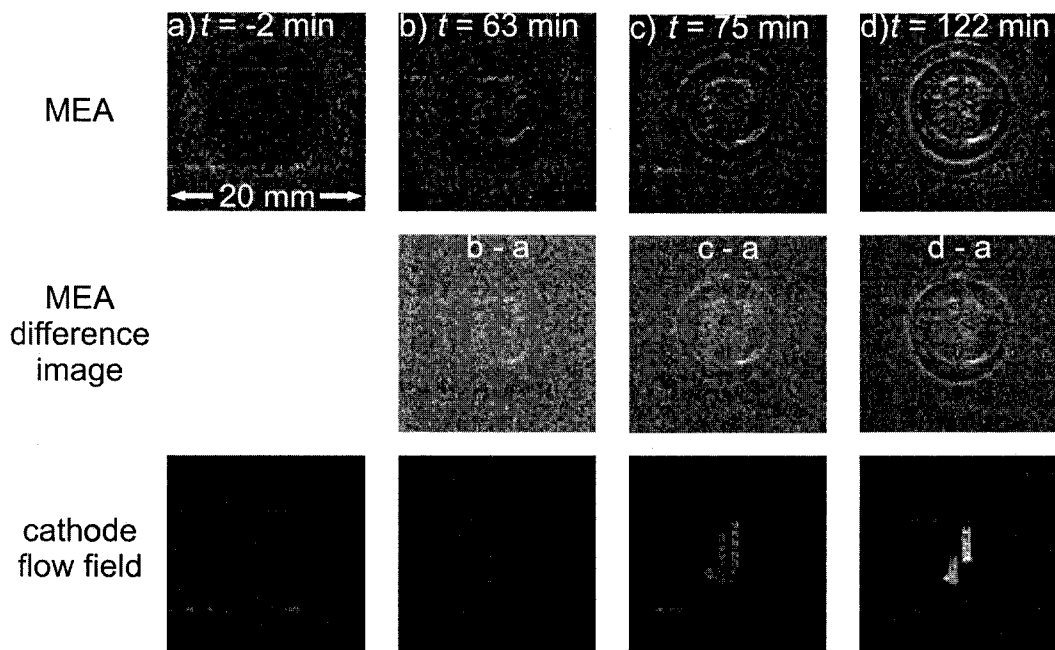


**Figure 7-6.**  $^1\text{H}$  NMR microscopy images from  $500 \mu\text{m}$  slices containing the MEA (top), the cathode flow field (bottom), and the MEA difference images (middle) showing the increase in  $^1\text{H}$  NMR signal while operating the PEMFC on  $\text{H}_2(\text{g})$  as fuel with a power output of  $\sim 30 \text{ mW cm}^{-2}$  (23 mA, 0.65 V). At  $t = 0$ , the fuel was switched from  $\text{D}_2(\text{g})$  to  $\text{H}_2(\text{g})$ .

signal was apparent after 40 min (Figure 7-5b), whereas the recovery of the signal was not apparent for 60 min (Figure 7-6b). This result was reproducible over repeated experiments. If the time required for H-D exchange to occur for water in Nafion is limited by the H-D exchange rates for water, one would expect the exchange from D<sub>2</sub>O to H<sub>2</sub>O to take longer due to larger O-D bond strength. This observation warrants further investigation.

The influence of co- and counter-flow gas configurations on the exchange-contrast introduced in the <sup>1</sup>H NMR microscopy images of the PEM by alternating between D<sub>2</sub>(g) and H<sub>2</sub>(g) as fuel was also investigated. In Figure 7-7 two MEA difference images are shown for each configuration. The first image shows the decline of the <sup>1</sup>H NMR signal when the fuel was switched from H<sub>2</sub>(g) to D<sub>2</sub>(g), and the second image shows the recovery of the signal when H<sub>2</sub>(g) was subsequently used as fuel. In the counter-flow configurations, #1 and #2, the H-D exchange in the PEM was relatively uniform in the plane of the MEA. This indicates a uniform in-plane distribution of water in the PEM and facilitates effective use of most of the catalyst decal. The images in Figure 7-7c and d show the non-uniform in-plane distribution of water in the PEM that results when the cell operates in the co-flow configurations. In both co-flow configurations there was little variation in the image contrast in the region near the gas inlets, and indicates that the PEM in this region contains little water. As a result, the conductivity of the PEM will vary across the plane of the MEA from gas inlet to outlet. In addition, only the region of the catalyst stamp near the gas outlets, where the water content and proton conductivity are higher, will be used effectively. The variation in the distribution of water in the PEM for the co- versus counter-flow gas configurations observed using H-D exchange is consistent with the results reported when starting the PEMFC with low water content PEM[14].

**Table 7-2.** The time that the PEMFC operated on  $D_2(g)$  or  $H_2(g)$  at the indicated power prior to acquiring the image of the MEA used in the calculation of the signal loss or signal recovery images shown in Figure 7-7.

Signal Loss Image	Operating time	Power Density / $mW\ cm^{-2}$
a	10 h 3 min	~32-30
b	1 h 7 min	~32
c	2 h 3 min	~25-31
d	1 h 23 min	~25-30
Signal Recovery Image		
a	1 h 23 min	~32-30
b	1 h 44 min	~34-32
c	1 h 32 min	~32-29
d	1 h 26 min	~31-29

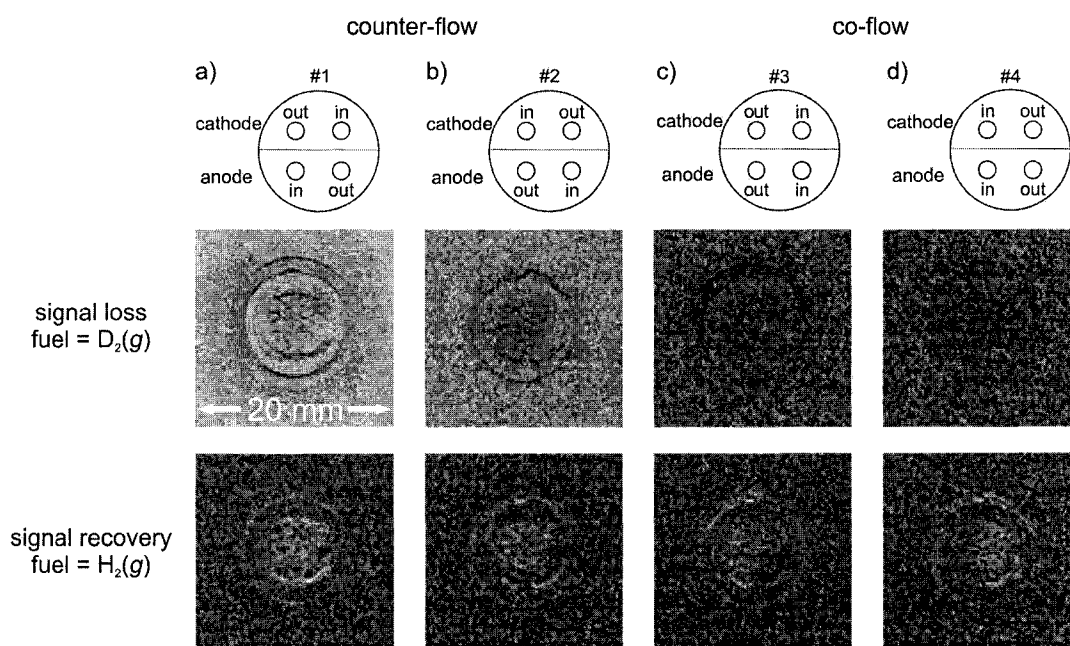


**Figure 7-7.** Representation of the top of the PEMFC indicating the gas inlet/outlet configurations (top), MEA difference images showing the decline in the  $^1H$  NMR signal in the PEM when using  $D_2(g)$  as fuel (middle), and MEA difference images showing the subsequent increase in the  $^1H$  NMR signal when using  $H_2(g)$  as fuel (bottom).

## 7.5. Conclusions

The results presented in this chapter demonstrate that H-D exchange can be used effectively to introduce contrast related to water distribution in  $^1H$  NMR microscopy images of an operating PEMFC. After operating the PEMFC on  $H_2(g)$ ,

cycling  $D_2O(l)$  through the cathode or anode flow channels rapidly removed the  $^1H$  NMR signal within the O-rings and revealed where  $H_2O$  was contained. Subsequent operation of the PEMFC with  $H_2(g)$  as fuel facilitated the investigation of changes in water content when operating the PEMFC with a fully hydrated PEM. After saturating the MEA with water,  $^1H$  NMR microscopy images of the operating PEMFC show that the in-plane distribution of water in the Nafion remains uniform for a period of time (on the order of hours) regardless of gas-flow configuration. Alternating the fuel supply between  $H_2(g)$  and  $D_2(g)$  introduced contrast that enabled investigation of changes in the water in the PEM when the PEMFC operates under steady-state conditions. While operating under such conditions, the H-D exchange contrast shows that counter-flow gas configurations impart a more uniform in-plane distribution of water in the PEM between the catalyst layers than the co-flow gas configurations.

These results demonstrate that H-D exchange is effective in introducing contrast in  $^1H$  NMR microscopy images of operating PEMFCs. The images obtained provide insight to the *in-situ* distribution of water in the PEM between the operating catalyst layers, information that is not available from other fuel cell diagnostic techniques.

#### 7.6. References

- [1] Connelly, A.; Lohman, J. A. B.; Loughman, B. C.; Quiquampoix, H.; Ratcliffe, R. G. *J. Exp. Bot.* **1987**, *38*, 1713-1723.
- [2] Ilvonen, K.; Palva, L.; Perämäki, M.; Joensuu, R.; Sepponen, R. *J. Magn. Reson.* **2001**, *149*, 36-44.
- [3] Kawamura, J.; Hattori, K.; Hongo, T.; Asayama, R.; Kuwata, N.; Hattori, T.; Mizusaki, J. *Solid State Ionics* **2005**, *176*, 2451-2456.



- [4] Callaghan, P. T. *Principles of Nuclear Magnetic Resonance Microscopy*; Oxford University Press: New York, 1991.
- [5] Feindel, K. W.; LaRocque, L. P. A.; Starke, D.; Bergens, S. H.; Wasylshen, R. E. *J. Am. Chem. Soc.* **2004**, *126*, 11436-11437.
- [6] Halle, B.; Karlström, G. *J. Chem. Soc., Faraday Trans. 2* **1983**, *79*, 1031-1046.
- [7] Sondheimer, S. J.; Bunce, N. J.; Lemke, M. E.; Fyfe, C. A. *Macromolecules* **1986**, *19*, 339-343.
- [8] Broka, K.; Ekdunge, P. *J. Appl. Electrochem.* **1997**, *27*, 117-123.
- [9] Zawodzinski, T. A., Jr.; Neeman, M.; Sillerud, L. O.; Gottesfeld, S. *J. Phys. Chem.* **1991**, *95*, 6040-6044.
- [10] Harris, K. R.; Woolf, L. A. *J. Chem. Soc., Faraday Trans. 1* **1980**, *76*, 377-385.
- [11] Mills, R. *J. Phys. Chem.* **1973**, *77*, 685-688.
- [12] Weingärtner, H. *Z. Phys. Chem.* **1982**, *132*, 129-149.
- [13] Crank, J. *The Mathematics of Diffusion*; Clarendon Press: Oxford, 1956.
- [14] Feindel, K. W.; Bergens, S. H.; Wasylshen, R. E. *J. Am. Chem. Soc.* **2006**, *128*, 14192-14199.
- [15] Barbir, F. In *PEM Fuel Cells: Theory and Practice*; Elsevier Academic Press: San Diego, 2005, 33-72.
- [16] Tsampas, M. N.; Pikos, A.; Brosda, S.; Katsaounis, A.; Vayenas, C. G. *Electrochim. Acta* **2006**, *51*, 2743-2755.
- [17] Katsaounis, A.; Balomenou, S.; Tsiplakides, D.; Brosda, S.; Neophytides, S.; Vayenas, C. G. *Appl. Catal. B: Environ.* **2005**, *56*, 251-258.

## Chapter 8. PEMFC Performance and Integral of $^1\text{H}$ NMR Microscopy Image Intensity

### 8.1. Introduction

The ionic conductivity of Nafion is related directly to the amount of water absorbed by the PEM[1-5], and the amount of water in the PEM is related to pre-treatment[2,4,6], humidity[1,2], and temperature[7]. In addition, in an operating PEMFC, the current through the cell, gas humidification, and gas flow rates affect the amount and distribution of water[8]. In an attempt to maintain optimal MEA water content in operating fuel cell stacks, complex programs are often used to control the gas flow rates and relative humidity, and to periodically purge accumulated  $\text{H}_2\text{O}(l)$ [9]. As mentioned previously, theoretical models are an important tool for fuel cell design and development[10,11]. Models are often used to predict fuel cell performance under varying conditions and to help reduce the number of prototypes built en-route to the defined performance objectives. However, detailed experimental data are required to validate models that are simplified, based on assumptions that often include isotropic membrane hydration[10,12].

The use of neutron-based experimental techniques to investigate water in operating PEMFCs was first introduced in 1996 by Mosdale *et al.*[13] who used small-angle neutron scattering to study the water profile across the PEM. Over the past decade numerous investigations have appeared using neutron imaging to measure water content and distribution in operating PEMFCs[14-22]. Recently neutron imaging has been combined with locally resolved impedance spectroscopy[23,24] in an effort to better determine the in-plane water content of the PEM[18]. Prior to the application of  $^1\text{H}$  NMR microscopy to study operating PEMFCs, no available experimental technique could monitor water in the PEM

between the operating catalyst layers separate from other regions of the cell.  $^1\text{H}$  NMR microscopy is suitable for observing the qualitative distribution of water in operating PEMFCs and is useful for investigating the impact of gas flow rate and configuration, and power output on the in-plane distribution of water (Chapters 6 and 7)[25-27].

The objectives of the research presented in this chapter are to investigate how the integrated intensity of the  $^1\text{H}$  NMR microscopy images acquired from an operating PEMFC change with variations in gas flow rate and the power output of the cell, and to evaluate the feasibility of obtaining the absolute water content in the PEM between the catalyst layers from  $^1\text{H}$  NMR microscopy images. In theory, the integrated intensity of the  $^1\text{H}$  NMR microscopy images is directly proportional to the  $^1\text{H}$  spin-density which, in the operating PEMFC, arises almost exclusively from water. This research demonstrates that  $^1\text{H}$  NMR microscopy is a valuable technique to elucidate important information regarding the interdependence of PEMFC water content, gas flow rates and configuration, and PEMFC performance.

## 8.2. Experimental Details

Pre-purified  $\text{H}_2(\text{g})$  (99.995%) and industrial grade  $\text{O}_2(\text{g})$  (99.0%) were supplied at ambient pressure to the 30 mm PEMFC from compressed gas cylinders *via* flow meters. All gases were obtained from Praxair. Dry gases were used, and unless otherwise stated, the  $\text{H}_2(\text{g})$  flow rate was  $5 \text{ mL min}^{-1}$  and  $\text{O}_2(\text{g})$  flow rate was  $2.5 \text{ mL min}^{-1}$ . Typical operating currents and voltages of the PEMFC are shown by the polarization curve in Figure 4-6. For this study the PEMFC was operated with external resistances that, in the absence of flooding of the catalyst by water, result in power densities that ranged from approximately  $15$  to  $50 \text{ mW cm}^{-2}$ .

A typical slice-selective SE imaging sequence[28] was used to obtain images from a  $30 \text{ mm} \times 30 \text{ mm}$  FOV. Five slices of thickness  $500 \mu\text{m}$  were oriented such that

the entire PEM and most of each GDL were contained within the central slice, and the anode and cathode flow fields were contained in the neighbouring slices. The FE direction was parallel with the plane of the MEA and  $B_0$ . 128 FE and 128 PE steps were used, yielding an in-plane pixel size of  $234 \mu\text{m} \times 234 \mu\text{m}$ . In all experiments, the receiver BW was 101010.1 Hz, the time between  $^1\text{H}$  NMR signal excitation and acquisition of the first echo,  $T_E$ , was 3.2 ms, and eight echoes were co-added after each excitation. The length of the RF excitation pulse was 1.0 ms with a BW of 6 kHz and a flip angle,  $\alpha$ , of  $90^\circ$ . The repeat time between successive  $^1\text{H}$  NMR signal excitations,  $T_R$ , was 1.0 s, resulting in a total time of 128 s per experiment.

### 8.3. Correlation Between PEMFC Performance and Image Intensity Integral

#### 8.3.1. The Region of Interest and Influence of Gas Flow Configuration

The catalyst decal of a MEA is often surrounded by superfluous PEM, and as shown in §6.3, when starting the PEMFC with a low water content MEA, water from a humidified gas stream and water produced at the cathode diffuses into the PEM surrounding the catalyst decal[25]. However, the PEM between the operating catalyst layers should reflect more rapidly, changes in water content due to variations in PEMFC operating conditions. The results presented in Chapter 6 demonstrate that the intensity of the  $^1\text{H}$  NMR microscopy images, and therefore the amount of water, in the region of the MEA is related to the PEMFC power output. To investigate further this correlation, the intensity of the  $^1\text{H}$  NMR signal in the region of the MEA was integrated and compared to the performance of the PEMFC.

Shown in Figure 8-1a is a photograph of the O-ring, Au ring, and flow field of the 30 mm PEMFC. A  $^1\text{H}$  NMR microscopy image acquired from a  $500 \mu\text{m}$  slice containing the MEA with the location of the O-ring and MEA indicated is shown in Figure 8-1b. The area of the catalyst decal is  $\sim 0.5 \text{ cm}^2$  and encompasses the area within the Au ring. The amount of water in the PEM between the operating catalyst

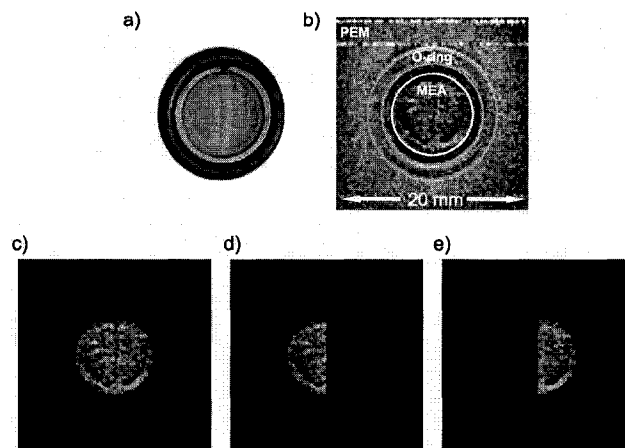


**Figure 8-1.** a) Photograph of the O-ring, Au ring, and flow field of the 30 mm PEMFC, b)  $^1\text{H}$  NMR microscopy image acquired from a 500  $\mu\text{m}$  slice containing the MEA, c) ROI containing the region within the Au ring/MEA as indicated in b, d and e) ROIs containing the left and right halves of the MEA, respectively. See Table 8-1 for ROI areas and  $^1\text{H}$  NMR signal intensity integrals.

**Table 8-1.** The area and integrated  $^1\text{H}$  NMR signal intensity for each of the three ROI shown in Figure 8-1c to e.

Image	Area (pu)	Area ( $\text{cm}^2$ )	Integrated Intensity (a.u.) <sup>a</sup>
c	904	0.497	47461
d	452	0.248	22691
e	452	0.248	24769

a) The signal intensities for the pixels in the ROI shown in Figure 8-1c ranged from 2929 to 279451, with mean value = 95575 and standard deviation = 53361. The source integral is the product of the ROI area and the mean value of the pixel intensities for the defined region.

layers and the performance of the cell is expected to be interdependent. In this area of the PEM, ionic conductivity has the highest influence on cell performance. For example, an increase in PEM conductivity will result in higher currents and production of more water at the cathode, which will lead to more water in the PEM thereby further increasing the conductivity. We previously showed that  $^1\text{H}$  NMR microscopy uniquely provides images of the water in the PEM in situ between the operating catalyst layers (see Chapters 6 and 7)[25,26]. Therefore, the defined region of interest, ROI, from which to integrate the  $^1\text{H}$  NMR microscopy signal was restricted to the MEA area, containing the PEM between the operating catalyst

layers,  $\text{PEM}_{\text{cat}}$ . Shown in Figure 8-1c is a ROI that encompasses the MEA to approximately the inner edge of the Au ring. The area of the ROI is 904 pixel units, pu, or  $0.497 \text{ cm}^2$ , and the areas of the left and right halves of the ROI (Figure 8-1d and e) are 452 pu, or  $0.248 \text{ cm}^2$ . Rapid relaxation of the  $^1\text{H}$  NMR signal in the carbon GDL prevents observation of water in this region (see Chapter 5)[26,27]. Therefore, water observed in these ROI only resides in the region of the PEM between the operating catalyst layers[26]. Typically  $\text{H}_2\text{O}(l)$  water in the GDLs is observed using PEMFCs constructed with transparent materials[29], and recently a novel fluorescence technique was reported for the ex situ visualization of  $\text{H}_2\text{O}(l)$  transport in GDLs[30]. Table 8-1 contains the integrated signal intensities of the three ROIs, which are proportional to water content. Another ROI of the same area as that in Figure 8-1c was used to integrate the intensity of images acquired from slices containing the cathode flow field. The reported integral for a ROI is the product of the ROI area in  $\text{cm}^2$  and the mean value of the  $^1\text{H}$  NMR signal intensity from each pixel for the defined region.

In Chapters 6 and 7 the direction of gas flow was shown to affect the in-plane distribution of water in the PEM between the catalyst layers[26]. Figure 8-2 shows the ROIs in images acquired from the PEMFC operating in each of the four possible gas flow configurations. The integrated  $^1\text{H}$  NMR signal intensities from the full ROI containing  $\text{PEM}_{\text{cat}}$  and the left and right halves are provided in Table 8-2. The integrated  $^1\text{H}$  NMR signal intensities are larger for the counter-flow configurations than for the co-flow configurations showing that counter-flow configurations maintain a greater amount of  $\text{H}_2\text{O}$  in  $\text{PEM}_{\text{cat}}$  than the co-flow configurations. Considering the two halves of the ROI, the signal intensity is similar for the counter-flow configurations but significantly lower at the inlets for co-flow configurations. In the co-flow configurations, the dry gases entering the flow channels draw water

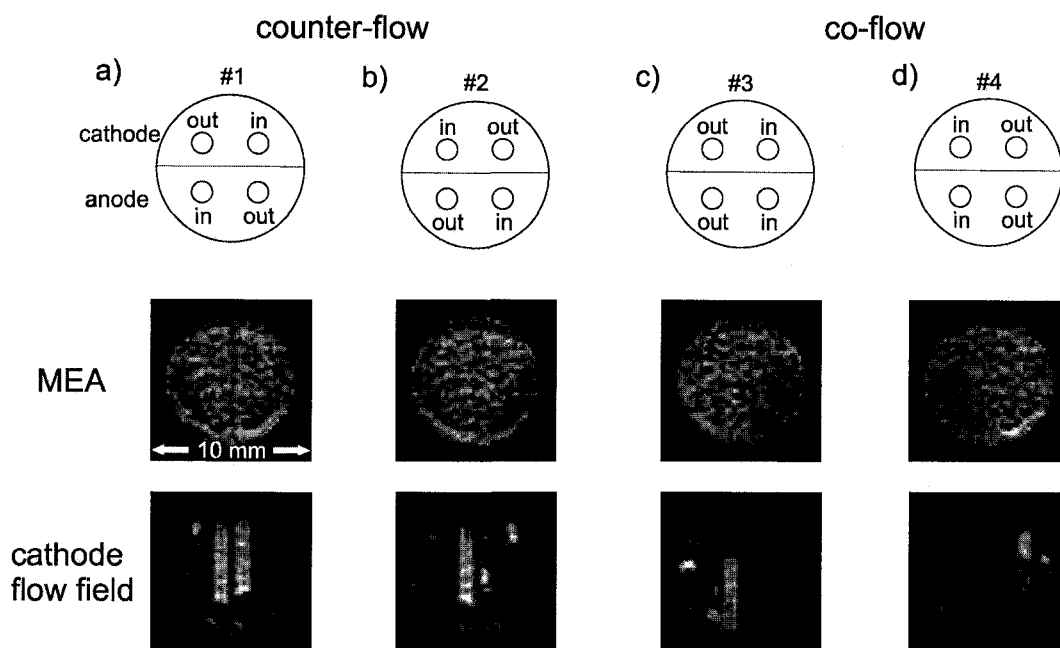


**Figure 8-2.** The four possible gas flow configurations for the 30 mm PEMFC and the ROI in images acquired from a 500  $\mu\text{m}$  slice containing the MEA and the cathode flow field of the operating PEMFC. The corresponding integrated signal intensity values for the three MEA ROIs as shown in Figure 8-1c to e are provided in Table 8-2.

**Table 8-2.** The integrated  $^1\text{H}$  NMR signal intensity values corresponding to the images shown in Figure 8-2 for the ROIs as defined in Figure 8-1c to e.

Image	Configuration	Integrated Intensity from ROI (a.u.)		
		MEA	Left Half MEA	Right Half MEA
a	#1	47461	22691	24769
b	#2	47751	24221	23530
c	#3	44092	24968	19125
d	#4	41365	15622	26743

from the same region of the MEA, dehydrating the PEM at the gas inlets. Further details are provided in Chapter 6[26].

For both counter-flow configurations the total  $^1\text{H}$  NMR signal integrals are essentially equal. The PEMFC was operated at  $\sim 38$  to  $48 \text{ mW cm}^{-2}$  ( $\sim 38$  to  $43 \text{ mA}$ ,  $0.50$  to  $0.56 \text{ V}$ ) for 73 min in configuration #1 (Figure 8-2a) and at  $\sim 35 \text{ mW cm}^{-2}$  ( $\sim 28.5 \text{ mA}$ ,  $0.61 \text{ V}$ ) for 217 min in #2 (Figure 8-2b). The half of the MEA at the anode

inlet/cathode outlet has lower signal intensity, less water, than the anode outlet/cathode inlet. These experiments were completed with the  $\text{H}_2(\text{g})$  flow rate double that of the  $\text{O}_2(\text{g})$ , and as shown in §4.2.1 twice the amount of water per unit time is then required to fully humidify  $\text{H}_2(\text{g})$ ; therefore, water in the MEA at the anode will more rapidly be depleted than at the cathode. However, diffusion of water from the cathode to the anode will help prevent dehydration of the PEM by the dry anode gas flow. The expected outcome is less water in the PEM near the anode inlet/cathode outlet than in the PEM near the anode outlet/cathode inlet. This expectation was confirmed, as shown by the images in Figure 8-2 and the integrated  $^1\text{H}$  NMR intensity values in Table 8-2. Note, that the location of  $\text{H}_2\text{O}(\text{l})$  in the cathode flow field for configuration #1 is central (Figure 8-1b), and for configuration #2 (Figure 8-2b) the  $\text{H}_2\text{O}(\text{l})$  is closer to the cathode inlet. Regions of the PEM adjacent to  $\text{H}_2\text{O}(\text{l})$  in the cathode flow field are expected to contain more water than regions of the PEM not adjacent to  $\text{H}_2\text{O}(\text{l})$ . Thus, without  $\text{H}_2\text{O}(\text{l})$  in the cathode flow field immediately opposite the anode inlet, this region of the MEA was more prone to dehydration. Several counter-flow models predict that the minimum PEM water content[31] or current density[32] occurs near the inlet of the anode gas channel. We note that although these small differences in  $^1\text{H}$  NMR signal intensity between the two halves of the MEA ROI in the counter-flow configurations can be rationalized with the above arguments, this observation warrants further investigation.

Considering the co-flow configurations (Figure 8-2c and d), the image for configuration #3 was acquired after the PEMFC operated at  $\sim 30 \text{ mW cm}^{-2}$  ( $\sim 27 \text{ mA}$ ,  $\sim 0.56 \text{ V}$ ) for 214 min, and the image for #4 was acquired after the PEMFC operated for 136 min at  $32$  to  $40 \text{ mW cm}^{-2}$  ( $\sim 32$  to  $40 \text{ mA}$ ,  $\sim 0.56$  to  $0.50 \text{ V}$ ). In both configurations, the amount of water in the  $\text{PEM}_{\text{cat}}$  near the inlets was less than in the  $\text{PEM}_{\text{cat}}$  near the outlets. The total integrated  $^1\text{H}$  NMR signal intensity of the MEA



ROI for configuration #3 is greater than for configuration #4. In addition, the integrated signal values for the two halves of the MEA ROIs differ by 13% and 25% of the value for the entire ROI for configurations #3 and #4, respectively. These differences in integral values between the two co-flow configurations are not easily accounted for. Also in Figure 8-2c and d are images that show the location of  $\text{H}_2\text{O}(l)$  accumulation in the cathode flow field. More  $\text{H}_2\text{O}(l)$  is present in the cathode flow field for configuration #3 than for configuration #4, which may account for the larger integral value obtained from the MEA ROI in configuration #3. With  $\text{H}_2\text{O}(l)$  accumulated in the outlet half of the cathode flow field for configuration #3, one would expect that half of the MEA ROI to have the largest integral; however, the integrated  $^1\text{H}$  NMR signal for the outlet half of the ROI is larger for configuration #4 (see Table 8-2), which has little  $\text{H}_2\text{O}(l)$  in the cathode flow field. These results illustrate the complexity of the interdependence between the amount of water in the  $\text{PEM}_{\text{cat}}$ ,  $\text{H}_2\text{O}(l)$  in the GDL (unseen by our technique), and  $\text{H}_2\text{O}(l)$  in the cathode flow field. Further research is required to elucidate these interdependencies. We note that our results which show that the inlets become dehydrated in co-flow configurations are qualitatively in agreement with the locally resolved impedance measurements of Schneider *et al.*[18] and numerous theoretical models[33-37].

### 8.3.2. Influence of $\text{O}_2(g)$ Flow Rate

To achieve an efficient and high performance PEMFC, selection of optimal gas flow rates is critical[8]. For example, if pure gases are used, they are either supplied in a dead-end mode (*i.e.*, flow rate equals the rate of consumption) or in a recirculation mode. If the cathode of the PEMFC is air fed, the cathode gas stream is typically supplied in a flow-through configuration with a stoichiometric ratio (*i.e.*,  $n\text{O}_2(g)_{\text{supplied}}/n\text{O}_2(g)_{\text{consumed}}$ ) of at least two[8]. When the reactant is supplied in dead-

end mode  $\text{H}_2\text{O}(l)$  may accumulate in the flow channels, and a high gas flow rate is used periodically to purge the water from the channels. In this section the influence of a high  $\text{O}_2(g)$  flow on the water content of the PEM and power output of the 30 mm PEMFC was investigated.

When the PEMFC was operated in counter-flow gas configuration #2 (see Figure 8-2b) with no change in external resistance the results shown in Figure 8-3

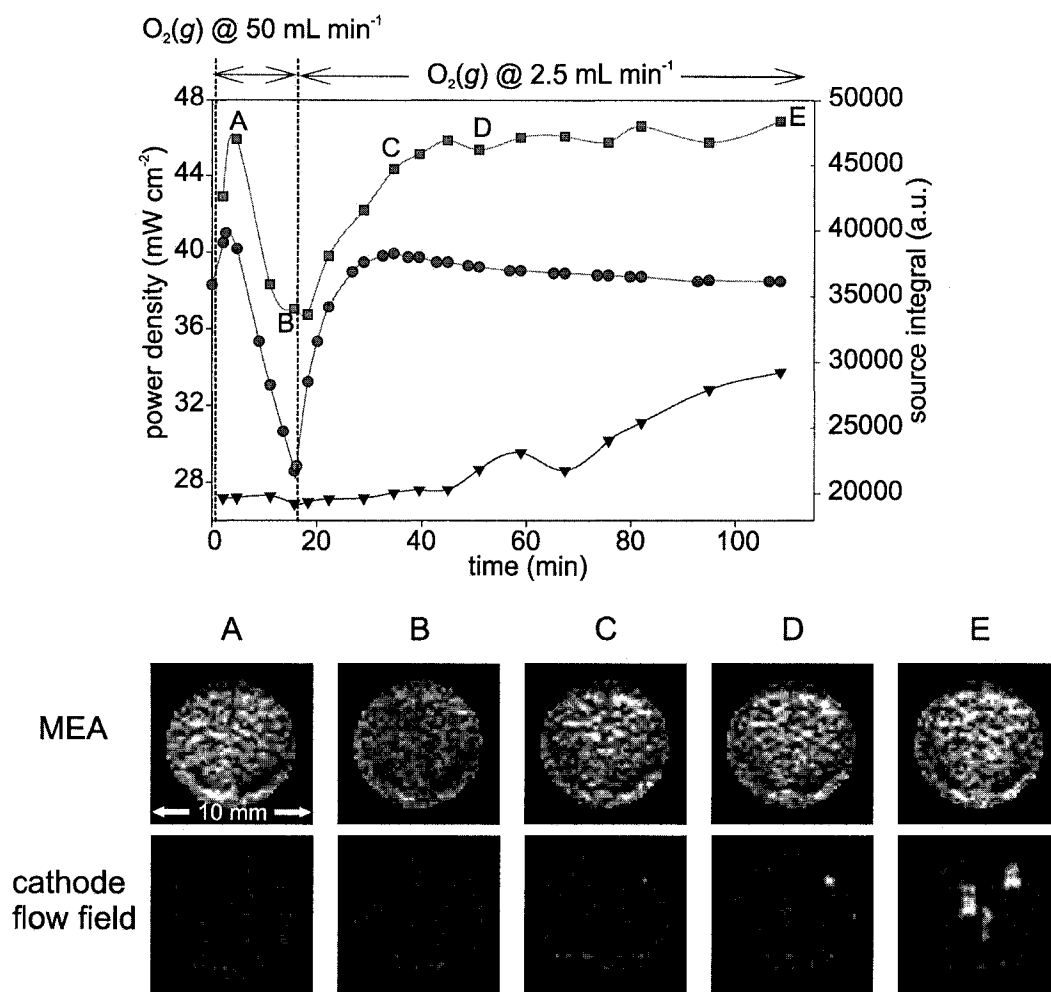


**Figure 8-3.** Top: Plot of power density and integrated  $^1\text{H}$  NMR signal intensities versus time showing the effect of changes to the  $\text{O}_2(g)$  flow rate on: power (●), MEA water content (■), and  $\text{H}_2\text{O}(l)$  in the cathode flow field (▼). Bottom:  $^1\text{H}$  NMR microscopy images (A-E) of the MEA and cathode flow field ROI from which the intensities were integrated. From  $t = 0$  to 16 min (B) the  $\text{O}_2(g)$  flow rate was  $50 \text{ mL min}^{-1}$ .

were obtained. At  $t = 0$  the  $O_2(g)$  flow rate was increased from 2.5 to 50 mL min<sup>-1</sup> to flush  $H_2O(l)$  from the cathode flow field and GDL, and to dry the MEA. As shown by the plot in Figure 8-3, there is a remarkable correlation between the power output of the cell (●) and the integrated <sup>1</sup>H NMR signal intensity from the MEA ROI (*i.e.*, PEM<sub>cat</sub>) (■) from  $t = 0$  through  $\sim t = 25$  min, confirming the expectation that the ionic conductivity of the PEM between the operating catalyst layers is closely related to cell performance. The high  $O_2(g)$  flow rate initially lead to an increase in both the cell power output and the water content in the MEA (Figure 8-3, point A). The <sup>1</sup>H NMR microscopy images corresponding to points A through E are shown below the plot. Prior to acquisition of this dataset, the PEMFC was operated in co-flow configuration #3. Thus, the initial increase in MEA water content and cell power output may have resulted from increased  $O_2(g)$  mass transport and redistribution of  $H_2O(l)$  in the cathode flow field or GDL upon switching the direction of  $O_2(g)$  flow; indeed, the image intensity integral for the right portion of the ROI increased immediately after the direction of gas flow was changed, and subsequently declined. After this initial increase in power and amount of water, both the power and the integral of the <sup>1</sup>H NMR microscopy image intensity in the MEA ROI continue to decline under the high  $O_2(g)$  flow rate (Figure 8-3, points A through B). This decrease in performance results from dehydration of the PEM. A decrease in the  $O_2(g)$  flow rate to 2.5 mL min<sup>-1</sup> resulted in an increase in MEA water content (Figure 8-3, points B through C). We expect that there is little  $H_2O(l)$  in the GDL and none was detected in the cathode flow field between points B through C. The dependence of the cell power output on the amount of water in the PEM<sub>cat</sub> is best represented between these points. This interdependence appears proportional, as is the ionic conductivity of Nafion with water content. After point C, the amount of water in

the PEM between the catalyst layers increased slowly and was expected to lead to improved ionic conductivity and cell performance, but the accumulation of  $\text{H}_2\text{O}(l)$  in the cathode flow field, and presumably the GDL, caused an overall decline of power output (Figure 8-3, points C through E).

To investigate the sensitivity of the PEMFC power output and the MEA ROI signal intensity to the  $\text{O}_2(g)$  flow rate, the flow rate was decreased in a series of steps from 50 to 2.5  $\text{mL min}^{-1}$ . Figure 8-4 shows a plot of the power response, and the integrated signal intensity values from the MEA and cathode flow field ROI. The  $^1\text{H}$  NMR microscopy images corresponding to plot points A through E are shown below the plot. At point A,1 on the plot, the MEA water content was high and a large amount of  $\text{H}_2\text{O}(l)$  was in the cathode flow field. The  $\text{O}_2(g)$  flow rate was then increased to 50  $\text{mL min}^{-1}$ . Figure 8-4, plot points A,1 to B, show that the  $\text{H}_2\text{O}(l)$  was quickly purged from the flow field and resulted in an increase in power. A small decrease in the MEA water content was also observed. As shown in Figure 8-4, points B to C, under the high  $\text{O}_2(g)$  flow rate the integrated signal intensities for both the MEA and cathode flow field ROIs, and the cell power output declined. At point C,2 on the plot, the  $\text{O}_2(g)$  flow rate was reduced to 20  $\text{mL min}^{-1}$  and resulted in increased power output and MEA water content. The  $\text{O}_2(g)$  flow rate was then decreased to 10, 5, and 2.5  $\text{mL min}^{-1}$  at plot points 3, 4, and 5, respectively. Evident from the plot and comparison of the  $^1\text{H}$  NMR microscopy images C and D in Figure 8-4, upon each reduction in  $\text{O}_2(g)$  flow rate the cell power output improved and the MEA water content increased. After the  $\text{O}_2(g)$  flow rate was reduced to 2.5  $\text{mL min}^{-1}$ , the MEA water content continued to increase; however, the cell power output began to decline as  $\text{H}_2\text{O}(l)$  accumulated in the cathode flow field (Figure 8-4, points D to E). The interdependence of cell power output and water in the  $\text{PEM}_{\text{cat}}$ ,  $\text{H}_2\text{O}(l)$

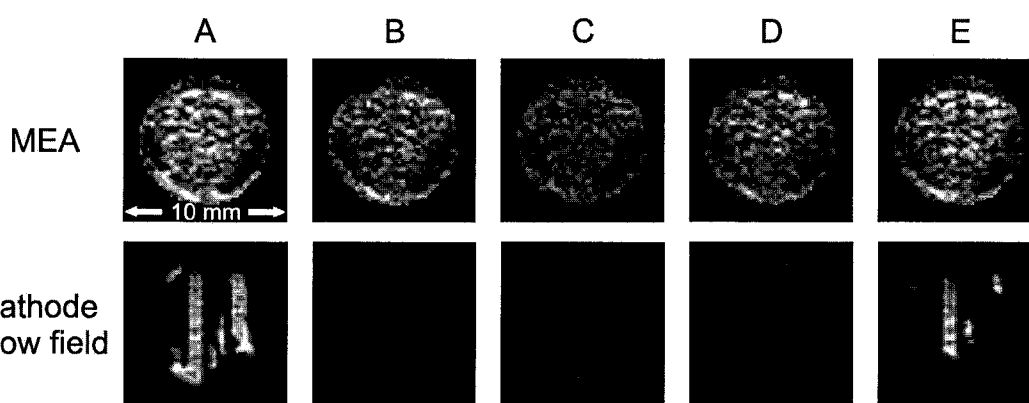
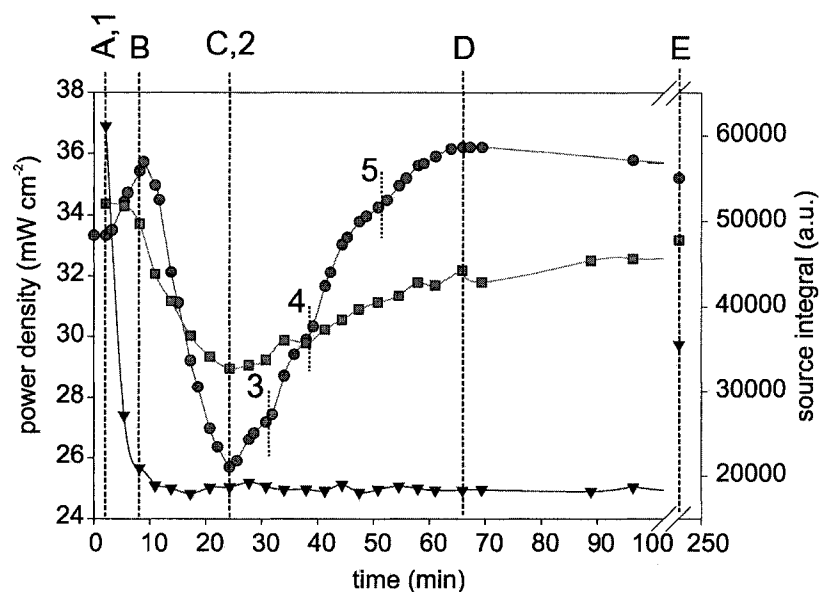


**Figure 8-4.** Top: Plot showing the sensitivity of the power density (●), MEA water content(■), and H<sub>2</sub>O(l) in the cathode flow field (▼) to changes in the O<sub>2</sub>(g) flow rate. The O<sub>2</sub>(g) flow rate was: 50 mL min<sup>-1</sup> from  $t = 0$  (A,1) to  $t = 25$  min (C,2); 20 mL min<sup>-1</sup> from  $t = 25$  min to  $t = 32$  min (3); 10 mL min<sup>-1</sup> from  $t = 32$  min to  $t = 39$  min (4); 5 mL min<sup>-1</sup> from  $t = 39$  min to  $t = 52$  min (5); and 2.5 mL min<sup>-1</sup> from  $t = 52$  min onward. Bottom: Example <sup>1</sup>H NMR microscopy images (A-E) of the MEA and cathode flow field ROIs from which the intensities were integrated. The PEMFC was operating in counter-flow gas configuration #2.

in the GDL and cathode flow field is complex. Clearly, <sup>1</sup>H NMR microscopy is an ideal technique for monitoring the distribution of water throughout an operating PEMFC and for providing unique insight regarding the performance of the cell and the effects of operating conditions.

### 8.3.3. Influence of Power Density

The results shown in Figure 8-5 were obtained with the PEMFC operating in co-flow configuration #4 (see Figure 8-2d). The plot of power density and integrated signal intensities from the  $^1\text{H}$  NMR microscopy image ROIs shown in Figure 8-5 demonstrates the sensitivity of the parameters to changes in the external circuit

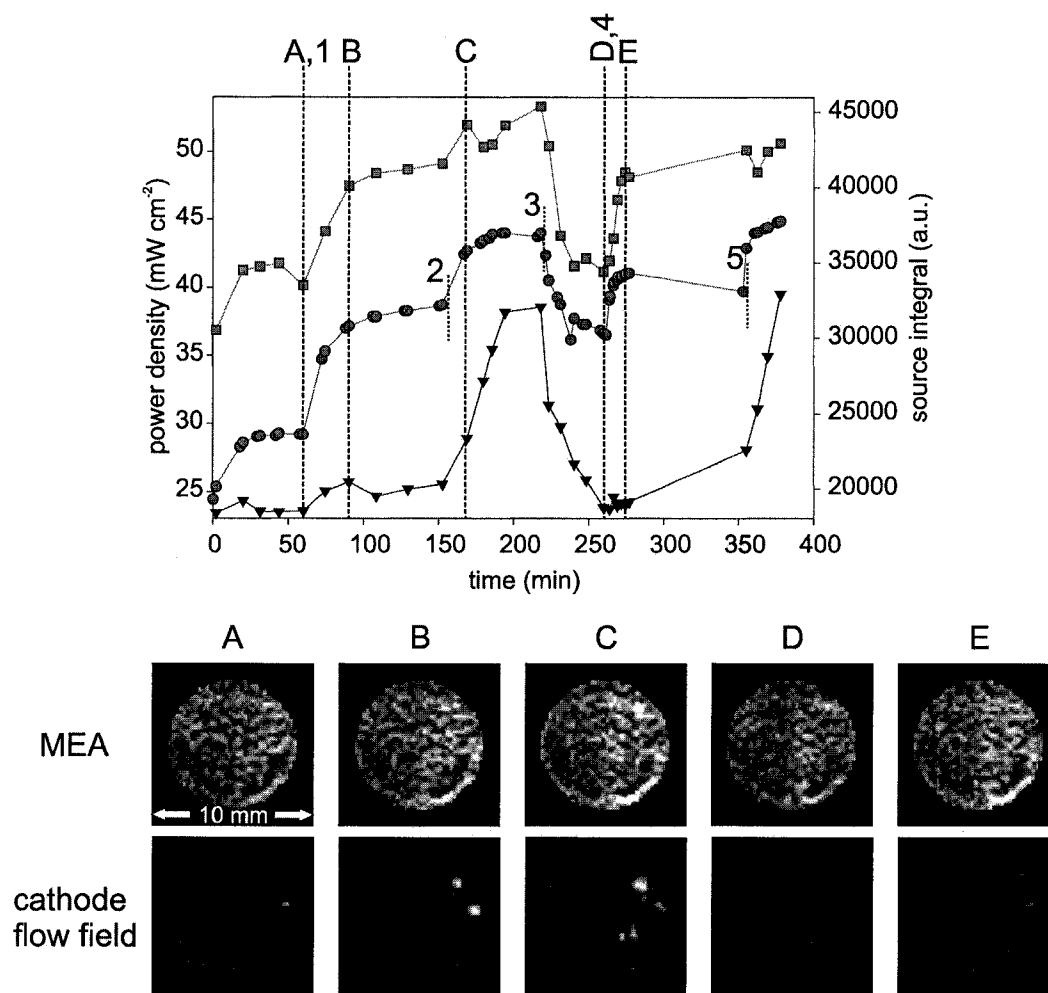


**Figure 8-5.** Top: Plot of power and integrated  $^1\text{H}$  NMR microscopy signal intensities versus time showing the effect of changes in circuit resistance and gas flow rates on the parameters; power density (●), MEA (■), and cathode flow field (▼). At  $t = 71$  min (A,1),  $t = 167$  min (2), and  $t = 356$  min (5) the external circuit resistance was decreased. At  $t = 221$  min (3) the resistance was increased. The  $\text{O}_2(\text{g})$  flow rate was  $50 \text{ mL min}^{-1}$  from  $t = 221$  min (3) to  $t = 261$  min (D,4). Bottom: Example  $^1\text{H}$  NMR microscopy images (A-E) of the MEA and cathode flow field ROI from which the intensities were integrated.

resistance. The  $^1\text{H}$  NMR microscopy images corresponding to points A through E are shown below the plot. In general, with each decrease in the external resistance the power ( $\bullet$ ) rose rapidly and then plateaued. Evident from the plots of the ROI signal intensity, the slow rise in power density was accompanied by a corresponding increase in the MEA water content ( $\blacksquare$ ) (*e.g.*, after point B). At higher power densities the amount of  $\text{H}_2\text{O}(l)$  in the cathode flow field ( $\blacktriangledown$ ) also increased, evident after point C. An interesting observation is that higher power densities lead to increased MEA water content. The increase in water was likely due to the higher current which results in the production of more water at the cathode and facilitates back-diffusion of water into the MEA. In addition, the change in MEA water content under conditions of constant gas flow rates indicates that the gas flow rates alone do not determine the MEA water content. One might expect that under optimal operating conditions the MEA water content would remain relatively constant regardless of power density. To understand the relationship between the amount of water in the PEM and the cell current and voltage, the PEM water content should be measured when the power density is changed: as a function of current (*i.e.*, operate at constant voltage), and as a function of voltage (*i.e.*, operate at constant current).

The results presented in Figures 8-3 to 8-5 show that the integrated  $^1\text{H}$  NMR microscopy image intensity in the ROI containing the MEA is correlated with the power output of the PEMFC and is affected by both changes in the  $\text{O}_2(g)$  flow rate and changes in the external resistance of the circuit. No other *in-situ* PEMFC diagnostic technique can provide such visual insight into the complicated interdependence of PEMFC operating performance, water content and distribution, and  $\text{O}_2(g)$  flow rates.

#### 8.4. Toward Quantification of the Amount of Water in the PEM

One of the ultimate goals of this research is to analyze quantitatively the amount and distribution of water throughout an operating PEMFC. In theory, the signal acquired in an NMR experiment is quantitative; assuming that the nuclear spins are in a homogeneous environment, the integrated NMR signal is proportional to the spin density. The amount of water in the PEM is related to the intensity of the  $^1\text{H}$  NMR microscopy image, but an operating PEMFC is a heterogeneous environment and as shown in §5.2 the materials affect the  $^1\text{H}$  NMR signal. Two possible approaches to relate the absolute amount of water in the PEM (*i.e.*,  $\lambda$ ) of an operating PEMFC to the integrated  $^1\text{H}$  NMR microscopy image intensity are discussed below.

The number of water molecules per  $\text{SO}_3\text{H}$  moiety,  $\lambda$ , in Nafion-117 is known to vary from  $\sim 2$  to 22; however, for Nafion exposed to temperatures  $> 105\text{ }^\circ\text{C}$  the maximum value of  $\lambda$  when immersed in  $\text{H}_2\text{O}(l)$  at  $T < 30\text{ }^\circ\text{C}$  is reported to be  $\sim 12$ [2]. The amount of water in Nafion is typically obtained through fastidious weight measurements in controlled humidity environments[1,38,39] and the EW of the PEM is then used to determine  $\lambda$ . Thus, one approach to relate the NMR signal to the PEM water content is to acquire a series of  $^1\text{H}$  NMR microscopy images of an MEA exposed to relative humidity values that are known to result in specific values of  $\lambda$ . A calibration curve could then be produced to relate the integrated NMR signal intensities to the absolute water content of the PEM. The reliability of such a calibration would be related to the reproducibility of the MEA preparation and assembly of the PEMFC (*e.g.*, catalyst loading, position of GDL, pressure of the fuel cell assembly on the MEA). As well, the integrated  $^1\text{H}$  NMR microscopy signal intensity is related to experimental parameters such as slice thickness and



orientation, pixel size, the number of signal averages, *etc.*; therefore, a calibration would have to be performed for each set of  $^1\text{H}$  NMR microscopy parameters.

The conductivity ( $\sigma$ , units  $\text{S m}^{-1}$ ) of Nafion is known to improve with increased PEM water content[1-5] (see Table 3-1). Conductivity is an intrinsic property of a material, defined as the conductance ( $G$ , unit  $\text{S}$ ) of a cross-section of the material through a specific length. Accurate determination of the conductivity of the MEA in an operating PEMFC may facilitate calculation of the amount of water in the PEM. In practice the resistance or conductance is measured and to calculate the conductivity, the cross-section (*i.e.*, area) and thickness of the membrane must be known. For Nafion, both parameters depend on water content[40]. As an approximation, changes in the total resistance of the PEMFC circuit could be attributed to changes in the conductivity of the PEM.

To investigate the existence of a correlation between MEA water content and change in the PEMFC resistance, the portion of the dataset presented in Figure 8-4 from  $t = 9$  min to  $t = 70$  min, during which  $\text{H}_2\text{O}(l)$  was not observed in the cathode flow field, was used. Data where  $\text{H}_2\text{O}(l)$  was visible were not used because changes in the PEMFC power output may also result from mass transport limitations. Over this period the power output varied from 12.8 to 18.1 mW and the integrated  $^1\text{H}$  NMR microscopy signal intensity from the MEA ROI varied from 33 000 to 44 000 a.u. A plot of the measured PEMFC conductance versus MEA ROI signal intensity revealed no obvious correlation between the parameters. The small currents achievable from the PEMFC are likely a limiting factor in obtaining values of conductance that reflect changes in PEM water content. The use of traditional PEMFC diagnostic techniques such as current interrupt or AC impedance spectroscopy may provide more accurate values of the instantaneous cell resistance (*e.g.*, separate from resistance due to activation polarization)[41].

While a correlation may exist between MEA water content and the cell resistance, using that approach to determine the absolute, or change in, water content may be difficult due to the plethora of factors that affect the properties of Nafion. For example, the conductivity of Nafion is also known to decrease at higher temperature[2-4,42] and to be sensitive to pre-treatment[3,4,42] and pressure[5]. Furthermore, Cappadonia *et al.*[4] reported that the conductance of the hot-pressed Nafion remains high even though the water uptake is much less than measured for non-treated samples. As well, a recent  $^1\text{H}$  NMR investigation of water in several Nafion membranes reported a persistent change in the signal linewidth and shape after exposure of the membrane to temperatures above 358 K[6]. To investigate further the feasibility of relating the resistance of an operating PEMFC to the amount of water in the PEM, a thorough study of the effects of PEM pre-treatment and MEA preparation on the water uptake and conductivity need to be completed.

## 8.5. Conclusions

The research presented in this chapter investigated relation between the integrated intensity of  $^1\text{H}$  NMR microscopy images and changes in PEMFC operating conditions, and evaluated the feasibility of using the image intensities to obtain the absolute water content in the PEM. The results presented demonstrate that the integral of the  $^1\text{H}$  NMR microscopy image intensity in a ROI of area approximately equal to the MEA/catalyst decal correlates well with the PEMFC power density. The  $^1\text{H}$  NMR signal integrals are greater for the counter-flow gas configurations than for the co-flow gas configurations, and in the co-flow configurations the signal integral was greater at the outlet than at the inlet. In addition, the signal integral was sensitive to  $\text{O}_2(\text{g})$  flow rate and changes in the resistance of the external circuit. Finally, the interdependence of the PEMFC power output, water the PEM between the operating catalyst layers, and  $\text{H}_2\text{O}(\text{l})$  in the GDL

and cathode flow field is complex. To pursue quantification of the amount of water in the PEM based on the integral of the  $^1\text{H}$  NMR signal intensity, further research on the effects of PEM pre-treatment and MEA preparation on the water content and conductivity need to be completed.

The interdependence of PEMFC performance on the properties of Nafion is complicated; however,  $^1\text{H}$  NMR microscopy provides a new diagnostic method for the *in-situ* investigation of these phenomena and future studies will continue to provide a better understanding of operating PEMFCs.

#### 8.6. References

- [1] Zawodzinski, T. A., Jr.; Neeman, M.; Sillerud, L. O.; Gottesfeld, S. J. *Phys. Chem.* **1991**, *95*, 6040-6044.
- [2] Zawodzinski, T. A., Jr.; Derouin, C.; Radzinski, S.; Sherman, R. J.; Smith, V. T.; Springer, T. E.; Gottesfeld, S. J. *Electrochem. Soc.* **1993**, *140*, 1041-1047.
- [3] Cappadonia, M.; Erning, J. W.; Stimming, U. *J. Electroanal. Chem.* **1994**, *376*, 189-193.
- [4] Cappadonia, M.; Erning, J. W.; Niaki, S. M. S.; Stimming, U. *Solid State Ionics* **1995**, *77*, 65-69.
- [5] Fontanella, J. J.; Edmondson, C. A.; Wintersgill, M. C.; Wu, Y.; Greenbaum, S. G. *Macromolecules* **1996**, *29*, 4944-4951.
- [6] Nosaka, A. Y.; Watanabe, S.; Toyoda, I.; Nosaka, Y. *Macromolecules* **2006**, *39*, 4425-4427.
- [7] Hinatsu, J. T.; Mizuhata, M.; Takenaka, H. *J. Electrochem. Soc.* **1994**, *141*, 1493-1498.
- [8] Barbir, F. In *PEM Fuel Cells: Theory and Practice*; Elsevier Academic Press: San Diego, 2005, 115-145.
- [9] Barbir, F. In *PEM Fuel Cells: Theory and Practice*; Elsevier Academic Press: San Diego, 2005, 271-336.

- [10] Wang, C.-Y. *Chem. Rev.* **2004**, *104*, 4727-4765.
- [11] Weber, A. Z.; Newman, J. *Chem. Rev.* **2004**, *104*, 4679-4726.
- [12] Barbir, F. In *PEM Fuel Cells: Theory and Practice*; Elsevier Academic Press: San Diego, 2005, 207-248.
- [13] Mosdale, R.; Gebel, G.; Pineri, M. *J. Membrane Sci.* **1996**, *118*, 269-277.
- [14] Bellows, R. J.; Lin, M. Y.; Arif, M.; Thompson, A. K.; Jacobson, D. J. *Electrochem. Soc.* **1999**, *146*, 1099-1103.
- [15] Satija, R.; Jacobson, D. L.; Arif, M.; Werner, S. A. *J. Power Sources* **2004**, *129*, 238-245.
- [16] Kramer, D.; Lehmann, E.; Frei, G.; Vontobel, P.; Wokaun, A.; Scherer, G. G. *Nucl. Instrum. Methods Phys. Res., Sect. A* **2005**, *542*, 52-60.
- [17] Kramer, D.; Zhang, J.; Shimoi, R.; Lehmann, E.; Wokaun, A.; Shinohara, K.; Scherer, G. G. *Electrochim. Acta* **2005**, *50*, 2603-2614.
- [18] Schneider, I. A.; Kramer, D.; Wokaun, A.; Scherer, G. G. *Electrochem. Commun.* **2005**, *7*, 1393-1397.
- [19] Hickner, M. A.; Siegel, N. P.; Chen, K. S.; McBrayer, D. N.; Hussey, D. S.; Jacobson, D. L.; Arif, M. J. *Electrochem. Soc.* **2006**, *153*, A902-A908.
- [20] Zhang, J.; Kramer, D.; Shimoi, R.; Ono, Y.; Lehmann, E.; Wokaun, A.; Shinohara, K.; Scherer, G. G. *Electrochim. Acta* **2006**, *51*, 2715-2727.
- [21] Pekula, N.; Heller, K.; Chuang, P. A.; Turhan, A.; Mench, M. M.; Brenizer, J. S.; Ünlü, K. *Nucl. Instrum. Methods Phys. Res., Sect. A* **2005**, *542*, 134-141.
- [22] Geiger, A. B.; Tsukada, A.; Lehmann, E.; Vontobel, P.; Wokaun, A.; Scherer, G. G. *Fuel Cells* **2002**, *2*, 92-98.
- [23] Schneider, I. A.; Kuhn, H.; Wokaun, A.; Scherer, G. G. *J. Electrochem. Soc.* **2005**, *152*, A2092-A2103.
- [24] Schneider, I. A.; Kuhn, H.; Wokaun, A.; Scherer, G. G. *J. Electrochem. Soc.* **2005**, *152*, A2383-A2389.

- [25] Feindel, K. W.; LaRocque, L. P. A.; Starke, D.; Bergens, S. H.; Wasylishen, R. E. *J. Am. Chem. Soc.* **2004**, *126*, 11436-11437.
- [26] Feindel, K. W.; Bergens, S. H.; Wasylishen, R. E. *J. Am. Chem. Soc.* **2006**, *128*, 14192-14199.
- [27] Feindel, K. W.; Bergens, S. H.; Wasylishen, R. E. *ChemPhysChem* **2006**, *7*, 67-75.
- [28] Callaghan, P. T. *Principles of Nuclear Magnetic Resonance Microscopy*; Oxford University Press: New York, 1991.
- [29] Yang, X. G.; Zhang, F. Y.; Lubawy, A. L.; Wang, C. Y. *Electrochem. Solid-State Lett.* **2004**, *7*, A408-A411.
- [30] Litster, S.; Sinton, D.; Djilali, N. *J. Power Sources* **2006**, *154*, 95-105.
- [31] Hsing, I. M.; Futerko, P. *Chem. Eng. Sci.* **2000**, *55*, 4209-4218.
- [32] Dutta, S.; Shimpalee, S.; Van Zee, J. W. *J. Appl. Electrochem.* **2000**, *30*, 135-146.
- [33] Ge, S. H.; Yi, B. L. *J. Power Sources* **2003**, *124*, 1-11.
- [34] Pasaogullari, U.; Wang, C. Y. *J. Electrochem. Soc.* **2005**, *152*, A380-A390.
- [35] Freunberger, S. A.; Santis, M.; Schneider, I. A.; Wokaun, A.; Büchi, F. N. *J. Electrochem. Soc.* **2006**, *153*, A396-A405.
- [36] Fuller, T. F.; Newman, J. *J. Electrochem. Soc.* **1993**, *140*, 1218-1225.
- [37] Berg, P.; Promislow, K.; St Pierre, J.; Stumper, J.; Wetton, B. *J. Electrochem. Soc.* **2004**, *151*, A341-A353.
- [38] MacMillan, B.; Sharp, A. R.; Armstrong, R. L. *Polymer* **1999**, *40*, 2471-2480.
- [39] Fontanella, J. J.; Wintersgill, M. C.; Chen, R. S.; Wu, Y.; Greenbaum, S. G. *Electrochim. Acta* **1995**, *40*, 2321-2326.
- [40] Gebel, G.; Aldebert, P.; Pineri, M. *Polymer* **1993**, *34*, 333-339.

[41] Barbir, F. In *PEM Fuel Cells: Theory and Practice*; Elsevier Academic Press: San Diego, 2005, 249-270.

[42] Slade, R. C. T.; Barker, J.; Strange, J. H. *Solid State Ionics* **1989**, *35*, 11-15.

## Chapter 9. Concluding Remarks

To achieve robust, high-performance PEMFCs, the amount and distribution of water throughout the system must be understood and controlled. The paramount objective of the research presented in this Thesis was to establish the feasibility of using  $^1\text{H}$  NMR microscopy to provide experimental insight into the relationship between the water content in, and the performance of, operating PEMFCs.

The research presented demonstrates that  $^1\text{H}$  NMR microscopy can be applied successfully to investigate the distribution of water throughout an operating PEMFC. PEMFCs capable of operating within the magnetic and RF fields required for  $^1\text{H}$  NMR microscopy experiments were successfully designed and constructed (Chapter 4). The ability to acquire images from specific regions of interest with  $^1\text{H}$  NMR microscopy (Chapter 5) facilitated the procurement of information relevant to improve the understanding of operating PEMFCs. The results from  $^1\text{H}$  NMR investigations of the operating 30 mm PEMFC presented in Chapter 6 revealed the diffusion of water from the MEA into the surrounding PEM, and the transient accumulation of  $\text{H}_2\text{O}(l)$  in the cathode flow field[1]. The  $^1\text{H}$  NMR signal from water in the carbon GDL was not observable, even with the use of SE-based experiments; however, the lack of  $^1\text{H}$  NMR signal in the GDL enabled the signal from water in the PEM to be isolated from  $\text{H}_2\text{O}(l)$  that accumulated in the flow channels. Operating the 30 mm PEMFC on dry gases, such that the MEA had to self-humidify, enabled investigation of the effects of gas flow configuration and  $\text{O}_2(g)$  flow rate on the amount and distribution of water the PEM between the operating catalyst layers[2]. As well, changes in PEM water content and the accumulation of  $\text{H}_2\text{O}(l)$  in the cathode flow channels were shown to be correlated with the power output of the PEMFC.

The use of hydrogen-deuterium exchange was found effective to introduce contrast in  $^1\text{H}$  NMR microscopy images acquired from the PEMFC (Chapter 7)[3]. Saturating the PEM with  $\text{D}_2\text{O}(l)$  and then operating the PEMFC with  $\text{H}_2(g)$  as fuel provided insight into the dehydration of the PEM. In addition, alternating between  $\text{H}_2(g)$  and  $\text{D}_2(g)$  as fuel introduced image contrast that enabled investigation of the distribution and the rate of water exchange in the PEM while maintaining steady-state operating conditions (*i.e.*, constant external resistance and gas flow rates).

The integral of the  $^1\text{H}$  NMR microscopy image intensity from the region of the PEM containing the catalyst decal was found to correlate with the power output of the PEMFC (Chapter 8). As well, the integral of the image intensity responded to changes in the gas inlet/outlet configuration, the  $\text{O}_2(g)$  flow rate, and the PEMFC power density.

Critical advances have been made over the past several decades in understanding PEMFCs and the development of systems for widespread commercial use. Although a number of hurdles remain, the need to develop alternative energy sources is increasing, and manufacturers have produced for example, hydrogen-powered fuel-cell test vehicles[4]. Recent development and use of methods amenable to looking inside an operating PEMFC have provided fuel cell experts with physical evidence and images to aid in the understanding of these dynamic and complex systems. The information obtainable with  $^1\text{H}$  NMR microscopy regarding the interdependence of PEMFC operating performance, gas flow configuration, gas flow rates, and water distribution is not available from other techniques.  $^1\text{H}$  NMR microscopy, the use of transparent fuel cells, neutron imaging, and other methods evolving, are complimentary techniques for visualizing operating PEMFCs. The data obtained from such investigations should be combined to verify results and used, for example, to address limitations in water management,



and to develop better models to understand water and gas transport in PEMFCs.  $^1\text{H}$  NMR microscopy provides an opportunity to obtain unique, reliable, quantitative, high-resolution information regarding the distribution of water throughout operating PEMFCs. The diversity in the size and strength of widely available commercial magnets for imaging systems, as well as accessories such as variable temperature units, adds versatility and potential to research involving  $^1\text{H}$  NMR microscopy of operating PEMFCs. NMR microscopy will continue to be an enlightening tool for investigating the water distribution, materials, and designs of operating PEMFCs.

#### 9.1. References

- [1] Feindel, K. W.; LaRocque, L. P. A.; Starke, D.; Bergens, S. H.; Wasylishen, R. E. *J. Am. Chem. Soc.* **2004**, *126*, 11436-11437.
- [2] Feindel, K. W.; Bergens, S. H.; Wasylishen, R. E. *J. Am. Chem. Soc.* **2006**, *128*, 14192-14199.
- [3] Feindel, K. W.; Bergens, S. H.; Wasylishen, R. E. *ChemPhysChem* **2006**, *7*, 67-75.
- [4] Schneider, D. In *Am. Sci.*, 2005; Vol. 93, pp 410-411.

## Chapter 10. Future Research Directions and Challenges

$^1\text{H}$  NMR microscopy is the only experimental technique by which regions of interest in an operating PEMFC can selectively be visualized and investigated. Performing the research and analyzing the results presented in this Thesis, and sifting through the immense body of relevant literature has revealed the potential of NMR microscopy to further the understanding of operating PEMFCs. This chapter provides an overview of potential research directions and topics.

### 10.1. NMR Techniques

The  $^1\text{H}$  NMR microscopy investigations reported in this Thesis were completed using Fourier imaging, FI, techniques. One of the limitations encountered was the inability to detect the  $^1\text{H}$  NMR signal from water in the GDL as a result of rapid  $T_2$  relaxation (see Chapter 5) and the signal echo times on the order of ms necessary for FI. The potential of NMR microscopy methods that enable a shorter delay between signal excitation and detection, such as single-point imaging[1] or projection-reconstruction[1,2] techniques, should be investigated.

### 10.2. $\text{H}_2/\text{O}_2$ PEMFCs

#### 10.2.1. Water in the MEA

$^1\text{H}$  NMR microscopy investigations of the 30 mm PEMFC revealed that when operating with dry feed gases, self-humidification of the MEA can occur in counter-flow configurations, but the co-flow configurations dried the MEA at the gas inlets (Chapters 6 and 7)[3]. Humidification of the anode gas stream is often used to prevent dehydration of the MEA and improve PEMFC performance[4];  $^1\text{H}$  NMR microscopy studies of the 30 mm PEMFC operating in a co-flow gas configuration with humidified  $\text{H}_2(\text{g})$  are expected to reveal the existence of more uniform MEA hydration in comparison to results obtained operating with dry gases.

To further investigate the interrelation of MEA water content and PEMFC power output,  $^1\text{H}$  NMR microscopy experiments could be performed with PEMFCs operating under constant voltage and constant current conditions (*i.e.*, allow the power to change as a function of only current or only voltage). Such investigations may reveal the individual effects of current and voltage on the MEA water content. In addition, the use of a PEMFC with a larger catalyst decal (to achieve higher currents) may better facilitate the investigation of the relation between MEA resistance and the amount of water in the PEM.

Investigations with the 10 mm PEMFC and birdcage coil can attain better resolution more rapidly; however, in the presence of the Toray TGP-H-060 carbon paper, the thickness of the PEM visible between the catalysts was small in comparison to the physical thickness. The influence of a thinner GDL, such as TGP-H-030 (110  $\mu\text{m}$ ) should be investigated.

#### 10.2.2. Variable Temperature Studies

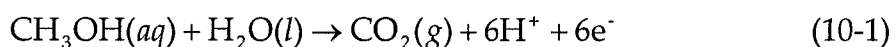
PEMFCs are often operated at elevated temperature to improve catalytic activity and PEM transport properties[4-6]. In large PEMFC stacks heat is generated by the operating cells, and active cooling is required to prevent dehydration of the PEM[4-6]. The research conducted in this Thesis was completed with PEMFCs operating within the gradient unit maintained at 20 °C. The temperature range of the gradient cooling unit is approximately 5 to 50 °C when using water as the coolant. Although a narrow temperature range, some insight may be gained regarding the temperature dependence of PEMFC performance as related to water content and distribution. To determine accurately the operating temperature of the PEMFC, thermocouples should be incorporated in future designs.

A topic of concern with commercial PEMFCs, particularly with automotive applications in cooler climates, is the cold- or freeze-start[4,7]. Apart from the

practical aspects of starting a frozen PEMFC, the repeated expansion and contraction of PEMs and PEMFC stacks can lead to failure of materials[8]. Crude experiments could be completed simply by freezing the PEMFC prior to performing  $^1\text{H}$  NMR microscopy experiments. As well, variable temperature units for NMR microscopy are commercially available.

### 10.3. Direct Alcohol PEMFCs

The use of alcohol fuelled PEMFCs is of interest for portable electronic devices and transportation applications due to the liquid state of the fuel, and ease of fuel distribution and refuelling[9]. For a direct methanol PEMFC, the reaction at the anode is[9]:



The  $\text{CO}_2(g)$  formed at the anode from the oxidation of methanol emerges from the GDL and must be removed from the flow channels or access of the catalyst to the fuel may be blocked. To investigate these processes, PEMFCs have been constructed from transparent materials to observe the formation of  $\text{CO}_2(g)$  bubbles at the GDL surface and the subsequent transport in the anode flow channels[10,11]. The potential of using NMR microscopy to reveal the space created by the  $\text{CO}_2(g)$  formed at the anode should be investigated. Preliminary results of a  $^1\text{H}$  NMR microscopy investigation of similar phenomena in a direct formic acid fuel cell have been reported[12].

Although Nafion is essentially impermeable to  $\text{H}_2(g)$  and  $\text{O}_2(g)$ , methanol can readily be absorbed. As a result, the crossover of methanol from the anode to the cathode is difficult to prevent[9]. If the chemical shift differences between the water and methyl protons can be resolved in the PEMFC environment, chemical shift selective imaging[2,13] may provide some insight into methanol crossover. Another

approach to image selectively the  $^1\text{H}$  NMR microscopy image from only methanol would be to use  $\text{CH}_3\text{OD}$  in  $\text{D}_2\text{O}(l)$  as fuel with an MEA hydrated with  $\text{D}_2\text{O}$ . If the PEMFCs operate successfully on methanol as fuel, investigations with alcohols less prone to crossover (*e.g.*, 2-propanol) could be pursued.

#### 10.4. PEM Pre-Treatment and MEA Preparation

The sheer volume of literature on the properties of Nafion and other PEMs, experimental investigations of operating PEMFCs, and theoretical models is overwhelming. Often a lack of consistency in PEM pre-treatment or the use of now unavailable PEMs renders some of the early reports of little relevance. Several studies that are critical and relevant to understand and improve the operation of PEMFCs appear to be lacking. As is stated throughout the PEMFC literature, the water content of PEMs such as Nafion is very sensitive to PEM pre-treatment[14] and humidity[15,16]. As a result, the ionic conductivity of Nafion and the performance of PEMFCs are also related to the PEM water content. Heat treatment [16-18] and hot-pressing[17] are also known to change the properties of Nafion, yet there is a lack of studies on the effects of MEA preparation on PEM water content, the diffusion of water in the PEM, and the ionic conductivity. As shown in Figure 10-1 the intensity of the  $^1\text{H}$  NMR microscopy image in the region that was subject to hot-pressing is different from the surrounding PEM.

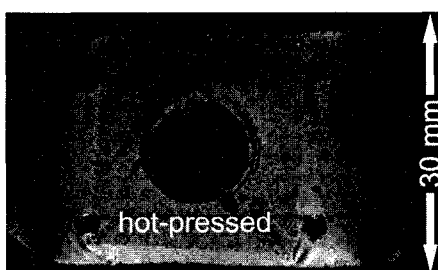


**Figure 10-1.**  $^1\text{H}$  NMR microscopy image of the MEA and PEM surrounding the catalyst decal that shows the different image intensity obtained from the hot-pressed PEM. GE image acquisition parameters:  $T_R = 200$  ms,  $T_E = 2.5$  ms, FOV = 30 mm  $\times$  50 mm, MTX = 256<sup>2</sup>, pixel size = 117  $\mu\text{m}$   $\times$  195  $\mu\text{m}$ , 64 averages, total experiment time = 54 min 36 s.

## 10.5. New Materials and Designs

The results presented in this Thesis were obtained using PEMFCs with MEAs constructed using the industry standard PEM, Nafion. Much effort, however, is dedicated to the development of PEMs with, for example, improved conductivity or decreased dependence of conductivity on membrane water content[19,20]. Similarly, other components of PEMFCs are continually being revised and improved including the materials, coatings, and designs of flow channels[21] and GDLs[22,23].  $^1\text{H}$  NMR microscopy can provide a direct view of the effects of different materials and designs on the resulting distribution of water throughout operating PEMFCs, and should prove to be an effective tool to complement other fuel cell diagnostic techniques.

## 10.6. References

- [1] Blümich, B. *NMR Imaging of Materials*; Oxford University Press: New York, 2000.
- [2] Callaghan, P. T. *Principles of Nuclear Magnetic Resonance Microscopy*; Oxford University Press: New York, 1991.
- [3] Feindel, K. W.; Bergens, S. H.; Wasylshen, R. E. *J. Am. Chem. Soc.* **2006**, *128*, 14192-14199.
- [4] Barbir, F. *PEM Fuel Cells: Theory and Practice*; Elsevier Academic Press: San Diego, 2005.
- [5] Hoogers, G., Ed. *Fuel Cell Technology Handbook*; CRC Press LLC: Boca Raton, 2003.
- [6] Larminie, J.; Dicks, A. *Fuel Cell Systems Explained*; 2nd ed.; John Wiley and Sons Ltd.: Chichester, 2003.
- [7] Ge, S. H.; Wang, C. Y. *Electrochem. Solid-State Lett.* **2006**, *9*, A499-A503.
- [8] St-Pierre, J.; Wilkinson, D. P.; Knights, S.; Bos, M. L. *J. New Mater. Electrochem. Syst.* **2000**, *3*, 99-106.

- [9] Hogarth, M. In *Fuel Cell Technology Handbook*; Hoogers, G., Ed.; CRC Press: Boca Raton, 2003, Chapter 7.
- [10] Argyropoulos, P.; Scott, K.; Taama, W. M. *Electrochim. Acta* **1999**, *44*, 3575-3584.
- [11] Argyropoulos, P.; Scott, K.; Taama, W. M. *J. Appl. Electrochem.* **1999**, *29*, 661-669.
- [12] Ha, S.; Dunbar, Z.; Masel, R. *Abstr. Pap. Am. Chem. S.* **2005**, *230*, U1638-U1639.
- [13] Haacke, E. M.; Brown, R. W.; Thompson, M. R.; Venkatesan, R. *Magnetic Resonance Imaging: Physical Principles and Sequence Design*; John Wiley and Sons: New York, 1999.
- [14] Slade, R. C. T.; Barker, J.; Strange, J. H. *Solid State Ionics* **1989**, *35*, 11-15.
- [15] Zawodzinski, T. A., Jr.; Neeman, M.; Sillerud, L. O.; Gottesfeld, S. *J. Phys. Chem.* **1991**, *95*, 6040-6044.
- [16] Zawodzinski, T. A., Jr.; Derouin, C.; Radzinski, S.; Sherman, R. J.; Smith, V. T.; Springer, T. E.; Gottesfeld, S. *J. Electrochem. Soc.* **1993**, *140*, 1041-1047.
- [17] Cappadonia, M.; Erning, J. W.; Niaki, S. M. S.; Stimming, U. *Solid State Ionics* **1995**, *77*, 65-69.
- [18] Nosaka, A. Y.; Watanabe, S.; Toyoda, I.; Nosaka, Y. *Macromolecules* **2006**, *39*, 4425-4427.
- [19] Rozière, J.; Jones, D. J. *Annu. Rev. Mater. Res.* **2003**, *33*, 503-555.
- [20] Hickner, M. A.; Ghassemi, H.; Kim, Y. S.; Einsla, B. R.; McGrath, J. E. *Chem. Rev.* **2004**, *104*, 4587-4611.
- [21] Li, X. G.; Sabir, M. *Int. J. Hydrogen Energy* **2005**, *30*, 359-371.
- [22] Dicks, A. L. *J. Power Sources* **2006**, *156*, 128-141.
- [23] Williams, M. V.; Begg, E.; Bonville, L.; Kunz, H. R.; Fenton, J. M. *J. Electrochem. Soc.* **2004**, *151*, A1173-A1180.

## Appendix A. List of Publications

### A.1. Publications Based on Material in this Thesis

Kirk W. Feindel, Steven H. Bergens, and Roderick E. Wasylishen. "Use of Hydrogen-Deuterium Exchange for Contrast in  $^1\text{H}$  NMR Microscopy Investigations of an Operating PEM Fuel Cell." *To be submitted*.

Kirk W. Feindel, Steven H. Bergens, and Roderick E. Wasylishen. "The Influence of MEA Water Content on the Performance of a PEMFC as Investigated by  $^1\text{H}$  NMR Microscopy." *Submitted to Phys. Chem. Chem. Phys.* (Invited article)

Kirk W. Feindel, Steven H. Bergens, and Roderick E. Wasylishen. "Insights into the Distribution of Water in a Self-Humidifying  $\text{H}_2/\text{O}_2$  PEM Fuel Cell using  $^1\text{H}$  NMR Microscopy." *J. Am. Chem. Soc.* **2006**, *128*, 14192-14199.

Kirk W. Feindel, Steven H. Bergens, and Roderick E. Wasylishen. "The Use of  $^1\text{H}$  NMR Microscopy to Study Proton-Exchange Membrane Fuel Cells." *ChemPhysChem.* **2006**, *7*, 67-75. (Invited *Concepts* article)

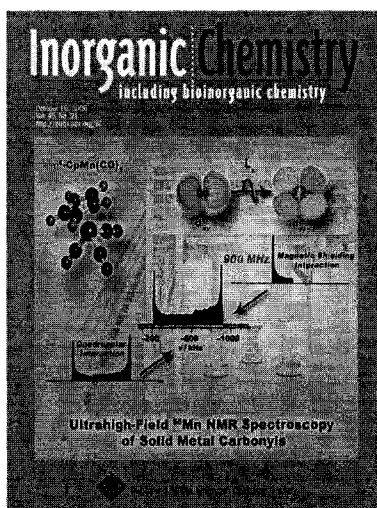
Kirk W. Feindel, Logan P.A. LaRocque, Dieter Starke, Steven H. Bergens, and Roderick E. Wasylishen. "In Situ Observations of Water Production and Distribution in an Operating  $\text{H}_2/\text{O}_2$  PEM Fuel Cell Assembly Using  $^1\text{H}$  NMR Microscopy." *J. Am. Chem. Soc.* **2004**, *126*, 11436-11437.



## A.2. Other Publications Resulting from Ph.D. Research

Kirk W. Feindel, Kristopher J. Ooms, and Roderick E. Wasylshen. "A Solid-State  $^{55}\text{Mn}$  NMR Spectroscopy and DFT Investigation of Manganese Pentacarbonyl Compounds." *Submitted to Phys. Chem. Chem. Phys.*

Kristopher J. Ooms, Kirk W. Feindel, and Roderick E. Wasylshen. "Ultra-High Field NMR Spectroscopy of Quadrupolar Transition Metals:  $^{55}\text{Mn}$  NMR of Several Solid Manganese Carbonyls." *Inorg. Chem.* **2006**, *45*, 8492-8499. (Cover article)



Mathew J. Willans, Kirk W. Feindel, Kristopher J. Ooms, and Roderick E. Wasylshen. "An Investigation of Lanthanum Coordination Compounds by Using Solid State  $^{139}\text{La}$  NMR Spectroscopy and Density Functional Theory" *Chem. Eur. J.* **2006**, *12*, 159-168.

Kristopher J. Ooms, Kirk W. Feindel, Mathew J. Willans, Roderick E. Wasylishen, John V. Hanna, Kevin J. Pike, and Mark E. Smith. "Multiple-Magnetic Field  $^{139}\text{La}$  NMR and Density Functional Theory Investigation of the Lanthanum(III) Halides." *Solid State Nucl. Magn. Reson.* **2005**, *28*, 125-124.

Kirk W. Feindel and Roderick E. Wasylishen. "A Relativistic DFT Study of One-Bond Fluorine-X Indirect Spin-Spin Coupling Tensors." *Magn. Reson. Chem.* **2004**, *42*, S158-S167.

Kirk W. Feindel and Roderick E. Wasylishen. "Phosphorus Magnetic Shielding Tensors for Transition-Metal Compounds Containing Phosphine, Phosphido, and Phosphinidene Ligands: Insights from Computational Chemistry." *Can. J. Chem.* **2004**, *82*, 27-44.

## Appendix B. You and Your PEMFC

### B.1. Maintenance

The most fragile part of both PEMFCs is the Au wire. When connected to the RF shielded cables, excessive movement of the cables can bend and/or break the Au wires. To add some rigidity to the wire on the 10 mm PEMFC, Teflon tubing is used to create a sheath over the wire prior to soldering the Au contact. Larger diameter Teflon tubing is used as a sheath over the wire, contacts, the screws to add rigidity. For the larger half of the 10 mm PEMFC the wire has broken off at the screw through which the wire runs and required the entire wire to be replaced. The wire is 0.5 mm diameter and 99.95% pure. When the wire in the smaller half of the 10 mm PEMFC requires replacement, the wire should be looped around the flow field in a clockwise direction. In the existing counter-clockwise configuration the end of the wire catches on the MEA during assembly of the cell and deforms the loop. When the Au wire is replaced a new latex O-ring needs to be punched using the appropriate dies (Figure B-1b). The screws through which the Au wire is placed should be loosened/tightened with the tools shown in Figure B-2. For the 30 mm

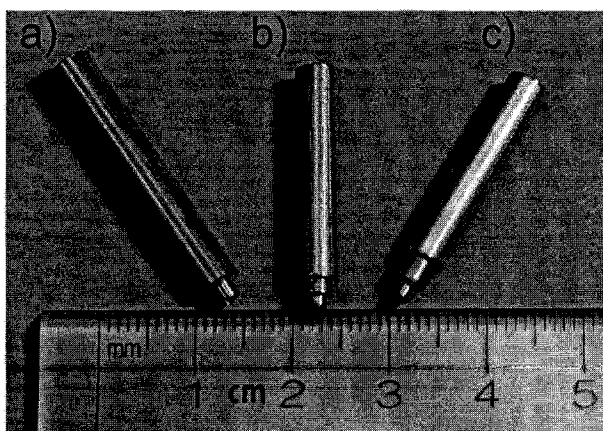


**Figure B-1.** The stainless steel dies machined for punching the latex O-rings for use with the 10 mm PEMFC. a and c) for the inlet/outlet tubes, b) for the Au-wire.

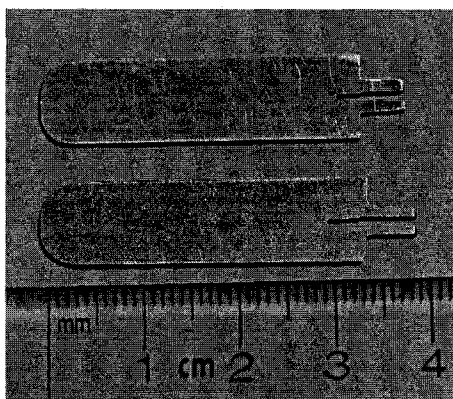


**Figure B-2.** The tools used to tighten or loosen the screws through which the Au wire is placed in the 10 mm PEMFC.

PEMFC the Au wire tends to bend away from, or against, the side of the assembly. The wire is 0.813 mm diameter 99.9% pure.

The O-rings punched from latex septa and used to seal the gas inlet/outlet tubes on the 10 mm PEMFC are not very durable. Typically they have to be replaced after each assembly/disassembly due to tearing caused from compression of the O-ring against the threads by the screws. The O-rings are punched using the dies shown in Figure B-1a and c. The Simriz O-rings used in the 30 mm PEMFC have been durable in the highly acidic conditions against the Nafion. The only O-rings that have been replaced are the Viton O-rings that are used to seal the gas inlet/outlet tubes. These tubes will eventually crack and should be replaced annually.

The TGP-H-060 used for the GDLs is brittle. After extended use or numerous assembly/disassembly the materials will begin to soften and fray and should be replaced. Replacement of the GDLs is *recommended* after each period of use and disassembly. The carbon from the GDL will coat the ridges of the flow channels and small pieces may break off and enter the flow channels. Prior to each assembly the flow channels should be cleaned with triple distilled water and a Kim-wipe or Q-tip.

The four screws used to assemble the 30 mm PEMFC are machined from nylon and are not very durable. Eventually the threads will strip and/or the screws will stretch. A new set of screws is typically kept on hand. Remember to have at least four new screws machined before using the last one.

## B.2. Assembly

### B.2.1. 30 mm PEMFC

The assembly of the 30 mm PEMFC is completed most easily with the inlet/outlet tubes detached. The only unique feature of the PEMFC is the holes on the outside of one half of the cell. For consistency, the MEA is oriented such that this half of the PEMFC is the cathode. Under an optical microscope (Prof. Mar's lab) the anode catalyst decal tends to look smooth with no scratches, but has a crackle; the cathode usually looks scratchy and has a gray tinge.

The first time an MEA is used, wet it in triple distilled water, then place it on one half the PEMFC assembly. Centre the catalyst decal over the flow field, make holes in the PEM for the screws, and trim the PEM flush with the edges of the assembly. After cleaning the flow channels, place a drop of triple distilled water in each flow field and place the GDL over the flow field. The GDLs are punched with the die shown in Figure B-3a. The surface tension of the water holds the GDL in place. Seat the screws in the cathode half of the assembly and place the MEA (cathode down) on top of the GDL and feed the screws through the holes in the PEM. Now place this half of the PEMFC over the anode half (with the GDL already in place) and tighten the four screws. Once assembled, the O-ring around the flow field holds the GDLs in place.

To attach the inlet/outlet tubes to the PEMFC, first feed each of the four tubes through a screw and place an O-ring over each tube at the bottom of the screw. For each tube and screw, feed the tube into the top of the PEMFC until it stops. Then

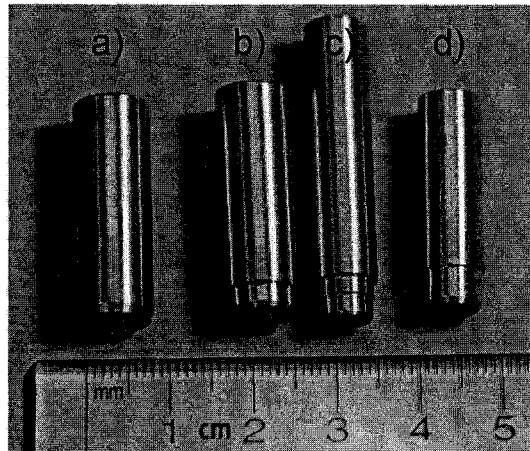


**Figure B-3.** The stainless steel dies machined for punching: a) the GDL for the 30 mm PEMFC, b) the MEA for the 10 mm PEMFC, c) the GDL for the 10 mm PEMFC, and d) a larger GDL for the 10 mm PEMFC (typically too large).

slide the O-ring down the tube and use fine-point tweezers to push it into the socket for the screw. Once the O-ring is seated, the screw can first be hand-tightened, and then tightened with a large pair of tweezers with ridges or a pair of needle-nose pliers that grip the screw heads. Once assembled the cell is submerged in a beaker of triple distilled water and tested for gas leaks.

#### B.2.2. 10 mm PEMFC

Assembling the 10 mm PEMFC is tricky, and can often take the better part of a day before successfully completed. To ensure that the flow field patterns are properly aligned, a jig was machined to hold the two halves of the PEMFC in place (see Figure B-4). Note that there are stainless steel dies for punching out the MEA and GDLs (Figure B-3b and c). The size of the catalyst decal and die are such that a small ring of PEM will remain around the catalyst decal. This small ring of PEM is necessary to make an effective seal against the O-rings surrounding the flow channels. The steps outlined below are what I have found to provide the best assembly-success rate.

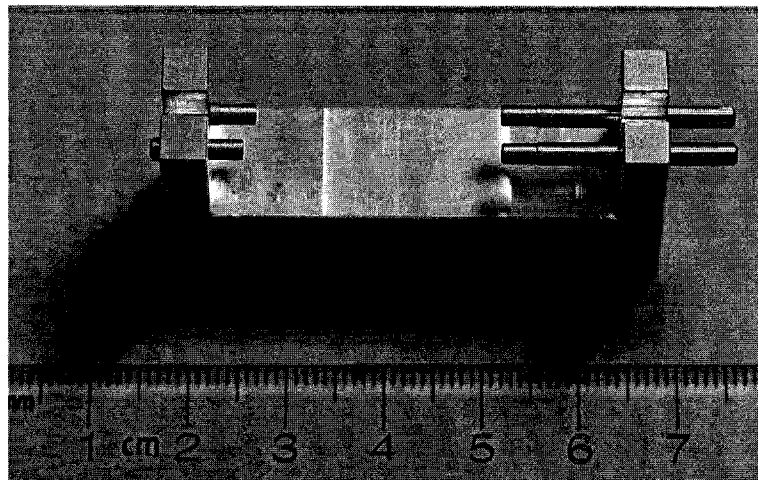


**Figure B-4.** The jig used for assembling the 10 mm PEMFC.

The first step is to ensure that the flow channels are clean and that the O-rings are seated properly around the Au-rings. The GDLs are sized appropriately to fit within the O-rings, and keeping them in position is the key to a successful assembly. If a GDL breaches the O-rings the PEMFC will leak. Place a drop of triple distilled water into each flow channel and then seat the GDLs over the flow fields. Next, place the MEA on top of the GDL that is seated over the flow channel of the larger half of the PEMFC, *i.e.*, on the pedestal. Hold this half of the PEMFC up-right. Bring the smaller half of the PEMFC (with the GDL seated within the O-ring) down on top of the larger half of the PEMFC and slowly twist the assembly together. For the flow channels to be aligned properly the Au wires existing the PEMFC also need to be aligned; therefore, finger-tighten the assembly as much as possible while maintaining the alignment of the Au wires. This is the period during which the GDLs may become misaligned. Unfortunately you won't know for sure until the cell is completely assembled and tested for leaks.

Now the assembly jig is required. To use the jig the Teflon tubes over the Au wire screws and the screws sealing the inlet/outlet tubes and latex O-rings need to

be removed. You will notice that the head of the screw sealing the Au-ring on the larger half of the PEMFC is larger than the screw used on the other half of the PEMFC. Similarly, on the assembly jig, only one end has a slot large enough to accommodate the larger screw head. In addition, this end of the jig has longer pins (Note that the pins can fall through small holes in your pocket, at which time you'll have to ask for new ones to be machined). The PEMFC is seated in the jig and the pins are pressed into the sockets for the inlet/outlet screws. On the outside of the smaller half of the PEMFC there are two flattened regions. These are to enable a wrench to be used to tighten the cell. To prevent slipping the flat regions were machined to match the Craftsman 10 mm wrench shown in Figure B-5.

To attach the inlet/outlet tubes to the 10 mm PEMFC, the same process as described above for the 30 mm PEMFC is followed. The only difference is that the latex O-rings used usually need to be replaced after each assembly/disassembly. If the PEMFC leaks from the main assembly (*i.e.*, not around the inlets/outlets), the cell must be disassembled and you'll likely find a deformed GDL. Use the appropriate die to punch new GDLs and repeat the assembly process.

When placing the 10 mm PEMFC in the 10 mm diameter birdcage resonator, two components are required to centre the cell in the coil. Depending on the orientation of the PEMFC one of the two shims shown in Figure B-6a and b are

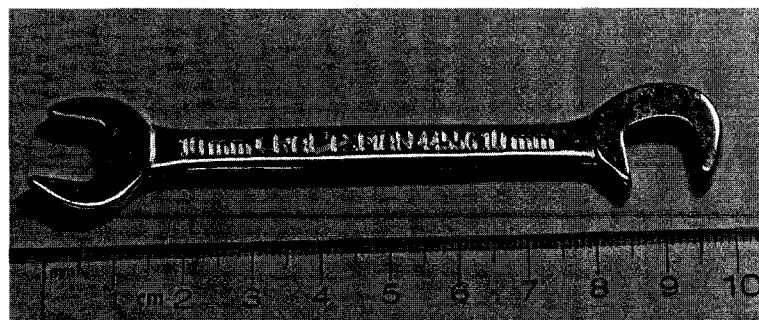
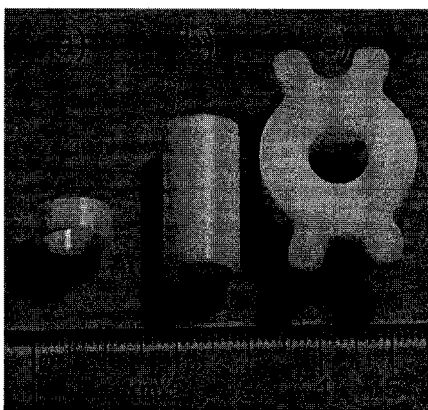


Figure B-5. The wrench used for tightening the 10 mm PEMFC assembly while in the jig.





**Figure B-6.** a and b) the shims used to centre the MEA of the 10 mm PEMFC in the 10 mm birdcage resonator. c) the platform placed in the top of the probe-head, below the 10 mm PEMFC, to enable the inlet/outlet tubes and RF shielded cables to reach the PEMFC.

required. As well, the platform shown in Figure B-6c is placed in the probe-head below the coil; the hole is required for the inlet/outlet tubes and the RF shielded cables.

### B.3. Conditioning

Whenever a new MEA is used the PEMFC should first be filled with triple distilled water to hydrate the PEM. The cell should then be operated with low gas flow rates (*e.g.*,  $\text{H}_2(\text{g}) @ 5 \text{ mL min}^{-1}$  and  $\text{O}_2(\text{g}) @ 2.5 \text{ mL min}^{-1}$ , or less) with out an external resistance. When the cell potential reaches  $\sim 1 \text{ V}$ , the smallest current possible with the variable resistor (*i.e.*,  $\sim 1.7 \text{ mA}$ ) should be drawn from the cell for 24 to 48 hrs, with the measurement of a polarization curve. After this initial conditioning period the cell should be operated with moderate currents such that the cell potential does not drop below  $\sim 0.7 \text{ V}$ . The MEA used in this research has been used for approximately 18 months without noticeable degradation in the performance.

### B.4. Long-Period Operation

The 30 mm PEMFC has often been operated continually for extended periods of up to several weeks. When leaving the PEMFC unattended, the operating

conditions should be chosen such that extensive dehydration or flooding of the cathode flow field does not occur. In practice the 30 mm PEMFC has not been left for extended periods (*e.g.*, overnight) with  $I > 40$  mA or with  $O_2(g)$  flow rates  $> 10$  mL  $min^{-1}$ . Keep in mind that each MEA may have slightly different performance characteristics.

## Appendix C. User Scale Mapping of Image Intensity

In ParaVision after acquisition of a dataset the image is automatically reconstructed. The parameters used for reconstruction available in the *Parameter Editor for RECO\_IN* window accessed through the *Spectrometer Control Tool* under the menu *Reco*, submenu *RECO Edit*. The pixel intensities are determined by mapping the largest source signal in the dataset to the maximum value of the chosen scale. For example, for *RECO: output word size = \_16BIT\_SGN\_INT*, the maximum value is 32767. The default selection for *RECO: output mapping* is *ABSOLUTE\_MAPPING* which ensures that the dynamic range of the parameter is used for the dataset and each image in a dataset (e.g., from different slices) is mapped with the same parameters. However, when the images are displayed in the *Image Display and Processing* window an 8 bit scale is used and *each* image from a particular dataset is displayed such that the display dynamic range is used, i.e., the image intensities are not comparable. To compare the intensity of images from the same reconstruction in the *Image Display and Processing* window, the intensities must be rescaled manually by accessing the *Rescale Dialog* through the *View* submenu *Window Image Intensity*. In the *Rescale Dialog*, select the *user defined* rescaling type and set the absolute upper interval to the maximum value observed in the dataset (i.e., check this value for each of the images you wish to compare and use the largest value). This is the *RECO\_map\_max* value found in the *reco* file for that reconstruction (e.g., */opt/xwinnmr/data/user/nmr/dataset/reco/exp#/pdata/reco#/reco*). When all images from a particular reconstruction are displayed with the same *Window Image Intensity* parameters, then the image intensities as shown in the *Image Display and Processing* window are comparable. Once *user defined* rescaling is selected the parameters can be copied between displayed images by holding down

the *i* key and the middle mouse button and dragging the *Int. Scaling User Def.* box that appears to another image.

Often in experiments of the operating PEMFC we wish to compare the intensities of images between datasets. This requires reconstructing the datasets with user defined output mapping. To reconstruct an image with different parameters the dataset should first be copied using the *Clone Reco* shortcut menu (*i.e.*, right mouse button) accessible from the dataset selected in the *Scan Control* window. After cloning the dataset, in the *Scan Control* window the comment will read *NOT RECONSTRUCTED* rather than *COMPLETED*. As mentioned above, different mapping options are available in the *Parameter Editor for RECO\_IN* window under *RECO: output mapping*. To reconstruct images with the same output mapping *RECO: output mapping = USER\_SCALE\_MAPPING* is used. Two parameters can be defined, *RECO: output slope* and *RECO: output offset*. The offset is left at 0, but the slope must be defined. The *RECO: output slope* is the factor by which the *RECO\_map\_max* value is multiplied by to obtain the maximum allowed *RECO: output word size*. To determine the value for *RECO: output slope*, one must first decide which datasets are to be compared, typically a series of experiments acquired with the identical parameters but at different times. Then, from the original reconstructed datasets, the minimum value of *RECO\_map\_slope* (also in the *reco* file, the location of which is described above) must be determined for the datasets which are to be compared. The minimum value of *RECO\_map\_slope* (or rounded down) is the value to be used for the *RECO: output slope*. After each dataset is reconstructed with the same mapping parameters and the datasets are loaded in the *Image Display and Processing* window, the final step is to rescale the *Window Image Intensity* as described above.

To access the dynamic range of the reconstructed image intensity defined by *RECO: output word size*, rather than the displayed dynamic range, the pixel intensities must be exported to an ASCII file. This is achieved through the *convert\_2dseq2csv* macro available in the ParaVision *Macro Manager* under the category *Bruker*. I find *SigmaPlot* very effective for creating 3D plots from these datasets.